REMOTE SENSING OF THE PLASMASPHERE BY GROUND-BASED OBSERVATIONS OF GEOMAGNETIC FIELD LINE RESONANCES

(M. Vellante)

Department of Physical and Chemical Sciences, University of L'Aquila, ITALY

Course on:

"Radiation Belt Dynamics and Remote Sensing of the Earth's Plasmasphere"

26-30 September, 2022, L'Aquila, Italy

REMOTE SENSING OF THE PLASMASPHERE BY GROUND-BASED OBSERVATIONS OF GEOMAGNETIC FIELD LINE RESONANCES

OUTLINE

- MHD wave modes in a uniform, cold plasma;
- MHD wave modes in a dipole field;
- Uncoupled toroidal and poloidal modes, eigenfrequency calculation (dipole and general magnetic field geometry);
- Plasma mass density inference;
- Field line resonance (FLR): basic theoretical characteristics (Southwood’s box model);
- Effects of the ionosphere on ground observations;
- Methods for detecting FLRs at ground: polarization methods, gradient/cross-phase technique;
- Experimental observations of FLRs on the ground and plasmasphere monitoring.

ULF waves (Geomagnetic pulsations)

- ULF (1 mHz – 1 Hz) oscillations of the geomagnetic field observed both in space and on the ground.

- In 1954, Dungey suggested that the common occurrence of regular geomagnetic pulsations with distinct periods could be the signature of standing Alfvèn waves on geomagnetic field lines (field line resonances: FLRs).

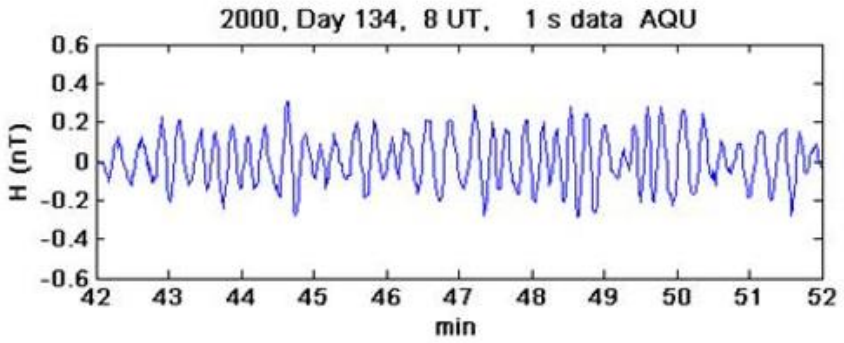

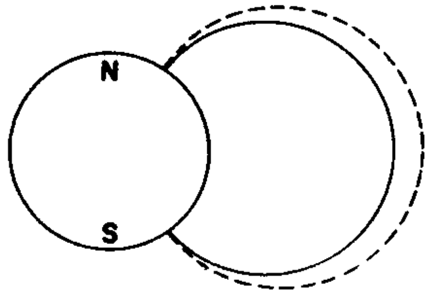

- Using the analogy with a vibrating string, it was then realized that these oscillations detected on the ground could be used to remote sense the magnetospheric plasma density (*Gul'elmi*, 1966).

- Magnetospheric waves in the ULF frequency range can be described using the MHD approximation: frequency lower than the ion girofrequency.

Basic MHD equations for small amplitude perturbations (**b**, **e**, **v**, **j**)

in a cold, highly conducting, collisionless, magnetized fluid:

1) $\nabla \times \mathbf{e} = -\,\partial \mathbf{b}/\partial t$ Faraday's law

2) $\nabla \times \mathbf{b} = \mu_o \mathbf{j}$ Ampère's law

3) $\mathbf{e} = -\,\mathbf{v} \times \mathbf{B}$ Ohm's law (frozen field)

4) $\rho\, \partial \mathbf{v}/\partial t = \mathbf{j} \times \mathbf{B}$ Momentum equation

$\rightarrow$

$$\partial^2 \mathbf{e}/\partial t^2 = \mathbf{V_A} \times \mathbf{V_A} \times \nabla \times \nabla \times \mathbf{e}$$

$\mathbf{V_A} = \mathbf{B}/(\mu_o \rho)^{1/2}$ = Alfvén velocity

---

In the ionosphere, where collisions are important:

3') $\mathbf{j} = \sigma_o \mathbf{e}_{//} + \sigma_P \mathbf{e}_{\perp} + \sigma_H \mathbf{e}_{\perp} \times (\mathbf{B}/B)$

σ_o: parallel conductivity

σ_P: Pedersen conductivity

σ_H: Hall conductivity

MHD WAVE MODES IN A UNIFORM, COLD PLASMA

1) ALFVEN (TRANSVERSE) MODE

Non-compressional, guided along the ambient field **B**

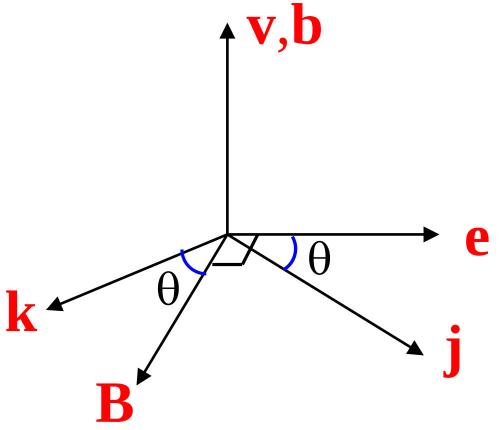

b ⊥ B

Poynting vector **S // B**

$\omega = k_{//} V_A$ $\qquad$ $V_A = B/(\mu_o \rho)^{1/2}$

STANDING WAVE (generated by multiple reflections of the Alfvén wave)

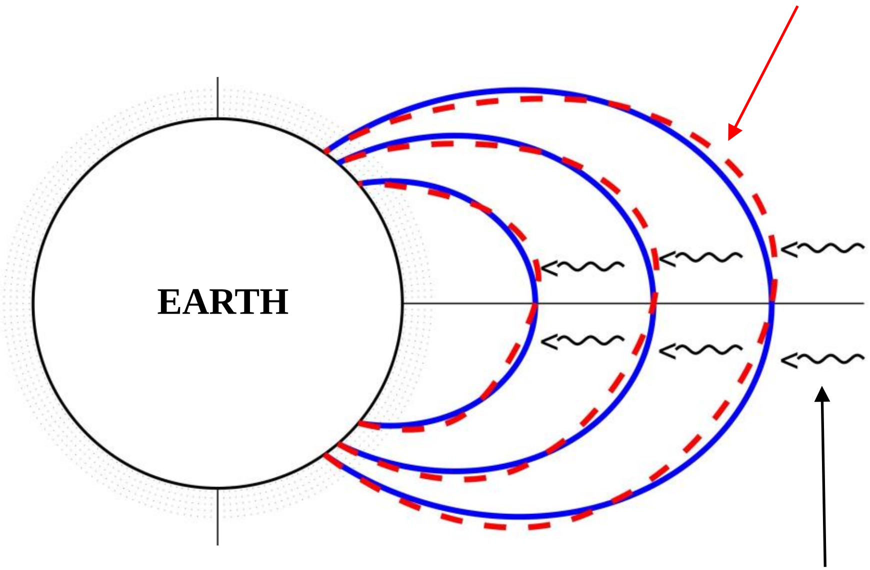

COMPRESSIVE WAVES

2) FAST (COMPRESSIONAL) MODE

No preferencial guidance: isotropic mode

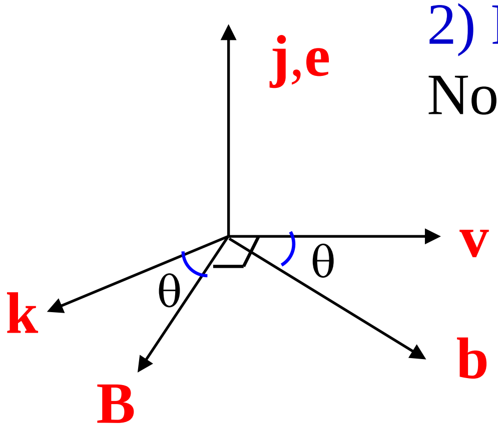

$\mathbf{b}_{//} \neq 0$

$\mathbf{S}_{\perp} \neq 0$

$\omega = k V_A$

A typical Alfvén velocity in the magnetosphere is $\sim 10^3$ km/s, while typical periods of ULF waves (geomagnetic pulsations) are in the range 10 – 500 s.

Thus, typical wavelengths are in the range 1 -100 R_E: comparable or even greater than the size of the magnetosphere.

Therefore, the uniform cold plasma approximation is not appropriate.

MHD WAVE MODES IN A DIPOLE FIELD

(*Cummings et al.*, 1969)

$\frac{\partial}{\partial \mu}$ = derivative along the field line

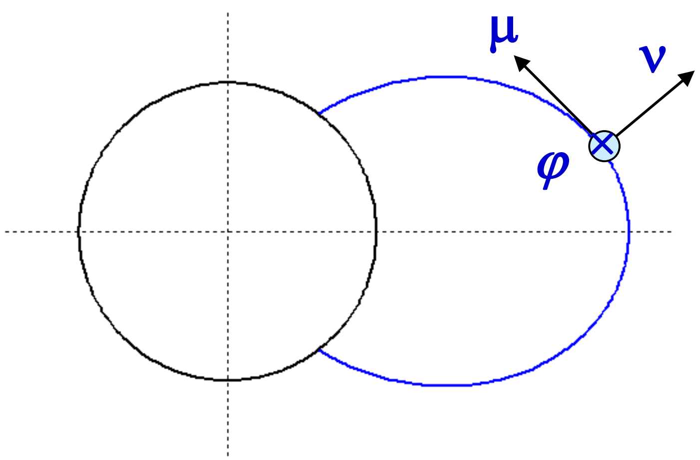

1) $$\left(g_\varphi \frac{\partial}{\partial \mu} g_\nu \frac{\partial}{\partial \mu} - \frac{1}{V_A^2}\frac{\partial^2}{\partial t^2}\right) h_\nu e_\nu = \left(g_\varphi \frac{\partial}{\partial \phi}\frac{\partial}{\partial t}\right) h_\mu b_\mu$$

2) $$\left(g_\nu \frac{\partial}{\partial \mu} g_\varphi \frac{\partial}{\partial \mu} - \frac{1}{V_A^2}\frac{\partial^2}{\partial t^2}\right) h_\varphi e_\varphi = -\left(g_\nu \frac{\partial}{\partial \nu}\frac{\partial}{\partial t}\right) h_\mu b_\mu$$

3) $$\frac{\partial}{\partial t}(h_\mu b_\mu) = \frac{\partial}{\partial \nu}(h_\varphi e_\varphi) - \frac{\partial}{\partial \varphi}(h_\nu e_\nu)$$

$g_\varphi, g_\nu, h_\varphi, h_\nu, h_\mu$: dipole metric functions

Transverse and compressional modes are coupled

Axial symmetry: $\partial/\partial\varphi = 0$

TOROIDAL MODE

$$\left(g_\varphi \frac{\partial}{\partial\mu} g_\nu \frac{\partial}{\partial\mu} - \frac{1}{V_A^2}\frac{\partial^2}{\partial t^2}\right) h_\nu \mathbf{e}_\nu = 0$$

Polarization: $\mathbf{e}_\nu , \mathbf{b}_\varphi , \mathbf{v}_\varphi$

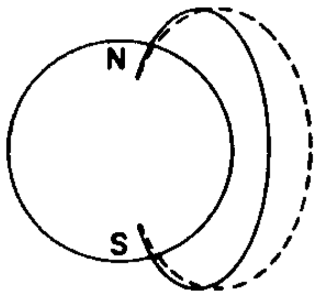

Azimuthal oscillations of plasma and field lines.

Independent, in-phase torsional oscillation of individual magnetic shells.

Poynting vector $\mathbf{S} \propto \mathbf{e} \times \mathbf{b}$ along $\mathbf{B}$

↓

Wave **guided** along the field line.

POLOIDAL MODE

$$\left(g_\nu \frac{\partial}{\partial\mu} g_\varphi \frac{\partial}{\partial\mu} + g_\nu \frac{\partial^2}{\partial\nu^2} - \frac{1}{V_A^2}\frac{\partial^2}{\partial t^2}\right) h_\varphi \mathbf{e}_\varphi = 0$$

Polarization: $\mathbf{e}_\varphi , \mathbf{b}_\nu , \mathbf{b}_\mu , \mathbf{v}_\nu$

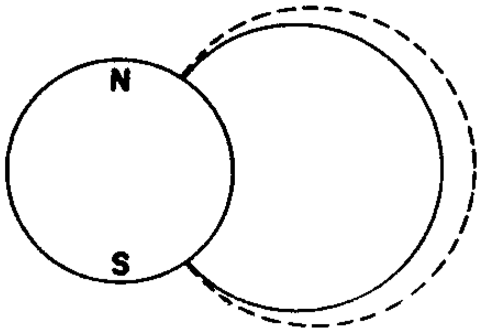

Plasma and field line oscillations in the meridian plane.

Propagation across the magnetic field.

$\mathbf{b}_\mu = \mathbf{b}_{//} \neq 0$ ⟶ **compressional** mode

Localised mode: $\partial/\partial\varphi \to \infty$

Oscillations at different meridian planes are decoupled

GUIDED POLOIDAL MODE

$$\left(g_\nu \frac{\partial}{\partial\mu} g_\varphi \frac{\partial}{\partial\mu} - \frac{1}{V_A^2}\frac{\partial^2}{\partial t^2} \right) h_\varphi \, \mathbf{e}_\varphi = 0$$

Polarization: e_φ , b_ν , v_ν

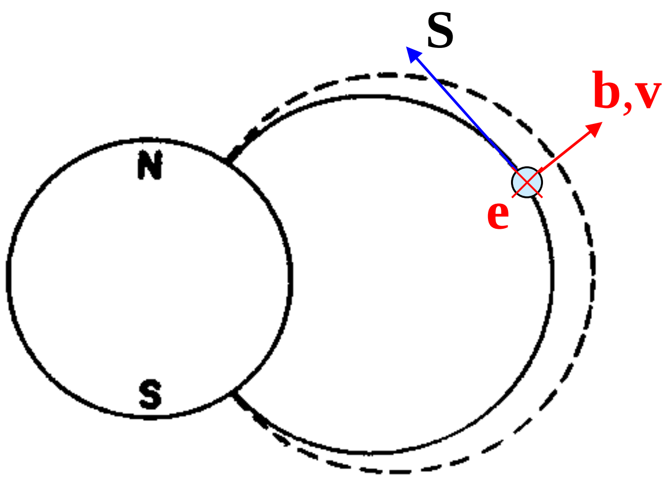

SCHEMATIC PLOT OF THE GUIDED STANDING OSCILLATIONS IN THE MAGNETOSPHERE

Magnetic field lines have fixed ends in the ionosphere, assumed as a perfect conductor.
Multiple reflections of the guided Alfvén wave generate a standing structure.

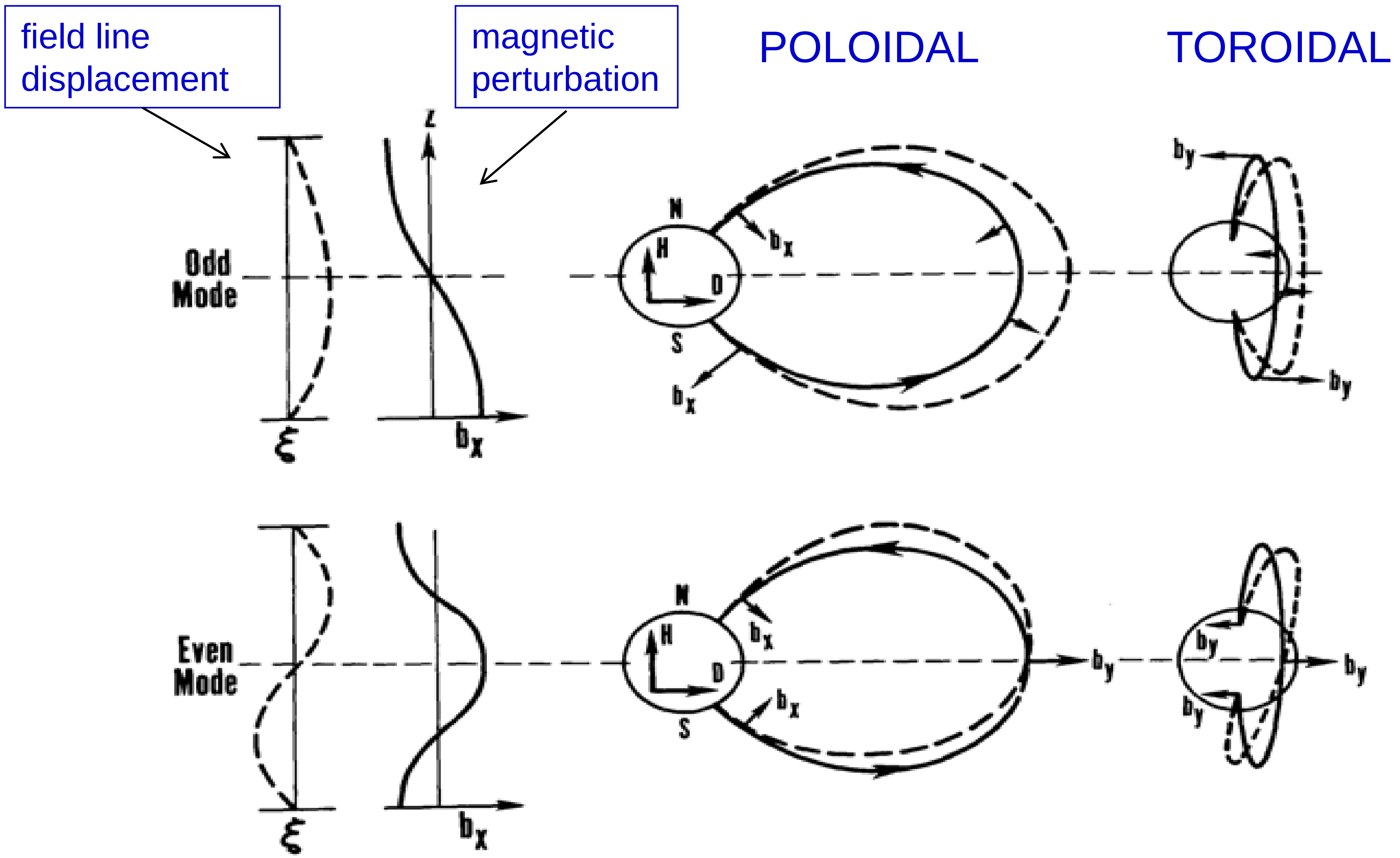

McPherron (2005)

WKB / TIME-OF-FLIGHT APPROXIMATION

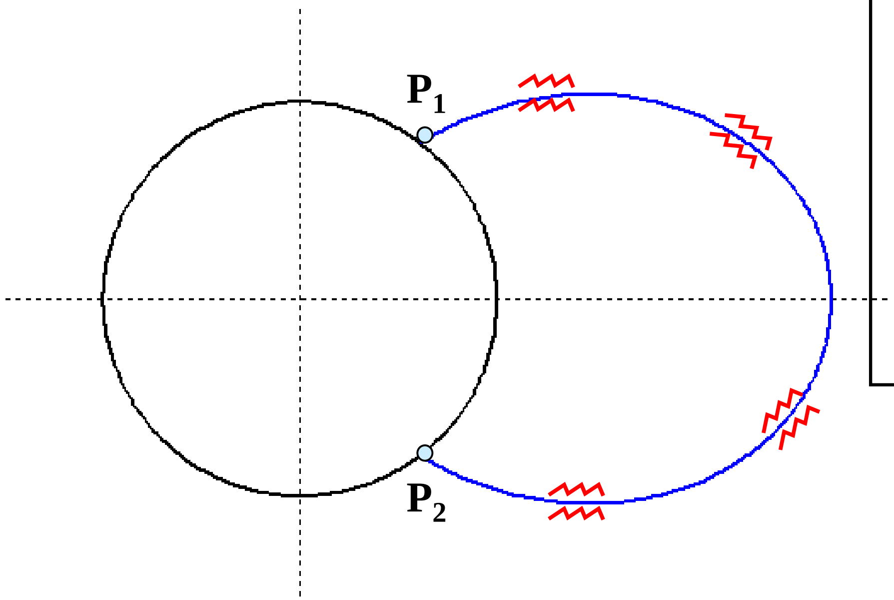

field-line eigenperiods ≡ time-of-flight :

$$T_n = \frac{2}{n}\int_{P_1}^{P_2} \frac{ds}{V_A(s)} \qquad n = 1, 2, 3, \ldots$$

$V_A(s) = B(s) / [\mu_o \rho(s)]^{1/2}$ = field-aligned Alfvén velocity

$$T_n = \frac{2}{n}\mu_o^{1/2} \int_{P_1}^{P_2} \frac{\rho^{1/2}(s)}{B\ (s)} ds$$

GUIDED EIGENMODES CALCULATION

Temporal variations: $exp(-i\omega t)$ $\quad z = \cos\theta$

AXISYMMETRIC TOROIDAL MODE

$$\frac{d^2\boldsymbol{\varepsilon}_\nu}{dz^2} + r_{eq}^2(1+3z^2)\frac{\omega^2}{V_A^2(z)}\boldsymbol{\varepsilon}_\nu = 0$$

$$\varepsilon_\nu = h_\nu e_\nu$$

LOCALISED POLOIDAL MODE

$$\frac{d^2\boldsymbol{\varepsilon}_\varphi}{dz^2} - \frac{6z}{1+3z^2}\frac{d\boldsymbol{\varepsilon}_\varphi}{dz} + r_{eq}^2(1+3z^2)\frac{\omega^2}{V_A^2(z)}\boldsymbol{\varepsilon}_\varphi = 0$$

$$\varepsilon_\varphi = h_\varphi e_\varphi$$

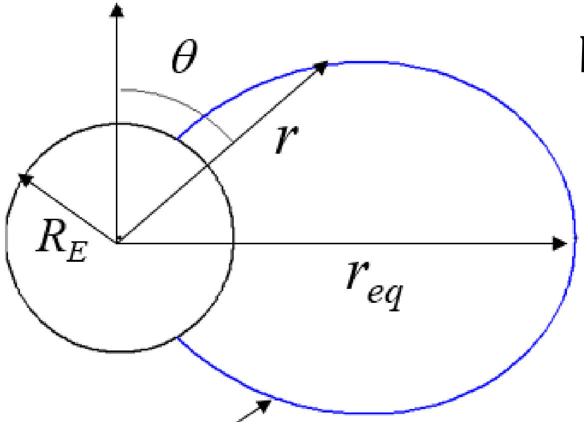

$r = r_{eq} \sin^2\theta$

$V_A = B / (\mu_o \rho)^{1/2}$ Alfvén velocity

Both space and ground observations show that the **toroidal** mode is the one most commonly excited.

TOROIDAL OSCILLATION

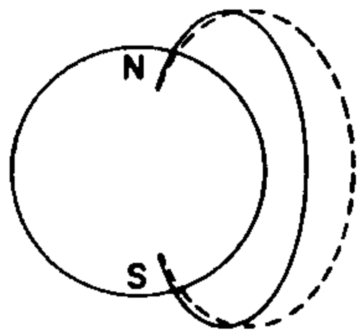

The reason is that field lines azimuthally adjacent to the vibrating line have nearly the same resonant frequency and so can vibrate in phase with the initially disturbed line.

POLOIDAL OSCILLATION

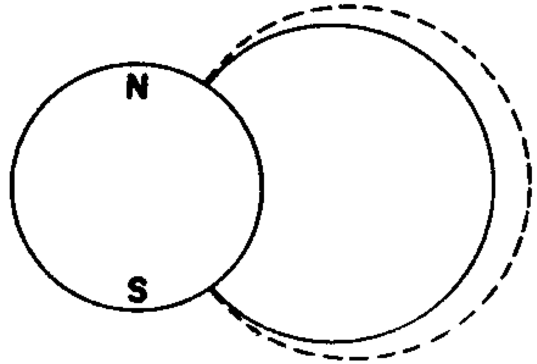

Conversely, in the poloidal mode field lines oscillate in the meridian plane and adjacent lines have different frequencies. Inevitably, adjacent field lines will oscillate out of phase and this mode will rapidly decay.

EIGENFREQUENCIES CALCULATION FOR THE AXISYMMETRIC TOROIDAL MODE

$$\frac{d^2\boldsymbol{\varepsilon_\nu}}{dz^2} + r_{eq}^2(1+3z^2)\frac{\omega^2}{V_A^2(z)}\boldsymbol{\varepsilon_\nu} = 0 \longrightarrow \boxed{\frac{d^2\varepsilon_\nu}{dz^2} + \lambda(1-z^2)^6\,\frac{\rho(z)}{\rho_{eq}}\,\varepsilon_\nu = 0 \qquad \lambda = \frac{\mu_o\,\rho_{eq}\,\omega^2\,r_{eq}^8}{B_E^2\,R_E^6}}$$

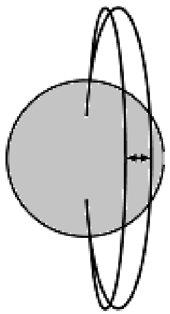

Toroidal Mode

$\varepsilon_\nu = h_\nu e_\nu$: wave electric field

$z = cos(\theta)$, θ : colatitude

ρ : mass density along the field line

ρ_{eq}: equatorial mass density

Eigenvalues $\boldsymbol{\lambda}$ can be numerically found imposing:

1) the boundary condition: $\boldsymbol{\varepsilon_\nu = 0}$ at the altitude (100-200 km) where the wave is reflected.
2) A given functional form for the mass density along the field line.

Common assumption: $\boldsymbol{\rho(r)/\rho_{eq} = (r/r_{eq})^{-m}}$

For any given ***L*- shell** and ***m*** value, the **equatorial** mass density inferred from the observed resonance frequency $\boldsymbol{f_R}$ is:

$$\boxed{\tilde{\rho}_{eq} = \frac{B_E^2}{4\pi^2\mu_o R_E^2}\,\frac{\lambda(L,m)}{L^8 f_r^2}}$$

For a given L $\Rightarrow$ $\tilde{\rho}_{eq} = \dfrac{\text{const}\,(L,m)}{f_R^2}$

Dependence on the assumed density distribution along the field line

At high and middle latitudes, the Alfvén velocity is minimum in the equatorial region of the line of force, and so most of the wave travel time is spent in that region. As a consequence, the period is essentially determined by the plasma mass density in the equatorial region. For this reason, the inferred equatorial density is not very sensitive to the assumed density distribution, i.e. on the assumed power law index *m*.

However, at lower latitudes ($L < 2$), the previous assumption is no longer true and no specific power law dependence can be considered a reasonable approximation of the real profile for the outer part of the field line and the density inference is more sensitive to the assumed density distribution.

Alfvén velocity distribution along the geomagnetic field line for $\boldsymbol{L = 4}$ and $\boldsymbol{L = 1.33}$. ***Poulter et al*. (1988)**

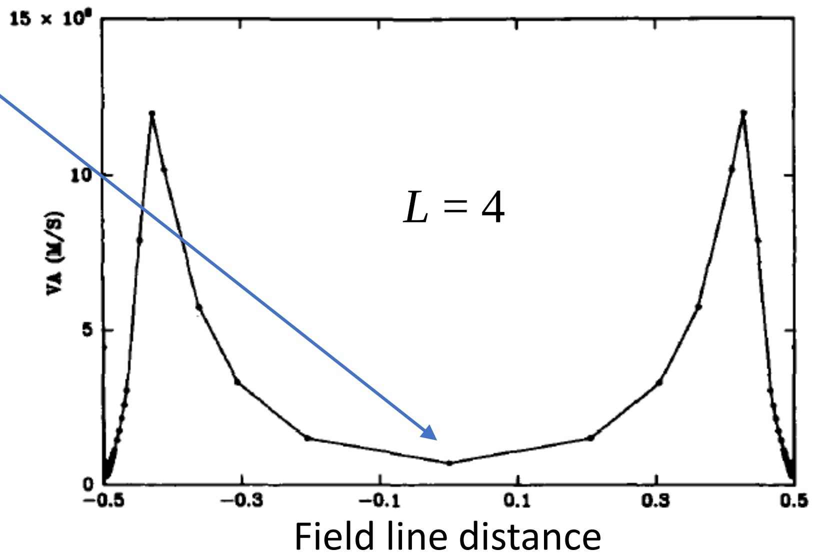

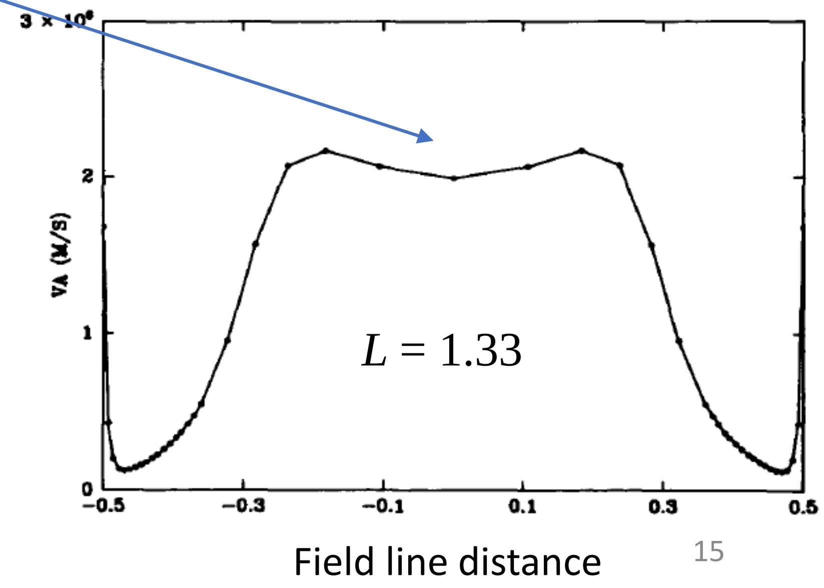

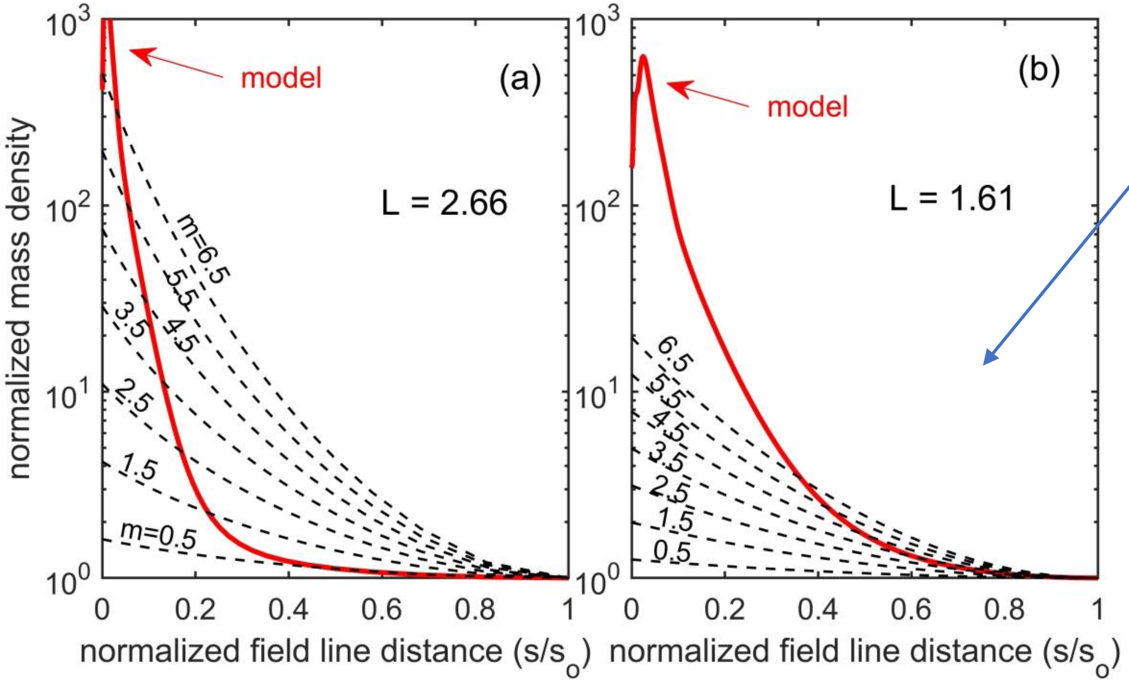

Vellante & Förster (2006)

Effects of external sources

At high latitudes, and even at low and middle latitudes during disturbed conditions (*Berube et al.*, 2006), need to consider geomagnetic field geometry more realistic than dipole or IGRF geometry (i.e. *Tsyganenko* models).

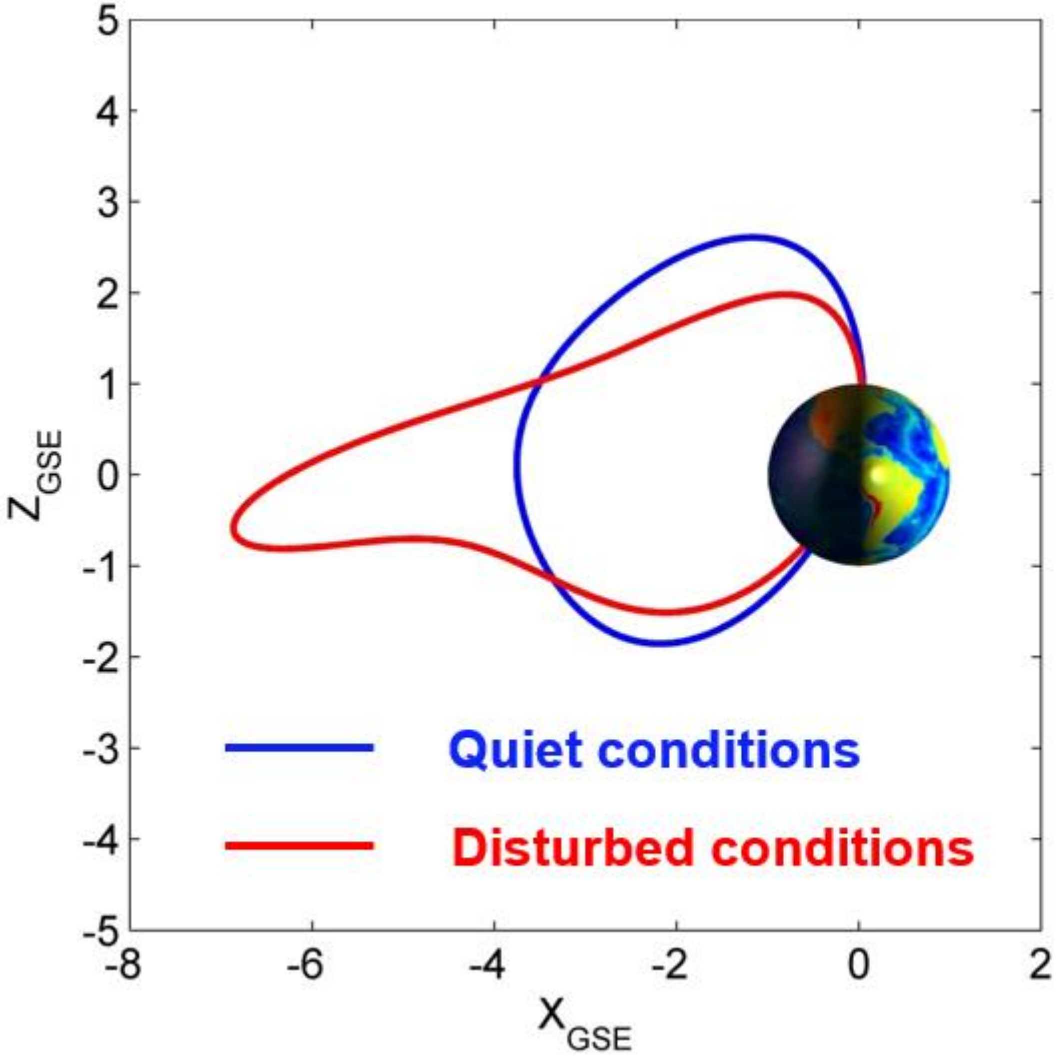

Arbitrary field geometry (*Singer et al.*, 1981)

$$\frac{d^2\xi'}{ds^2} + \frac{d\left[\ln\left(h_\alpha^2 B\right)\right]}{ds}\frac{d\xi'}{ds} + \frac{\omega^2}{V_A^2}\xi' = 0$$

s distance along the field line

B (s) magnetic field

$\xi'(s) = \xi(s) / h_\alpha(s)$

$\xi(s)$ field line displacement

$h_\alpha(s)$ distance to an adjacent field line

An example of a pulsation event with latitude-dependent period (*Cz. Miletits et al.*, 1988)

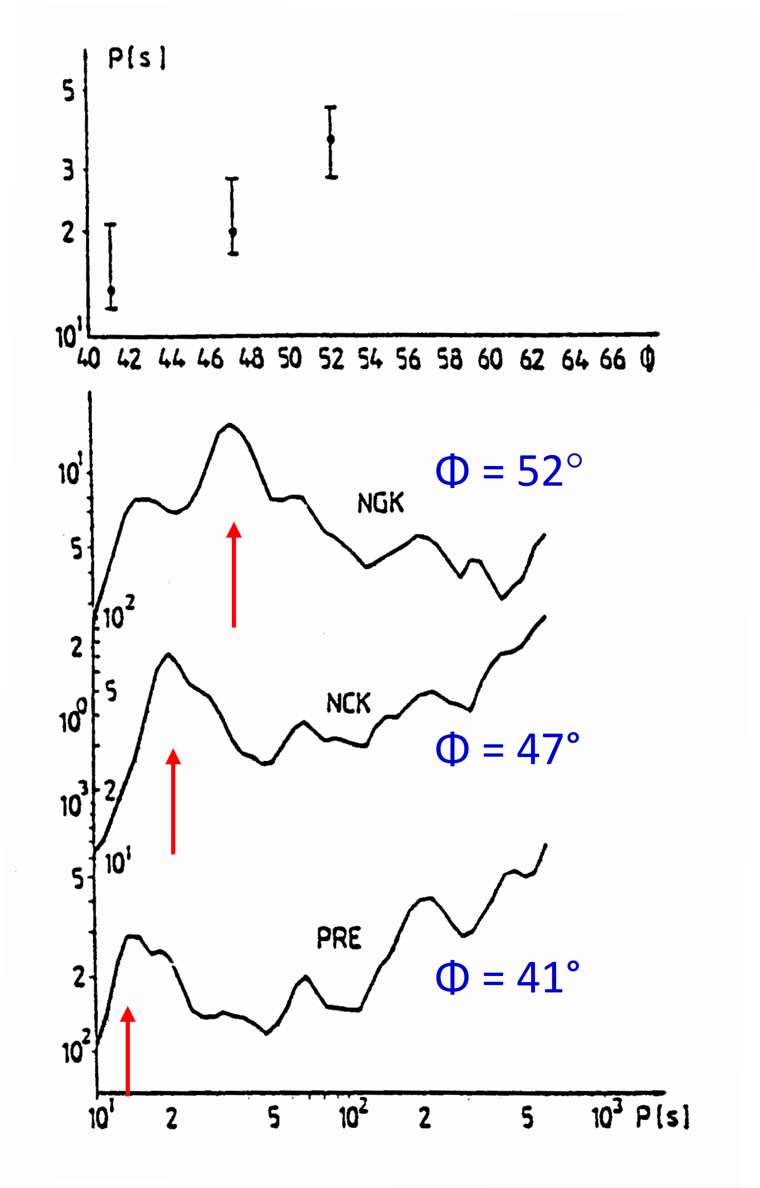

Amplitude and phase patterns vs latitude

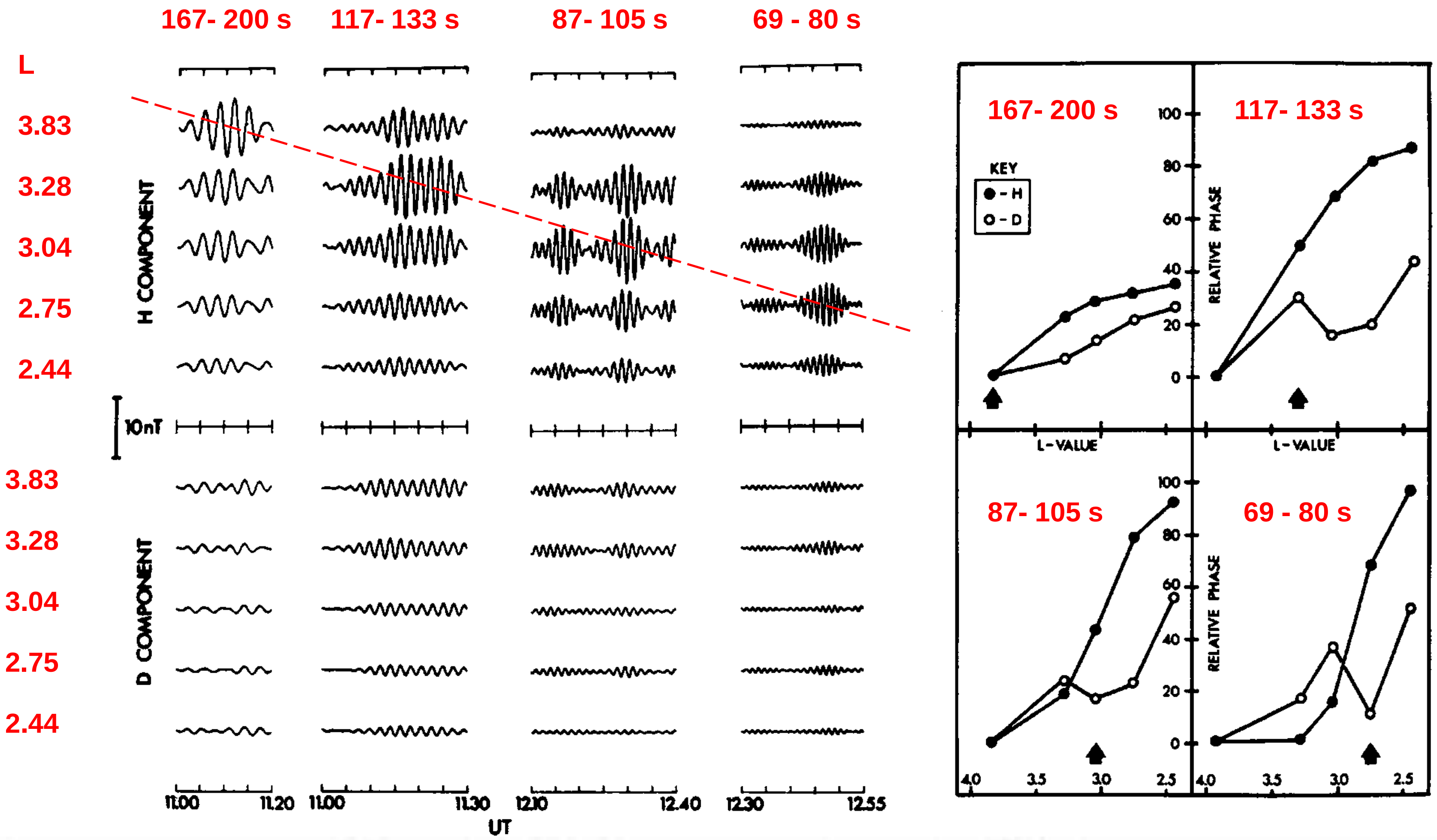

Fig. 4. a) *H*- and *D*-wave packets filtered in different period bands at a meridional array in Great Britain ($L = 3.83, 3.28, 3.04, 2.75, 2.44$ from top to the bottom). b) Corresponding wave phases relative to the most northern station. Arrows indicate the latitude where the *H*-component peaks (Green, 1978).

Diurnal and latitudinal polarization pattern

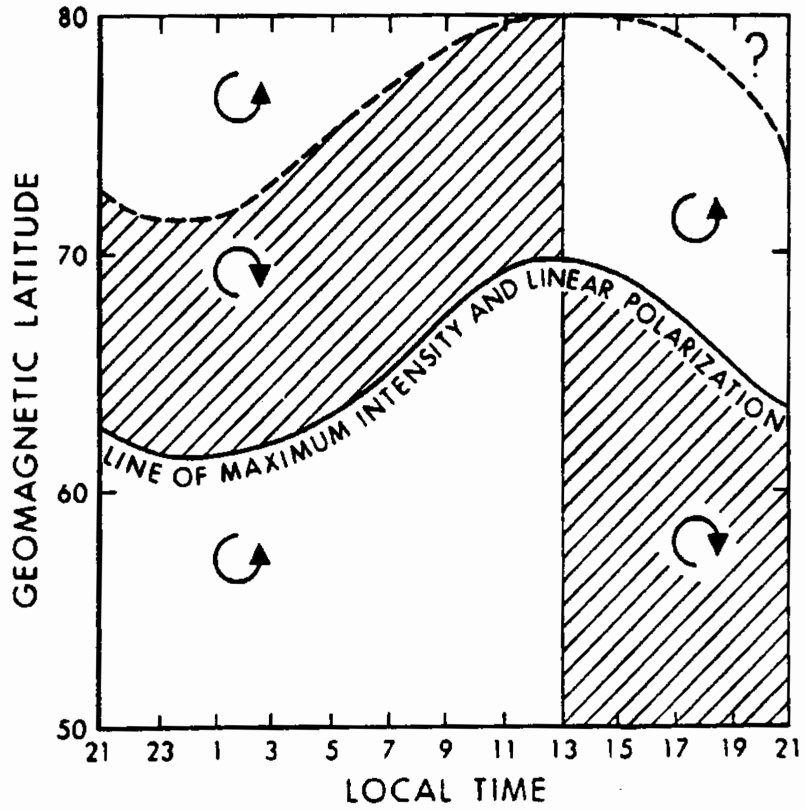

Fig. 5. The diurnal and latitudinal variation of the polarization for micropulsations with frequencies of ∼ 5 mHz. For higher frequencies the pattern shifts equatorward. These results were obtained from measurements taken at a latitudinal array of stations in Canada (Samson et al., 1971).

Polarization reversals across:

- noon meridian
- latitude of maximum amplitude

Kelvin-Helmholtz instability

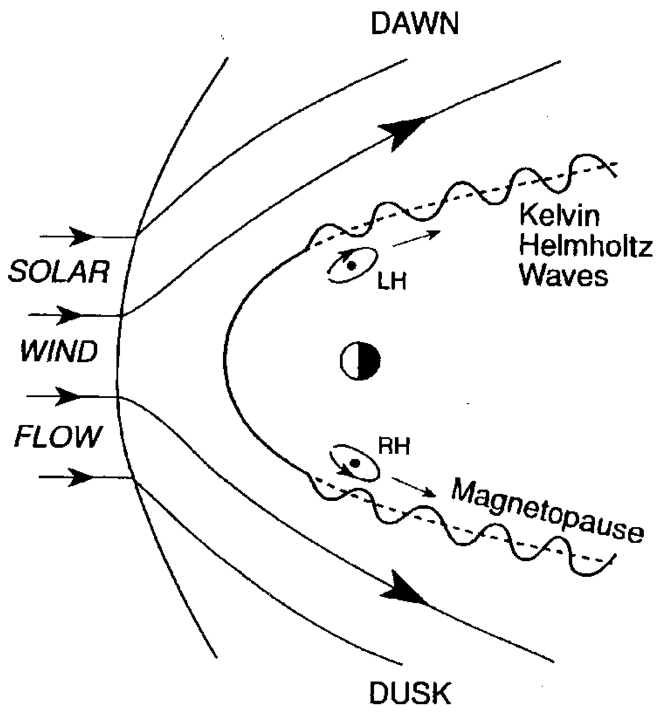

Effect of field line stretching

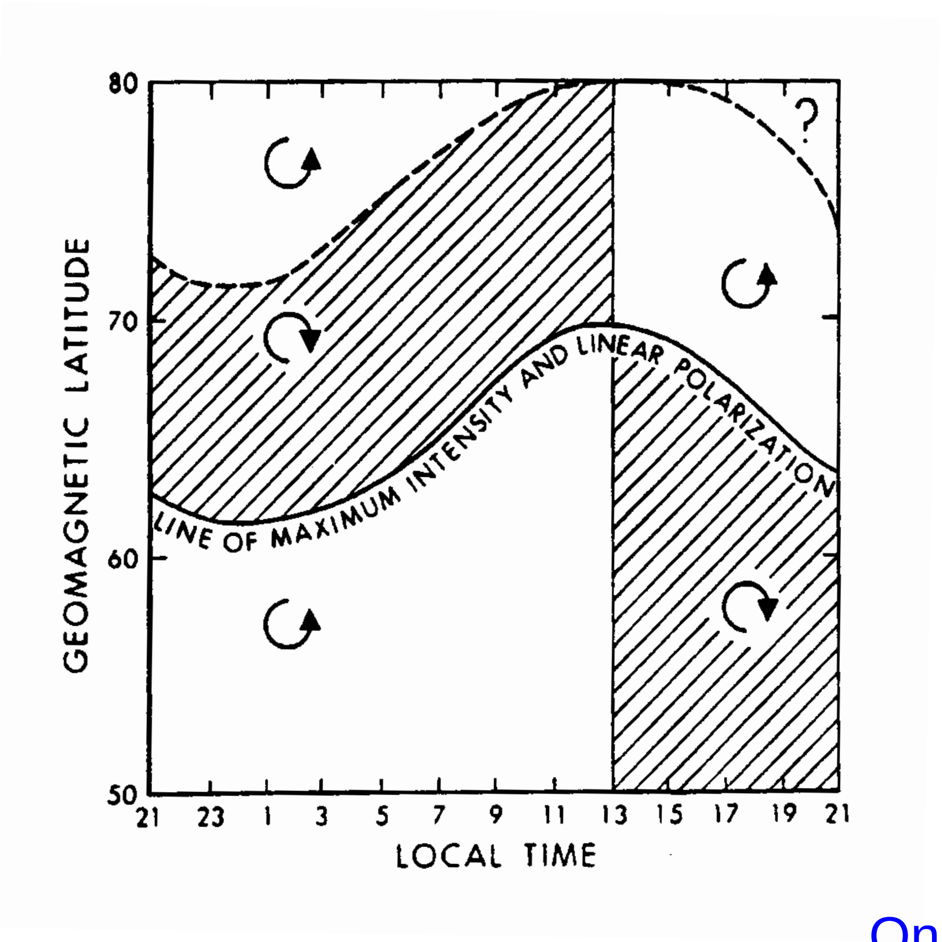

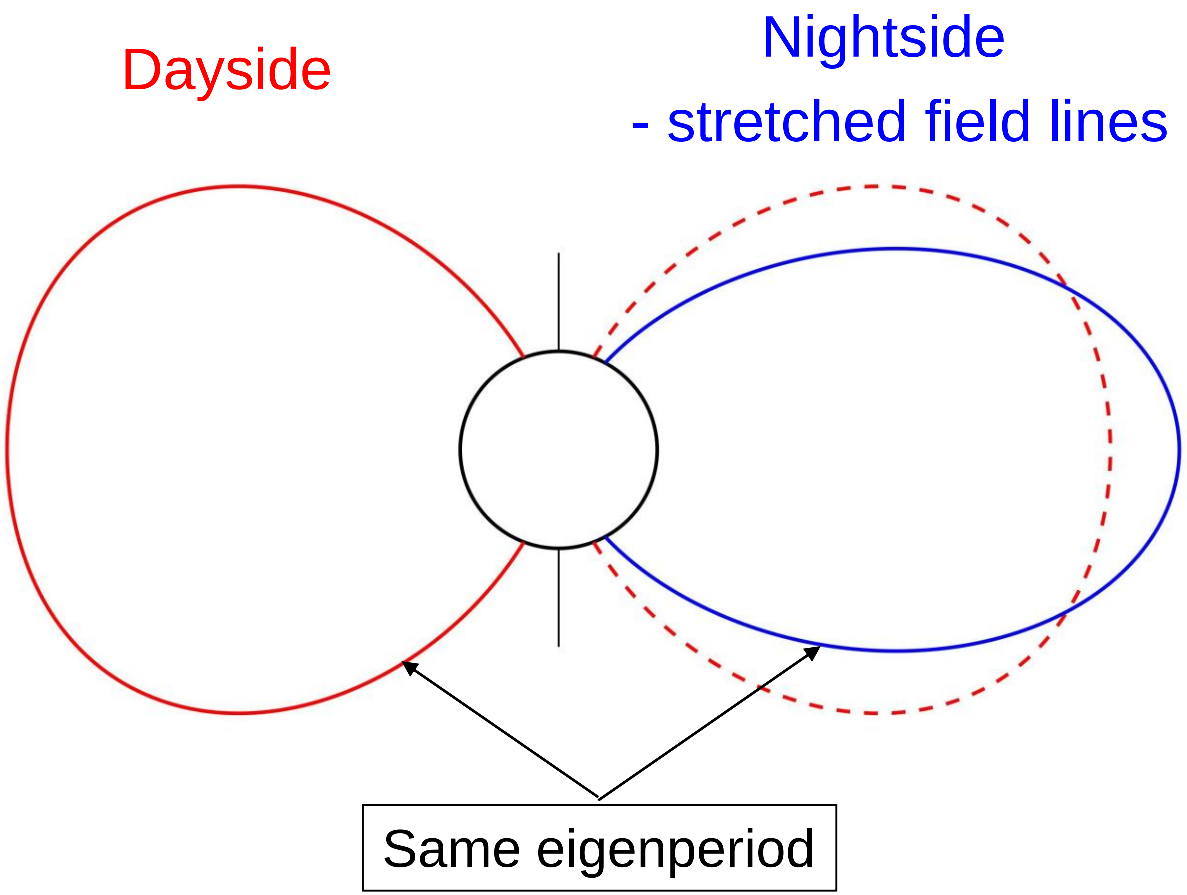

On the nightside, a given eigenperiod corresponds to a lower latitude

Field line resonance model

(*Southwood*; *Chen and Hasegawa*, 1974)

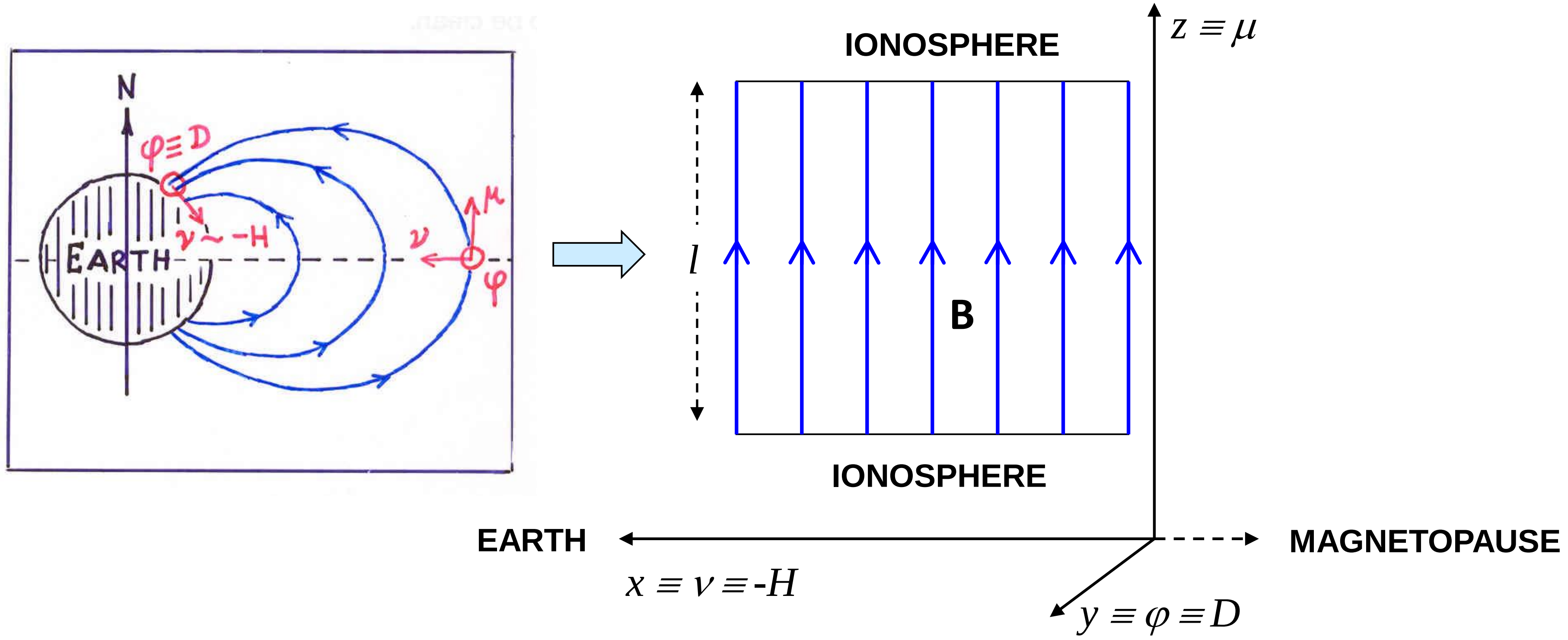

Plasma density $\rho = \rho(x)$

eigenfrequency

$\omega_R(x) = (\pi / l)\, V_A(x) =$

$= (\pi / l)\, B\, [\mu_o\, \rho(x)]^{-1/2}$

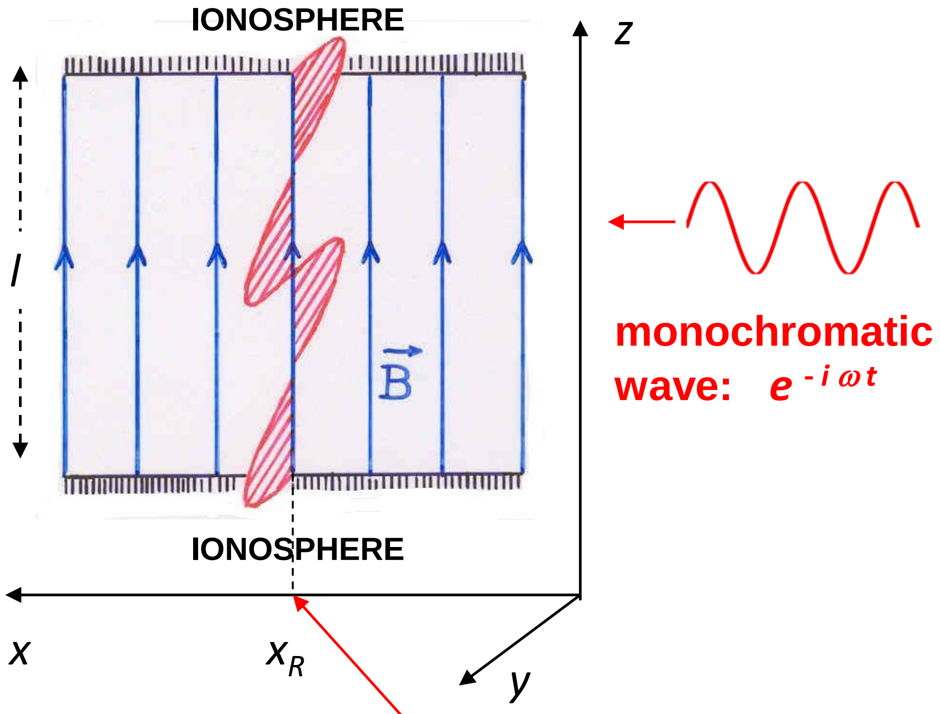

$\omega_R = \omega_R(x)$

resonance: $\omega_R = \omega$

because of dissipative effects: $\omega \rightarrow \omega - i\gamma$

assuming magnetic perturbations of the form:

$$\mathbf{b} = \mathbf{b}(x)\exp[i(k_{//}z + my - \omega t)]$$

near the resonance:

$$\frac{d^2 b_x}{dx^2} + \frac{\omega^2}{\delta[\omega^2 - \omega_R^2(x)]}\frac{db_x}{dx} - m^2 b_x = 0$$

$\delta = (\frac{1}{\rho}\frac{d\rho}{dx})^{-1}$ scale length of the inhomogeneity

singularity at $x = x_R$

By expanding $\omega_R(x)$ around $\omega_R(x_R)$:

$$\frac{d^2 b_x}{dx^2} + \frac{1}{(x - x_R - i\varepsilon)}\frac{db_x}{dx} - m^2 b_x = 0$$

$\varepsilon = 2\gamma\delta/\omega$ = resonance width

$$\frac{d^2 b_x}{dx^2} + \frac{1}{(x - x_R - i\varepsilon)} \frac{d b_x}{dx} - m^2 b_x = 0$$

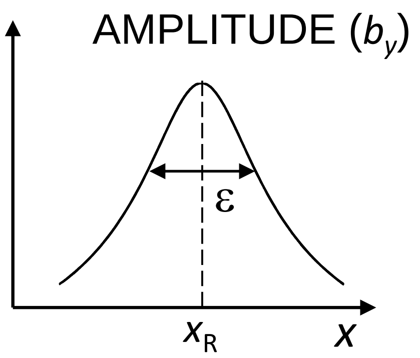

Solutions are given by the modified Bessel functions,

close to x_R :

$$b_x \sim b_o \log\left[m\,(x - x_R - i\,\varepsilon)\right]$$

$$b_y \sim \frac{i\,b_o}{m\,(x - x_R - i\varepsilon)} = \frac{b_y(x_R)}{1 + i\,(x - x_R)/\varepsilon}$$

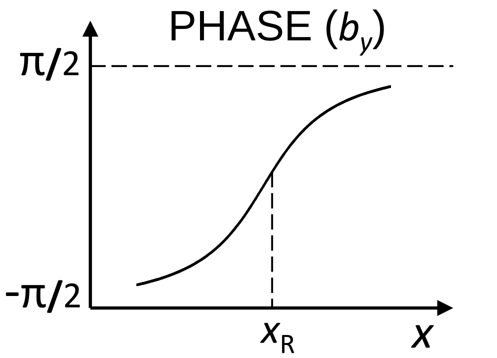

At the resonant latitude x_R :

a) More pronounced peak and sharper phase change for b_y, i.e. in the azimuthal direction: Toroidal mode dominates;

b) The horizontal polarization is predicted to reverse the sense across the resonance where becomes almost linear;

c) The horizontal polarization changes sense according to the sign of the azimuthal wave number m : if the driving source is due to the Kelvin Helmholtz instability → polarization reversal across the noon meridian.

Theory

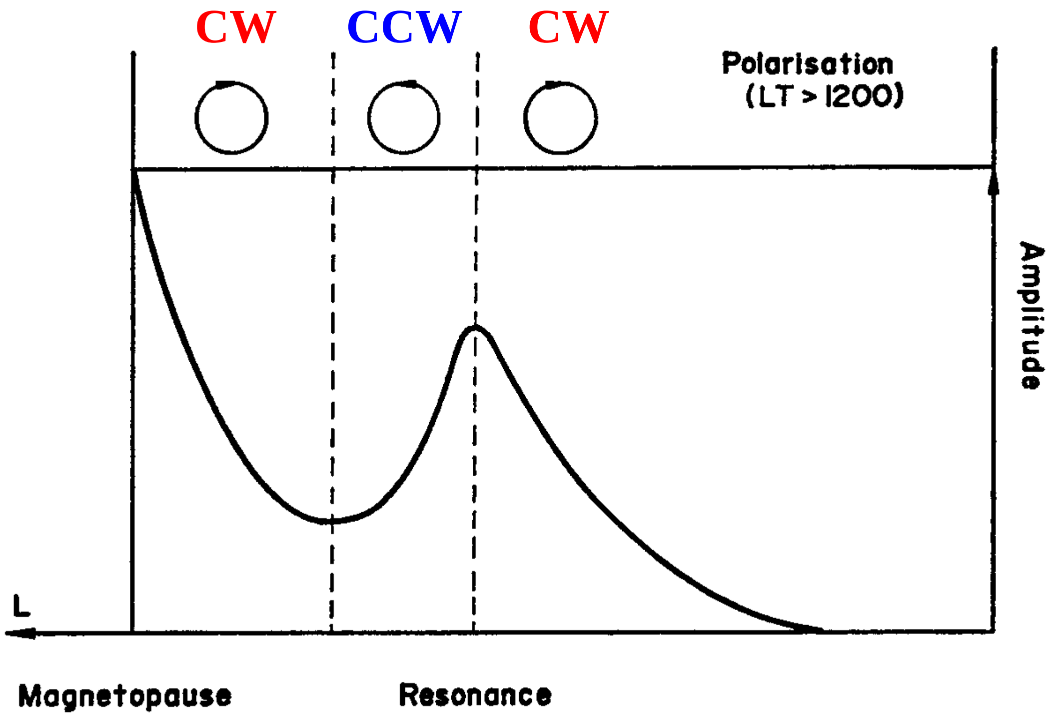

Fig. 6. Schematic representation of amplitude and polarization of an hydromagnetic wave as a function of L-shell in the magnetosphere. The source is assumed to be a monochromatic surface wave with eastward propagation ($m > 0$) as produced by the Kelvin-Helmholtz instability on the afternoon side (LT > 1200) of the magnetopause. The senses of polarization are opposite in the local morning (Southwood, 1974).

Observations

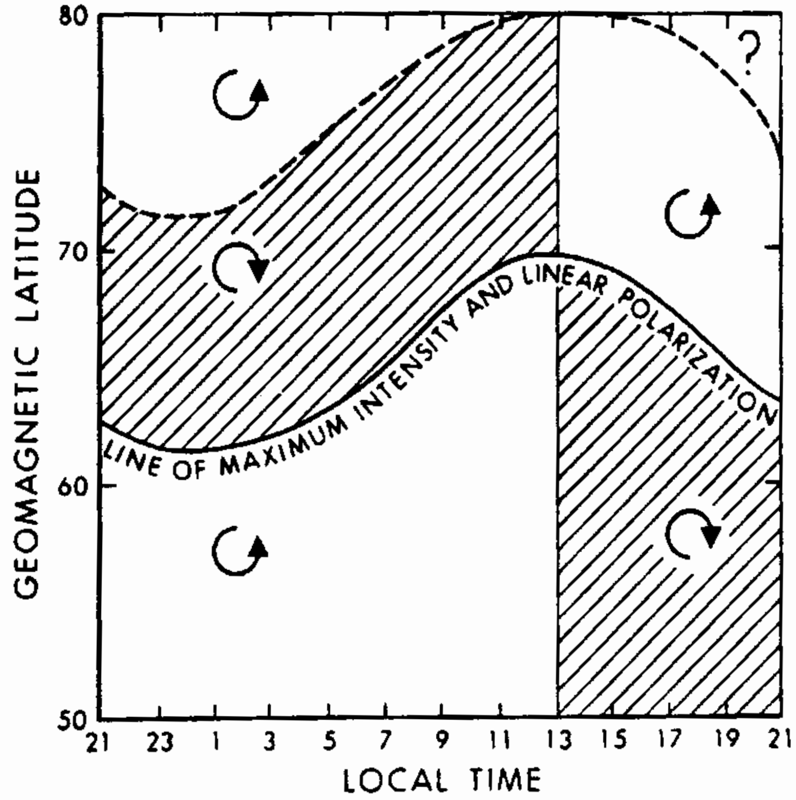

Fig. 5. The diurnal and latitudinal variation of the polarization for micropulsations with frequencies of ~ 5 mHz. For higher frequencies the pattern shifts equatorward. These results were obtained from measurements taken at a latitudinal array of stations in Canada (Samson et al., 1971).

FLR drivers

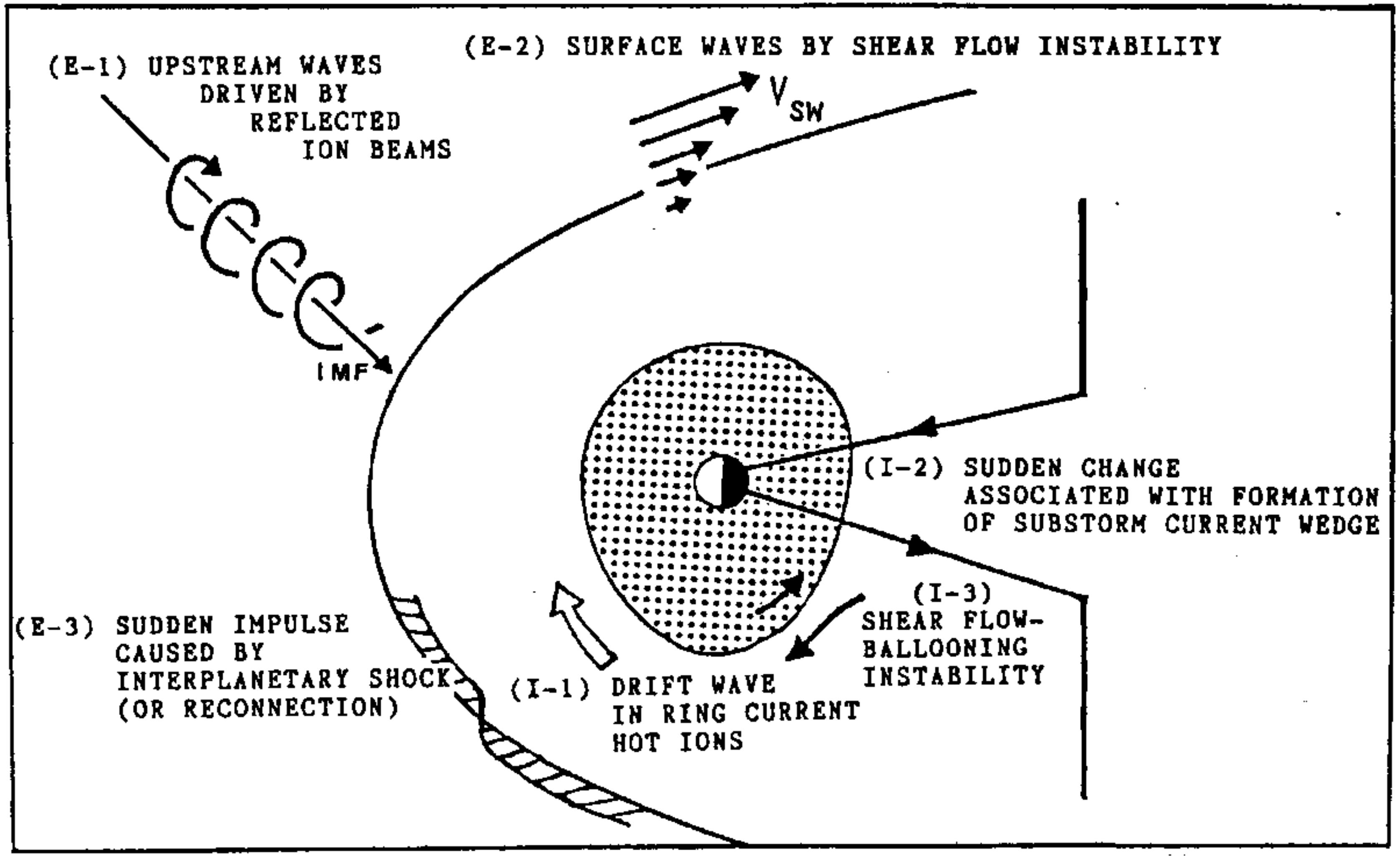

Yumoto, 1988

FLRs – cavity modes coupling

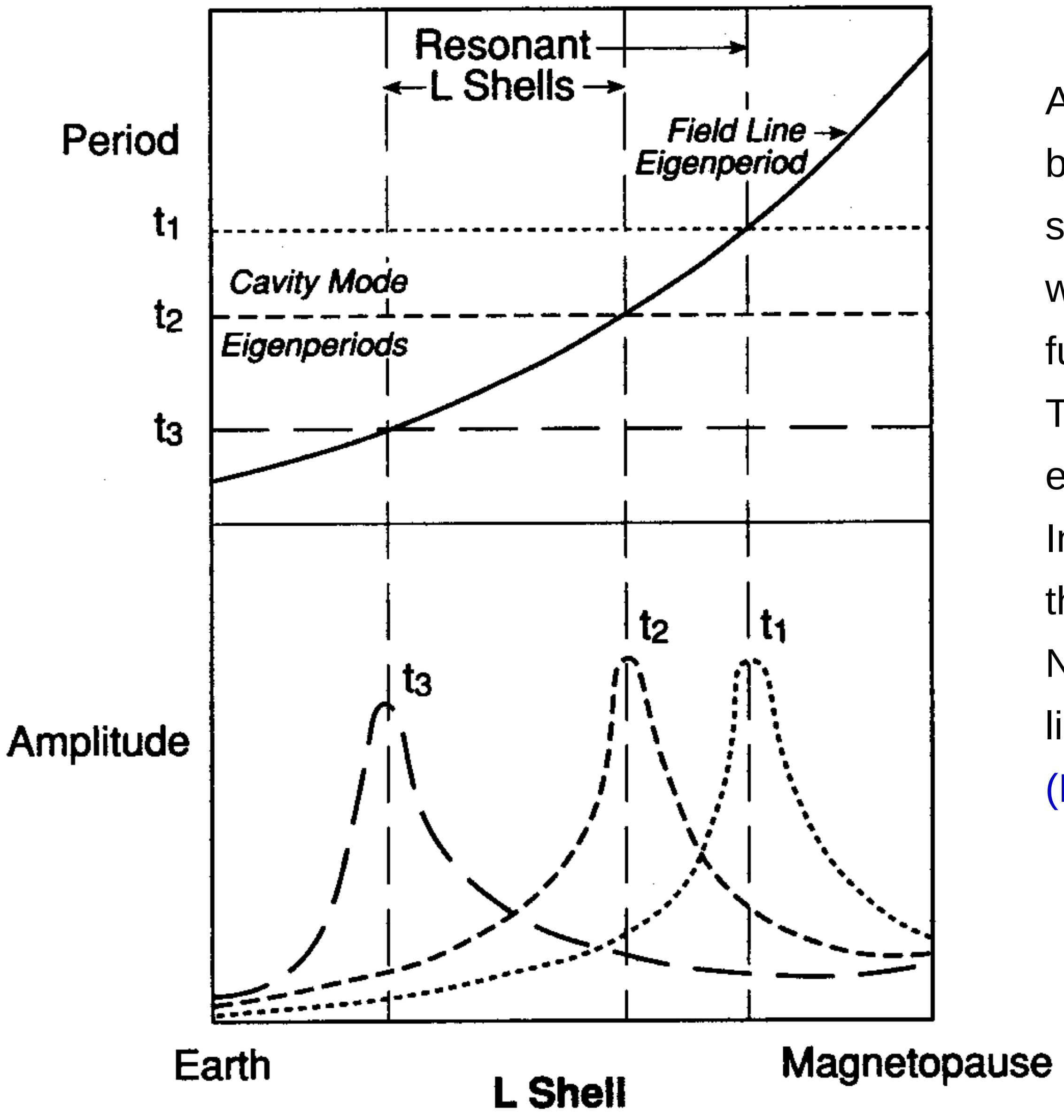

A schematic representation of field line resonances driven by resonant magnetospheric cavity modes. The top panel shows the periods of three harmonics of cavity resonance, which do not vary with L-shell, and the variation of the fundamental field line eigenperiod with L shell.

There are three L shells where the fundamental field line eigenperiod matches one of the cavity mode eigenperiods.

In the lower panel the variation of wave amplitude at each of the three cavity eigenperiods with L shell is drawn.

Note how a field line resonance is driven each time a field line eigenperiod match.

(Hughes, 1994).

IONOSPHERIC EFFECT (*Hughes*, 1983)

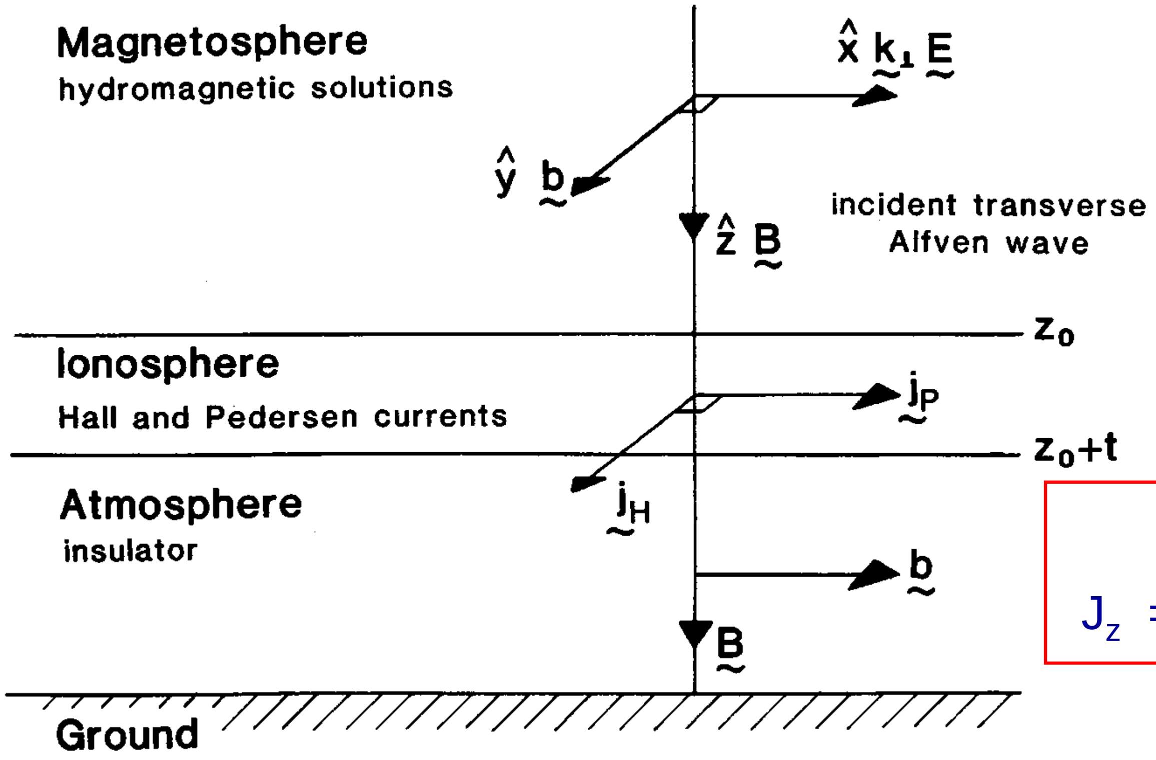

In the atmosphere (insulator)

$$J_z = \mu_o^{-1}(\nabla \mathrm{x}\mathbf{b})_z = \mu_o^{-1}\,\mathbf{k}_\perp \mathrm{x}\, \mathbf{b}_{horiz.} = 0$$

$\Downarrow$

$\mathbf{b}_{horiz.} = 0$ or $\mathbf{b}_{horiz.}$ // $\mathbf{k}_\perp$: along x

The Pedersen current shields the incident signal. On the ground, we observe the signal generated in the E-region (altitude ~120 km) by the Hall current: i.e. a 90º rotation.

Spatial integration (filtering) effect

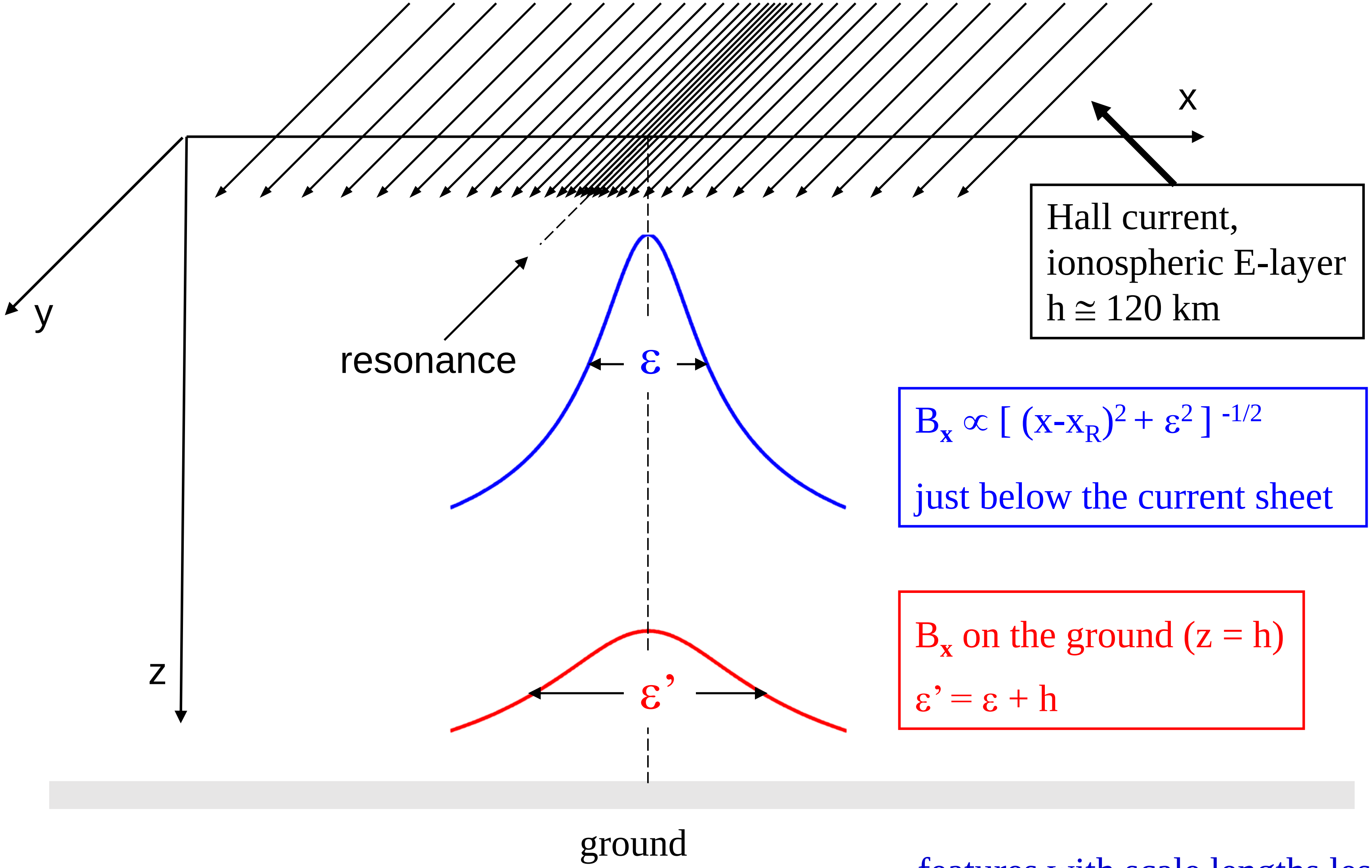

More generally: $B_{ground} \approx \left(2\,\frac{\Sigma_H}{\Sigma_P}\,e^{-k_{hor}h}\right) B_{magn}$ ➡ features with scale lengths less than ~120 km (E-region altitude) are strongly attenuated

Ionospheric effect on the resonance structure *Hughes and Southwood*, 1976

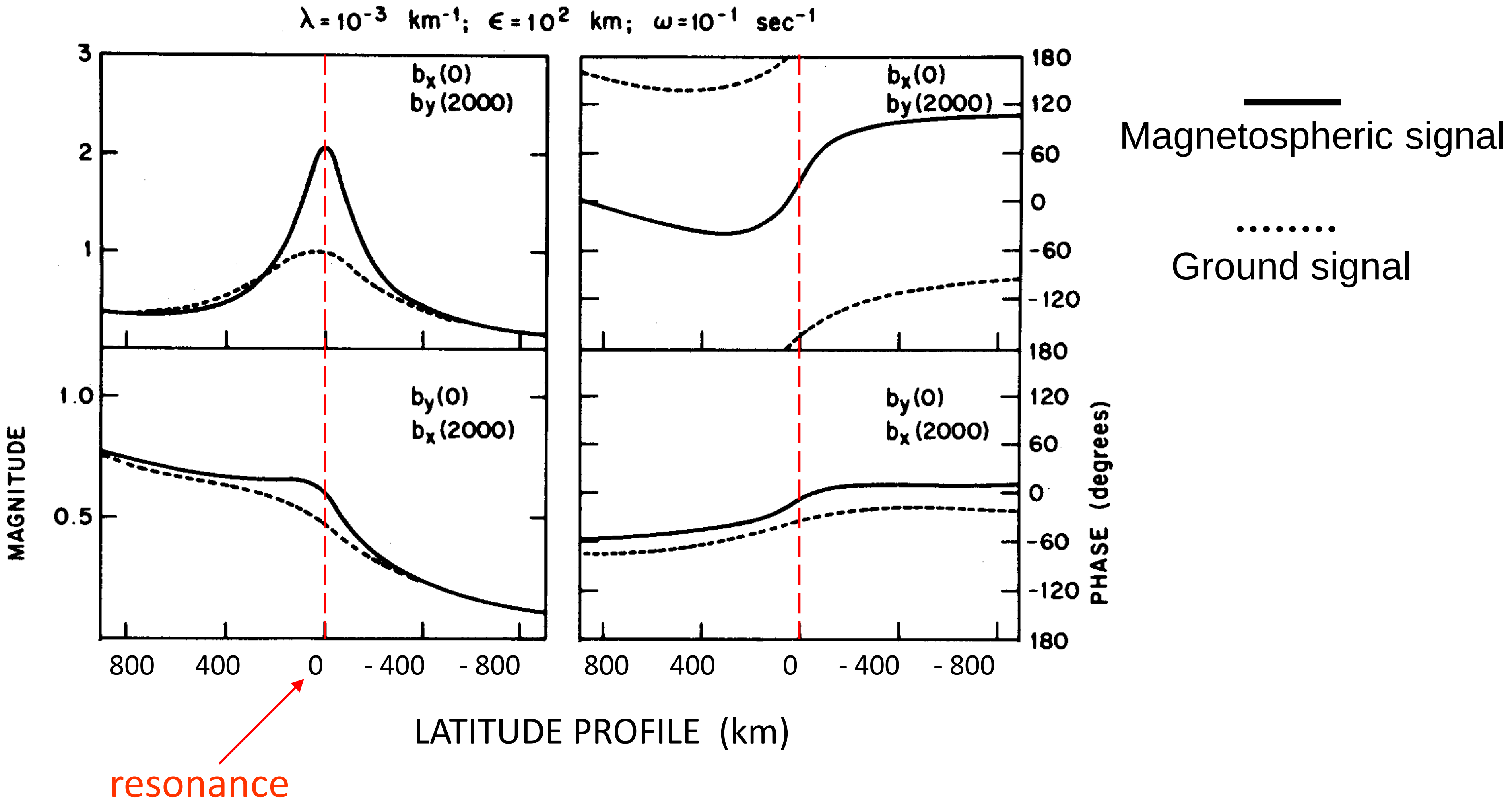

On the ground, the signal is rotated through 90° and the resonance structure is smoothed.

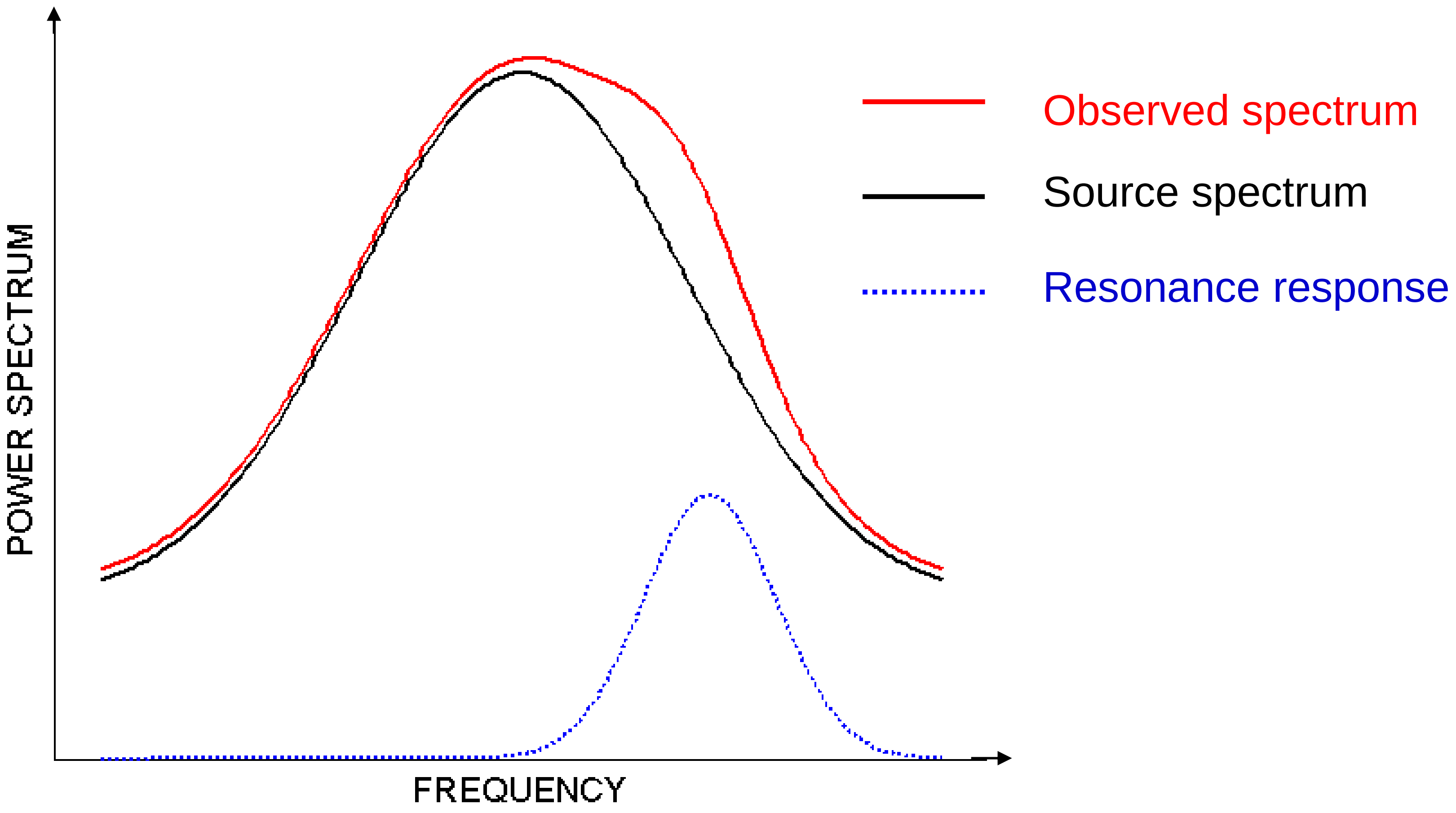

Resonance effects can be easily masked by:

- peculiarities of the source spectrum
- ionospheric smoothing

Detection of different harmonics at L = 2.3 by the H/D technique

(*Vellante et al*., 1993)

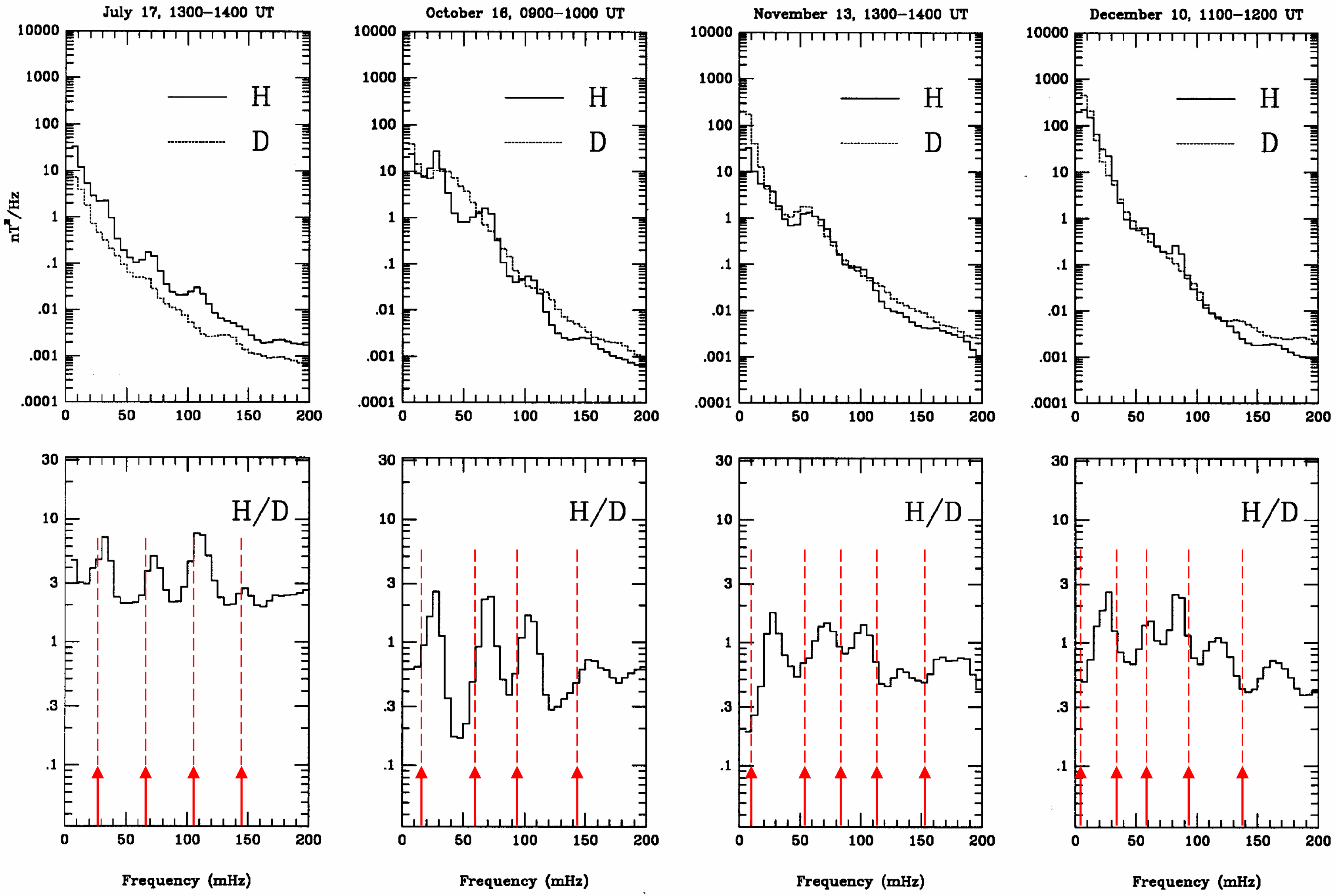

Gradient method for detecting field line resonances from ground-based ULF measurements

(*Baransky et al*., 1985; *Waters et al*., 1991)

Higher latitude field line → Lower resonant frequency (ω_N)

Lower latitude field line → Higher resonant frequency (ω_S)

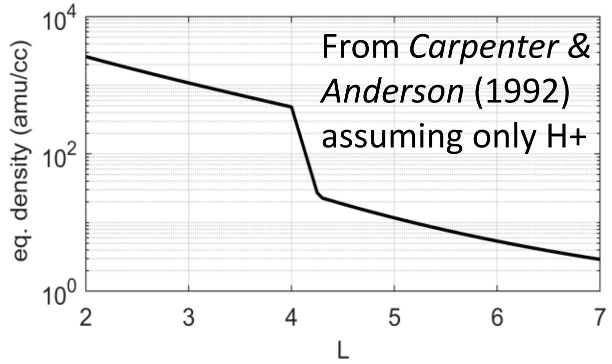

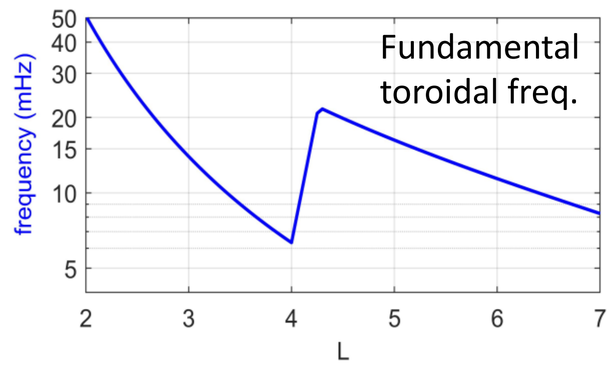

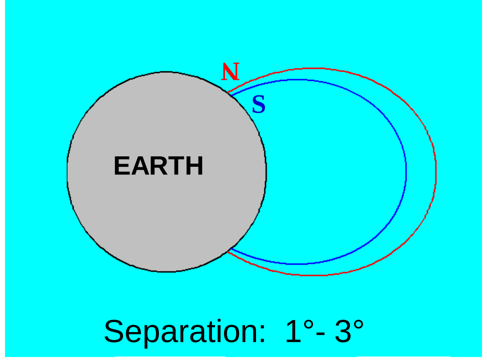

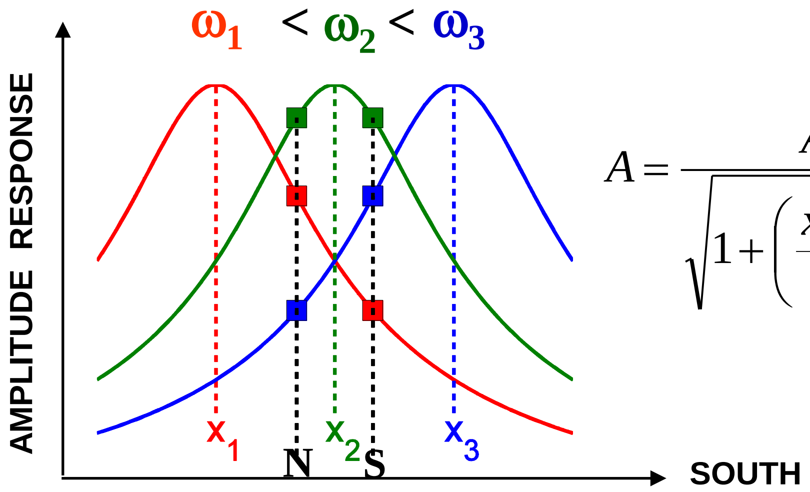

$$A = \frac{A_R(f)}{\sqrt{1 + \left(\frac{x - x_R(f)}{\varepsilon} \right)^2}}$$

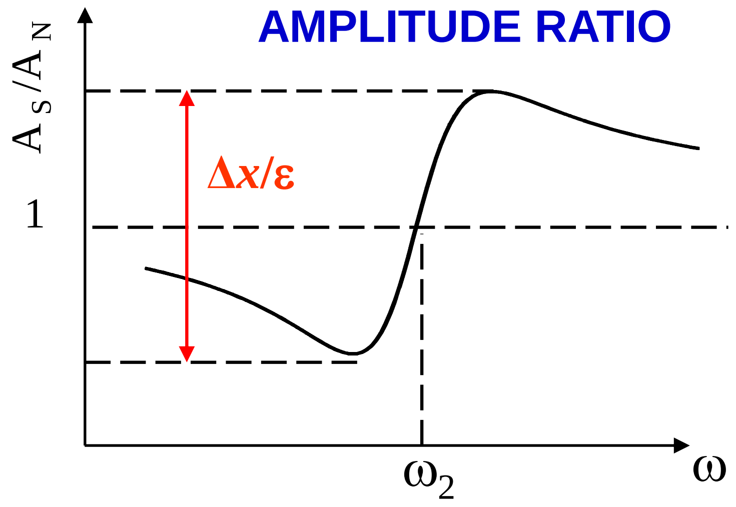

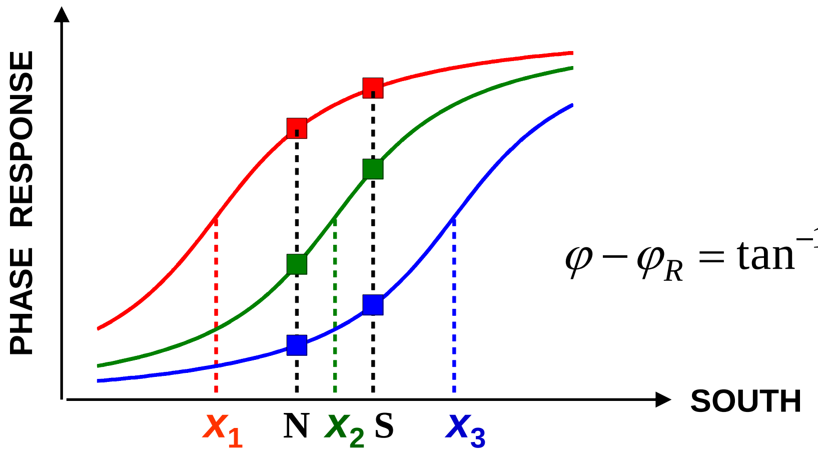

$$\varphi - \varphi_R = \tan^{-1}\left(\frac{x - x_R}{\varepsilon} \right)$$

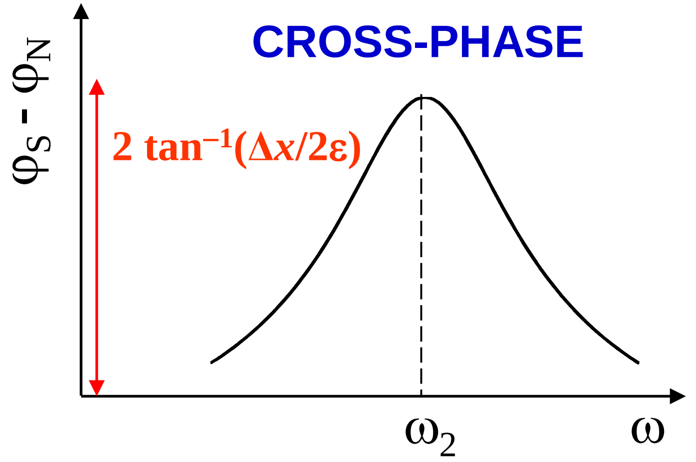

GRADIENT METHOD FOR DETECTING FIELD LINE RESONANCES FROM GROUND-BASED ULF MEASUREMENTS

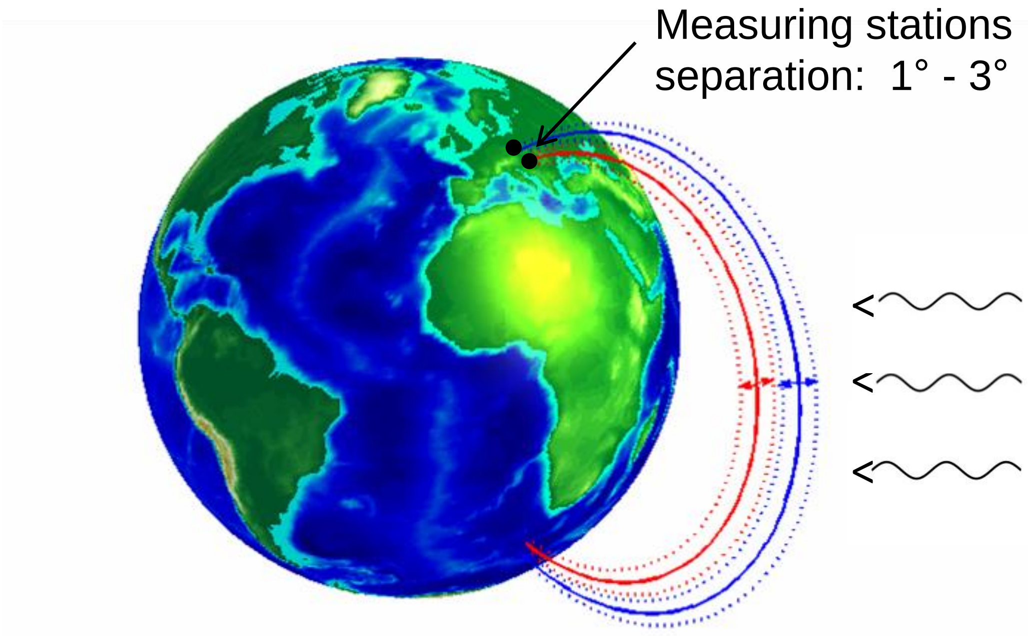

FREQUENCY RESPONSE OF TWO OSCILLATORS

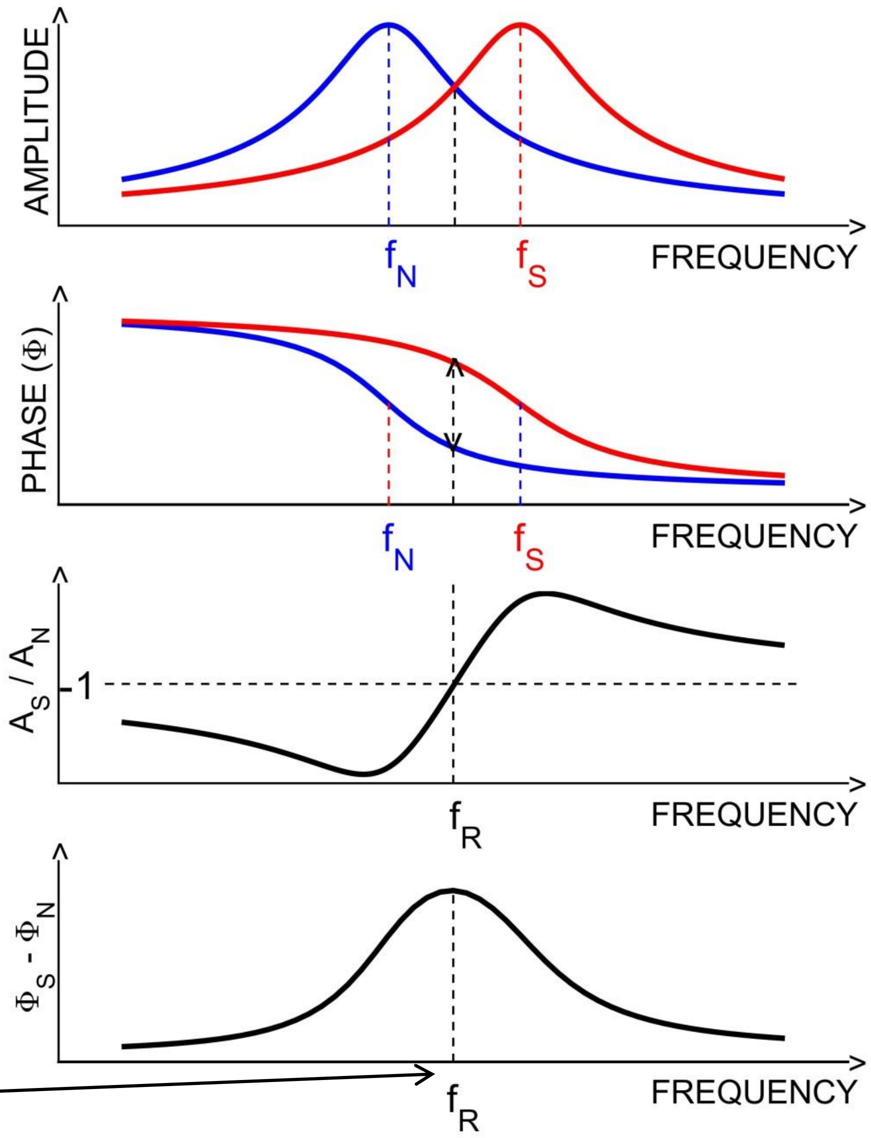

— Higher latitude field line → Lower resonance frequency (f_N)

— Lower latitude field line → Higher resonance frequency (f_S)

CROSS-PHASE TECHNIQUE

Resonance frequency at the middle point.

Identified by a maximum in the phase difference

An example of application of the gradient technique

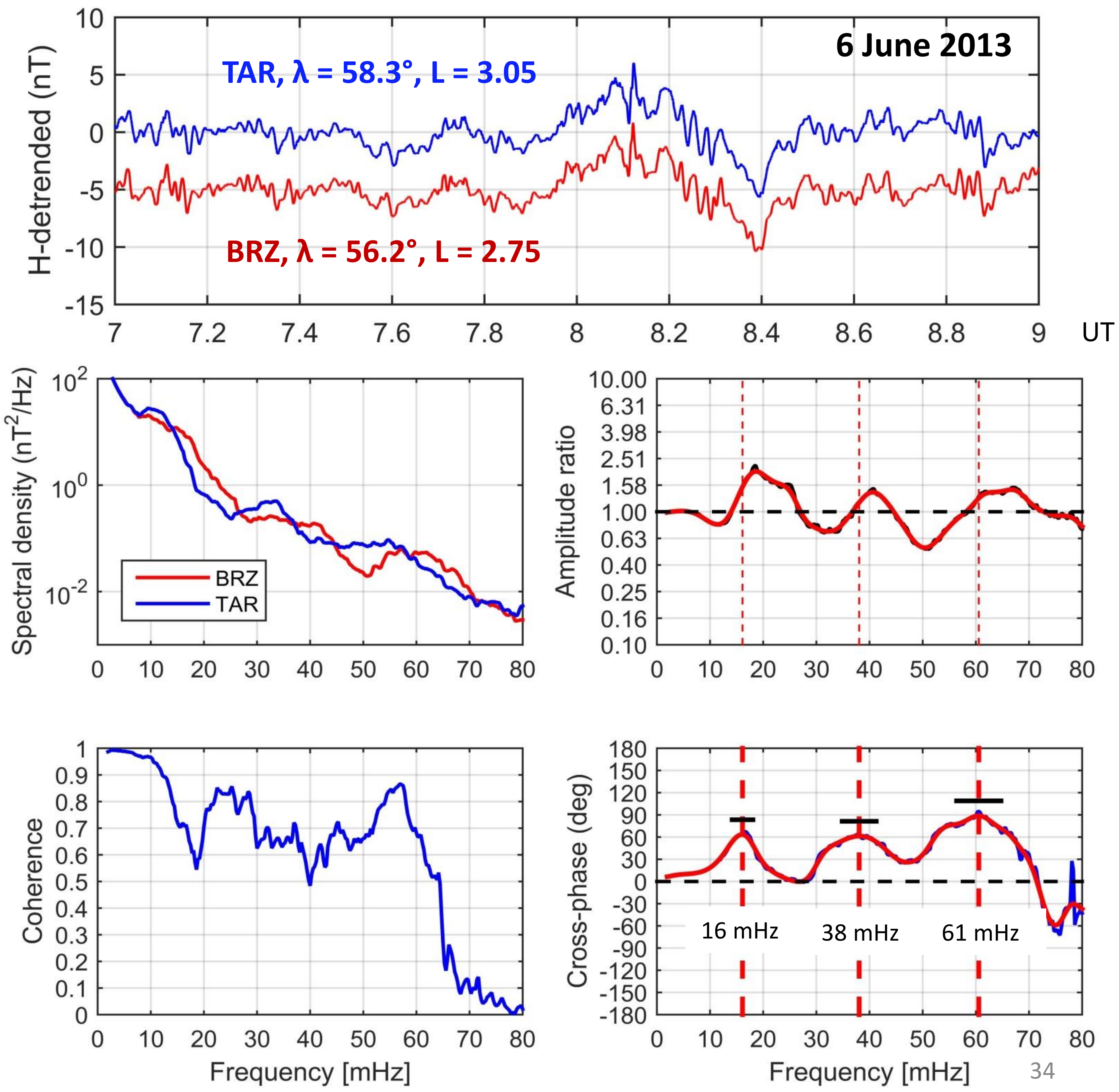

DYNAMIC CROSS-SPECTRA

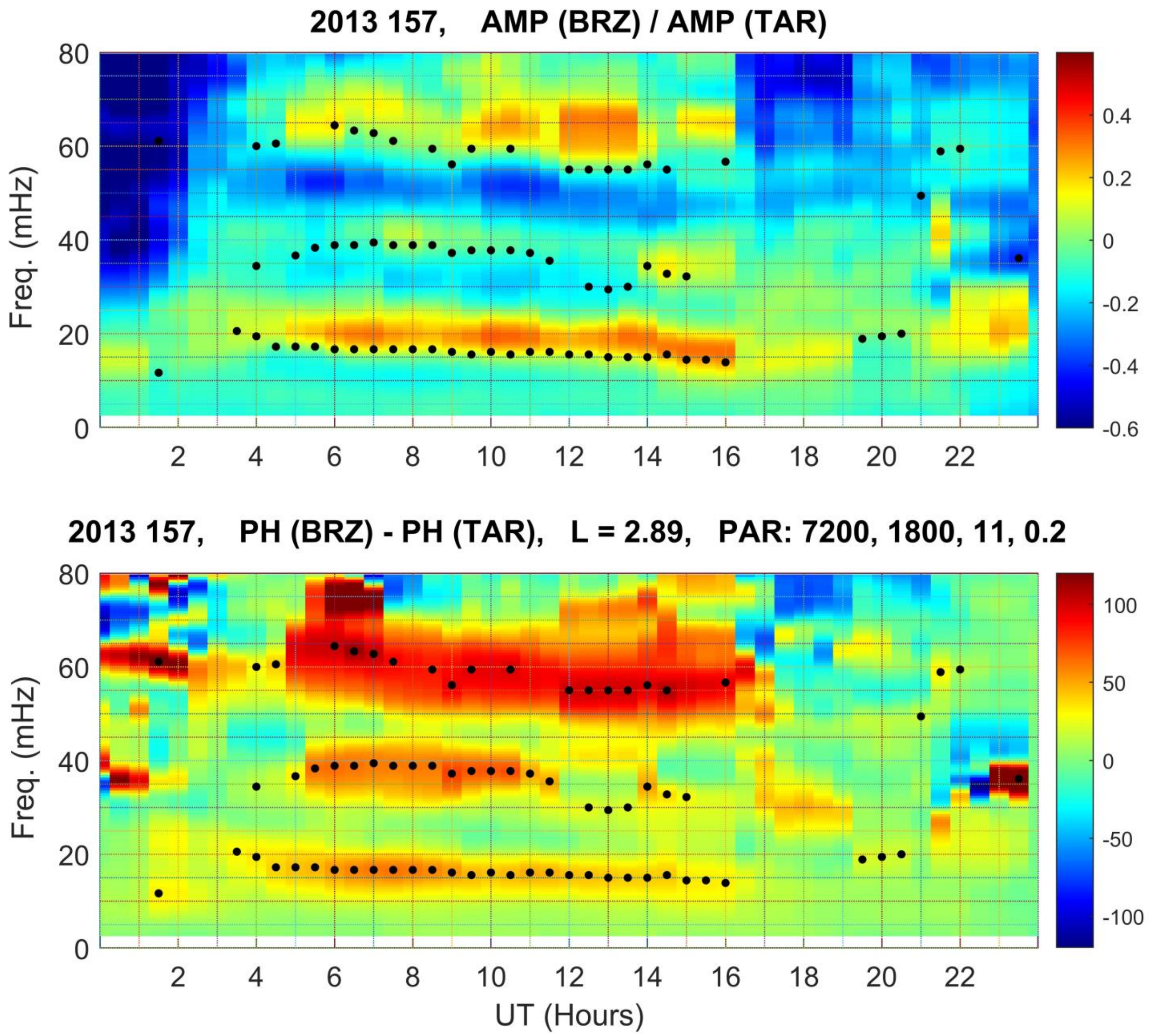

Diurnal variation at low latitudes

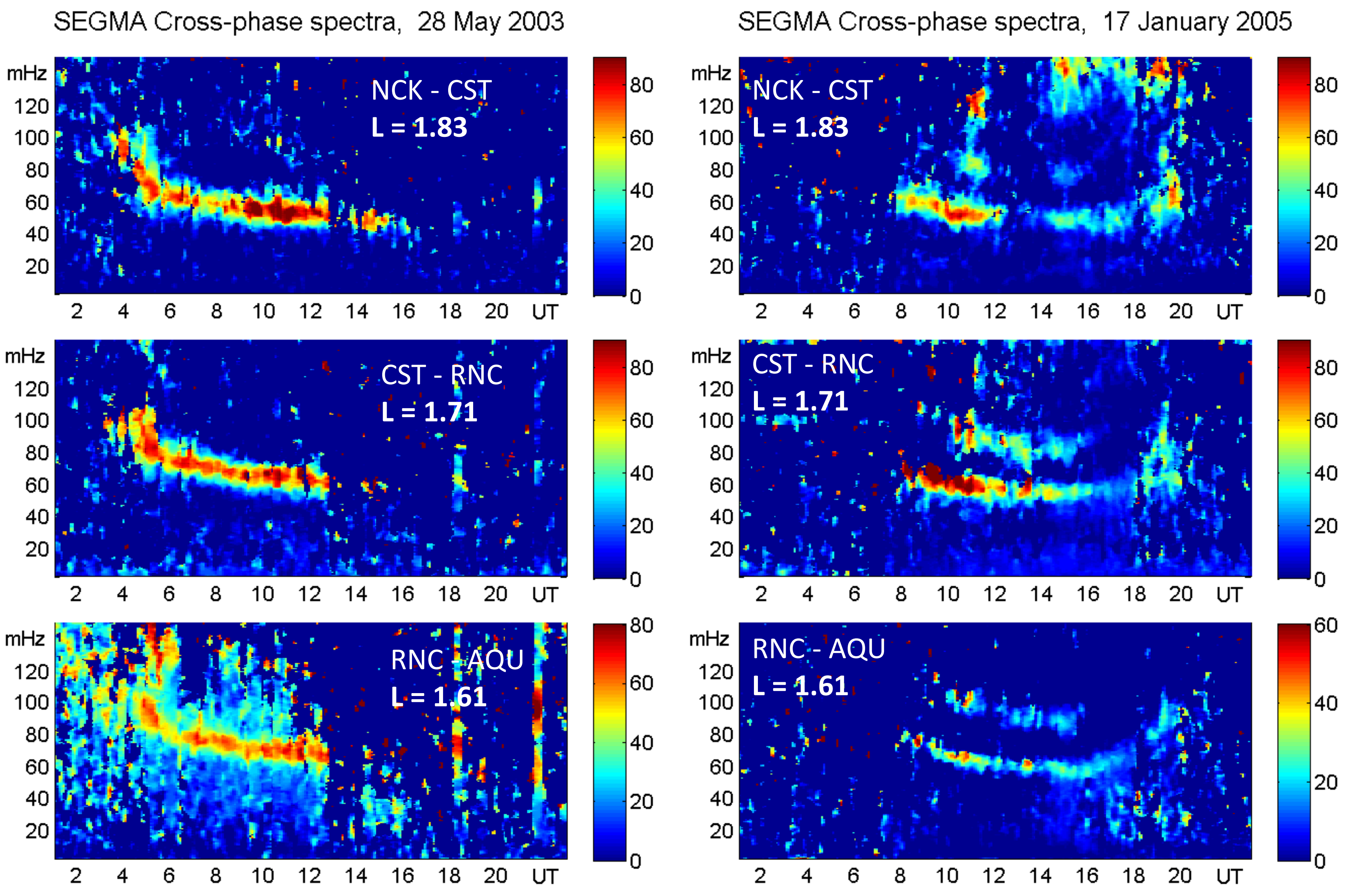

Other examples of diurnal variation using the cross-phase technique

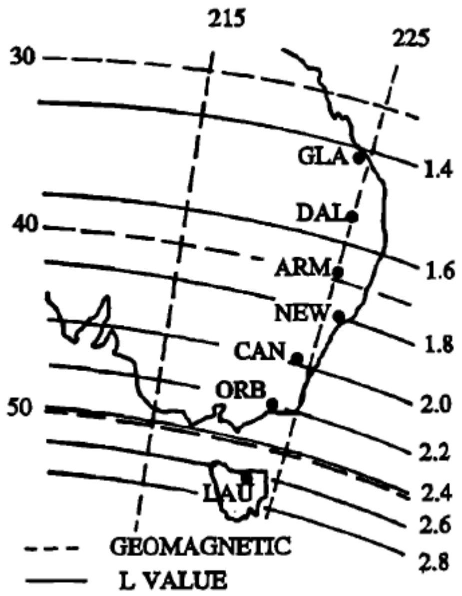

Observations at an eastern australian array (*Waters et al.*, 1994)

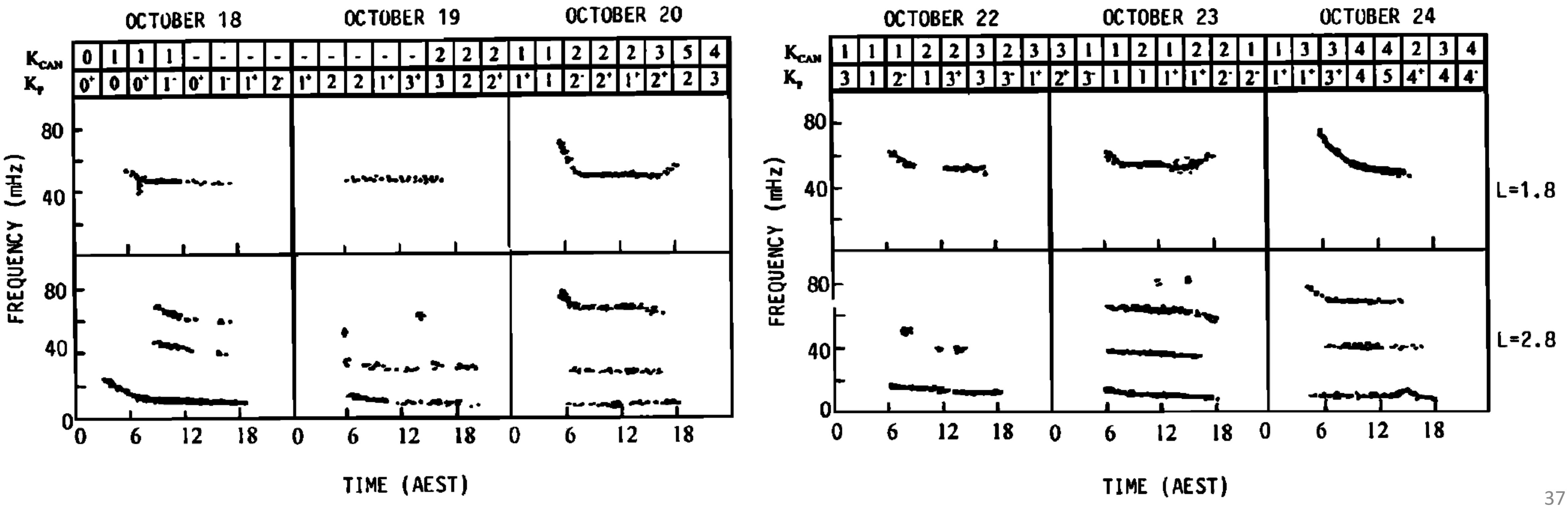

ANNUAL VARIATION OF THE FLR FREQUENCY AT *L* = 1.61, YEAR 2003

Vellante et al., 2007

DAILY AVERAGES (0900 – 1600 LT)

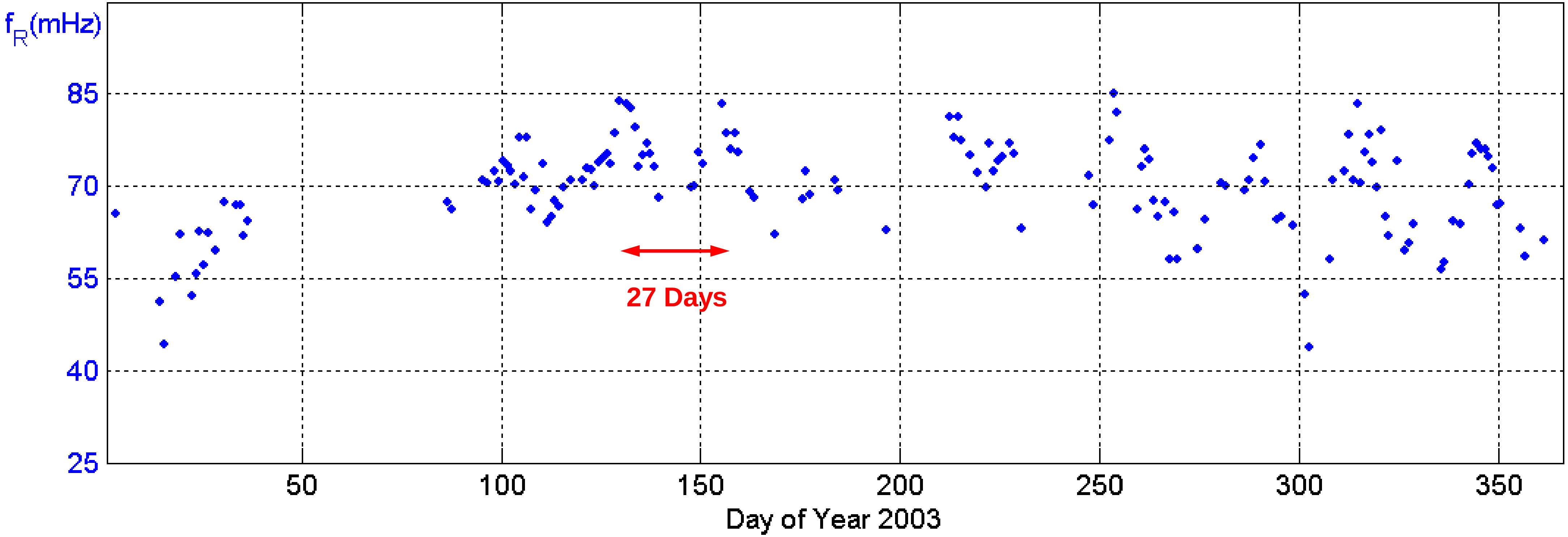

A nearly 27-days modulation appears, which must be connected to the recurrence of active regions of the Sun

SOLAR IRRADIANCE DEPENDENCE OF THE FLR FREQUENCY (L = 1.61)

Vellante et al., 2007

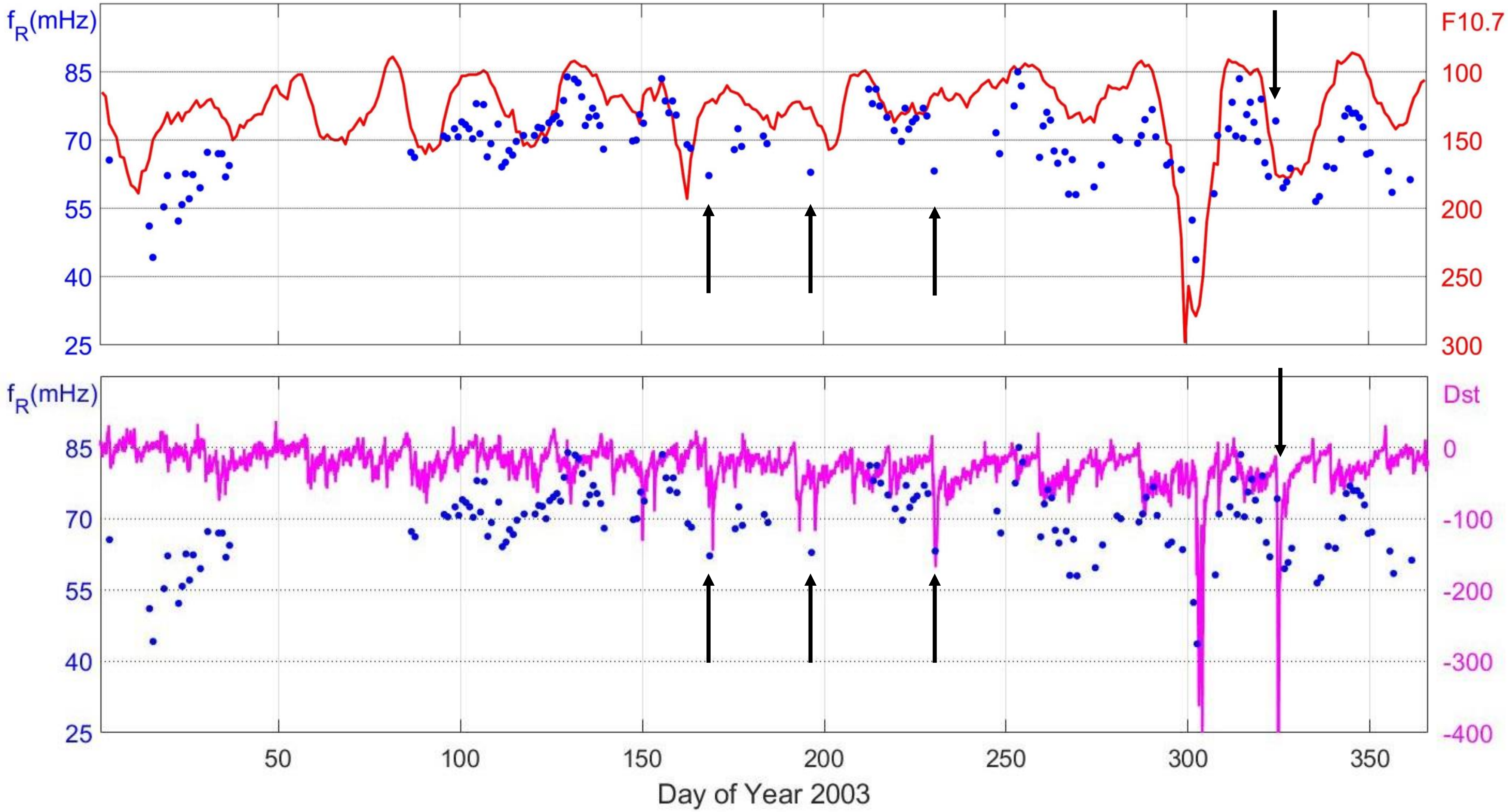

- **An increase of the solar EUV/X-ray radiation increases the ionization rate in the ionosphere. This influences the whole distribution of the plasma along the low-latitude field line through rapid diffusion.**
- **Values which more strongly depart from the F10.7 dependence are often associated with stormy periods following SSC.**

Linear regression analysis

Vellante et al., 2007

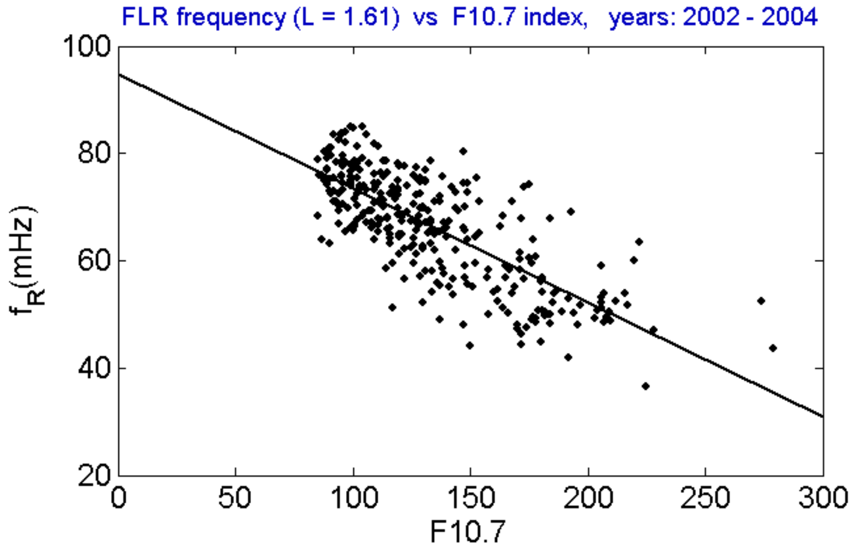

Experiment:

f_R [mHz] = **95 – 0.21 x F10.7**

corr. coeff. = 0.75

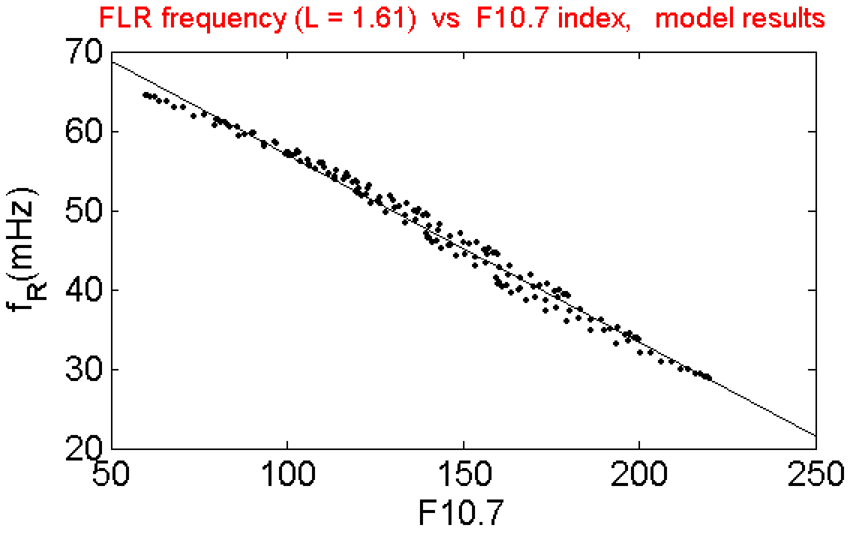

Model (Jakowski & Förster, 1995)**:**

f_R [mHz] = **81 – 0.24 x F10.7**

corr. coeff. = 0.99

CROSS CORRELATION ANALYSIS (f_R vs F10.7) L = 1.6, 2002-2004

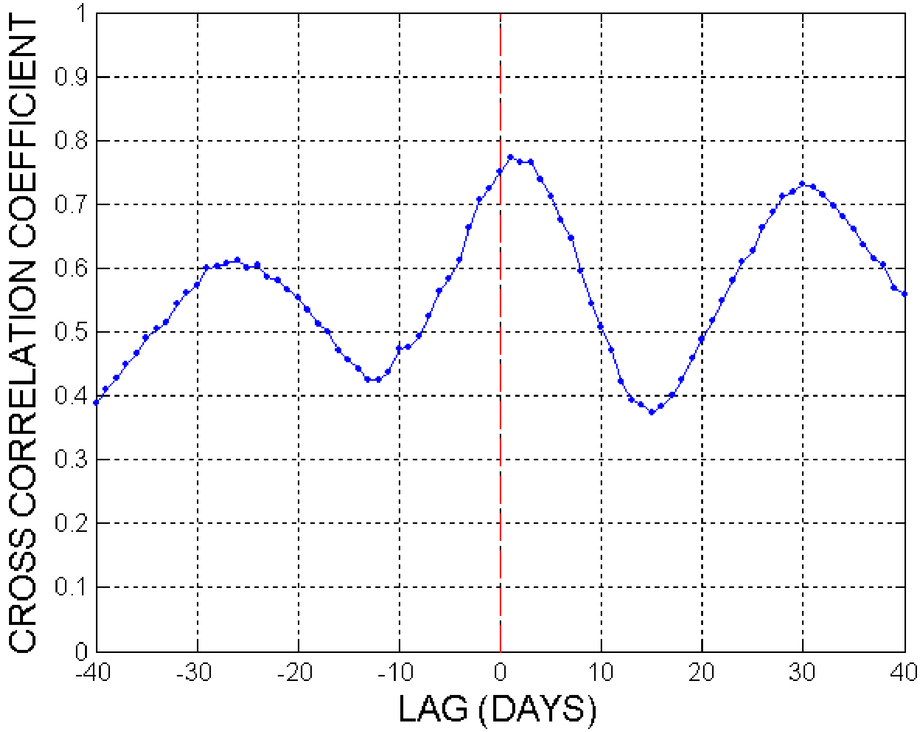

Vellante et al., 2007

- FLR frequency (plasmaspheric density) follows short-term (27 days) variations of the solar radiation with a time delay of 1-2 days.

- Similar delays found previously in atmospheric and ionospheric parameters.

- The delay in the ionospheric electron content was attributed to the delay of the atomic oxygen concentration to follow solar radiation changes (*Jakowski et al.*, 1991).

Solar Cycle Variation of the Field Line Resonant Frequency at L'Aquila (L = 1.56)

Vellante et al. (1996)

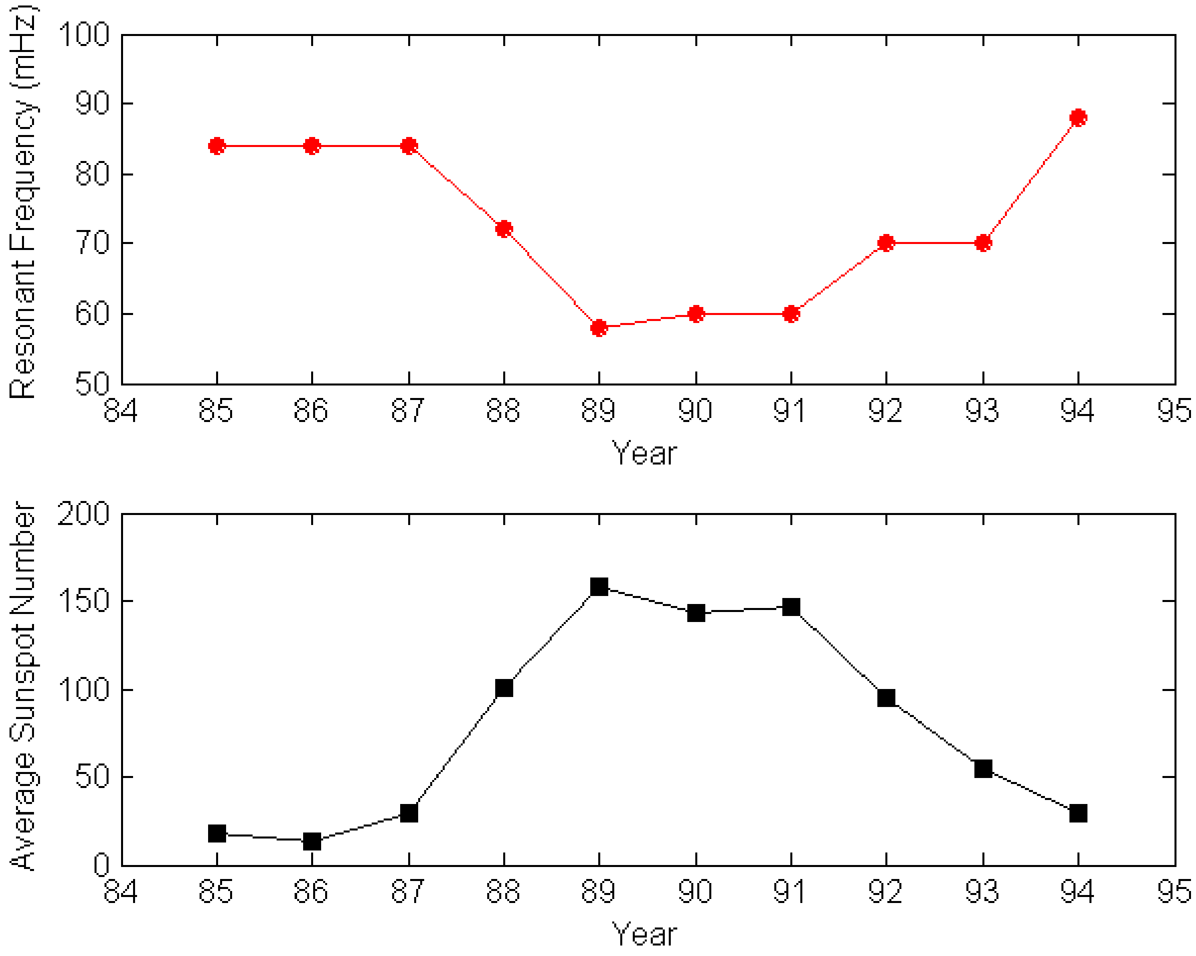

Assuming $\rho \propto f_r^{-2}$ ⟶ $\rho_{max} \approx 2\,\rho_{min}$

Annual variation

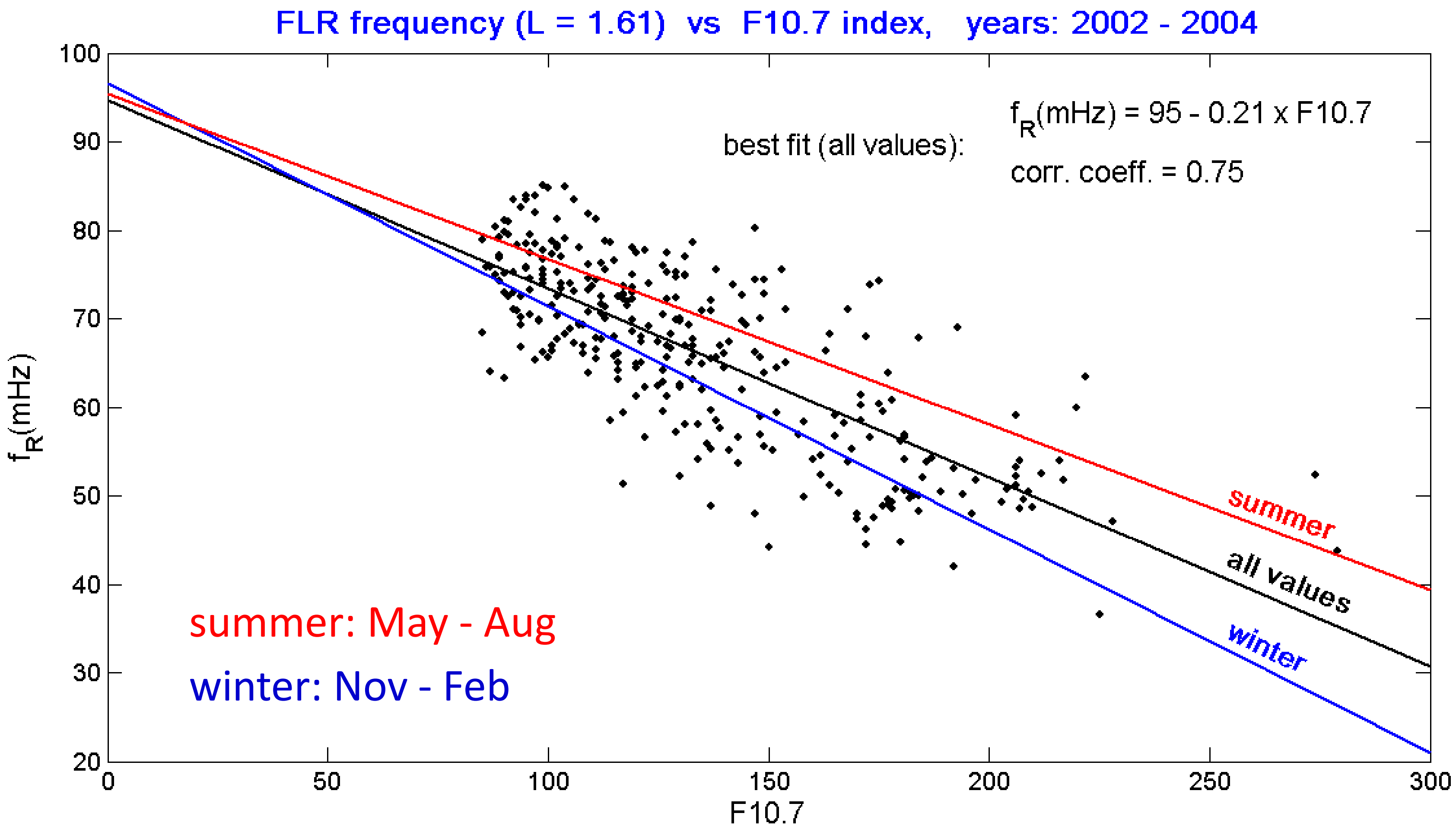

$f_{sum} / f_{win} \sim 1.1 \div 1.2$ ➡ $\rho_{win} / \rho_{sum} \sim$ **1.2 ÷ 1.4**

Higher ratios (~2-3) are found, for both ion and electron densities, in the American sector (e.g., *Berube et al*., 2003; *Menk et al*., 2012).

→ Higher asymmetry in the ionospheric solar illumination at opposite ends of the magnetic field lines (*Clilverd et al*., 1991).

PLASMON – A new, ground based data-assimilative modeling of the Earth's plasmasphere - a critical contribution to Radiation Belt modeling for Space Weather purposes

EU-FP7 Project, 2011-2104

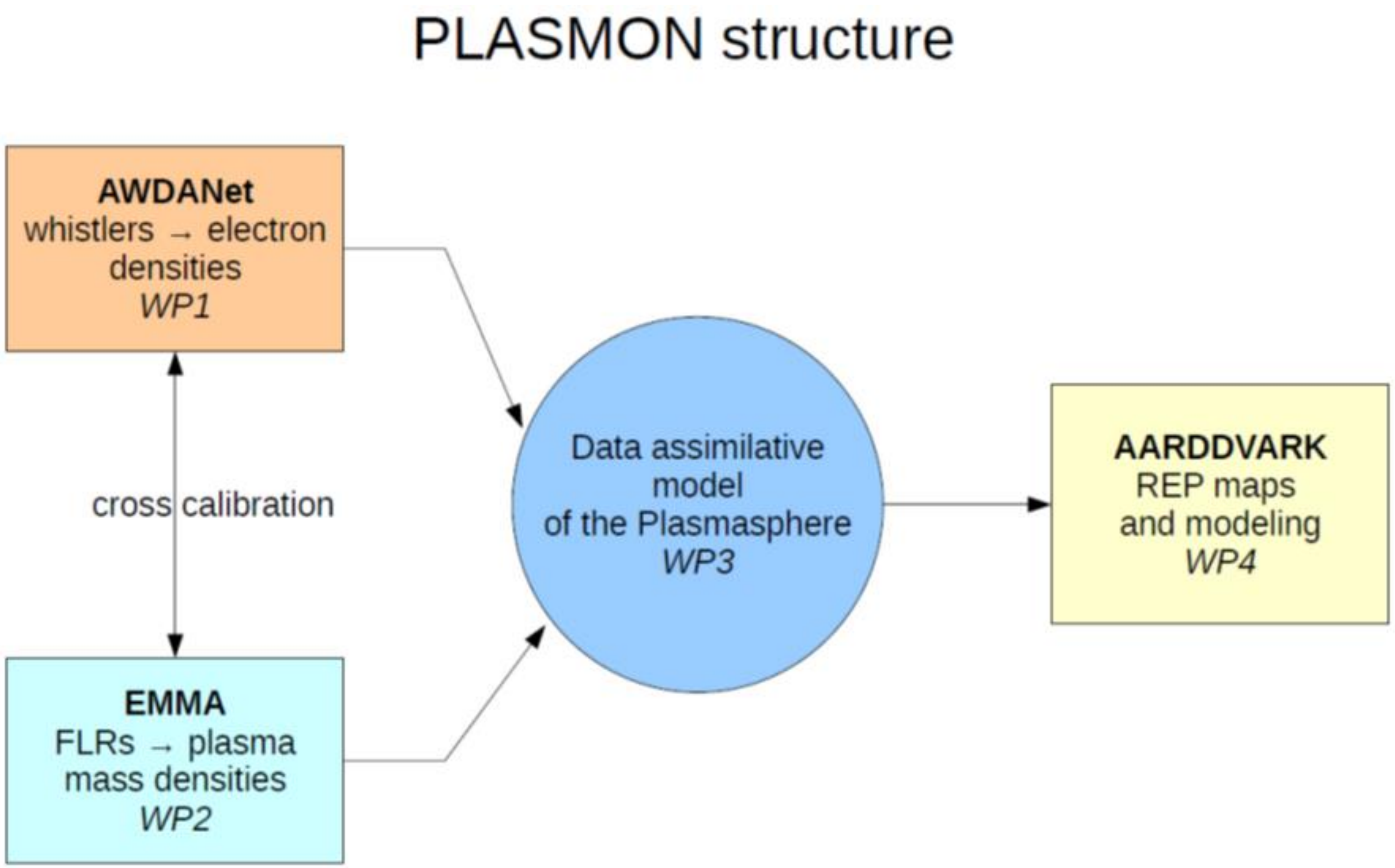

PLASMON 2nd annual meeting, Sodankyla Geophysical Observatory, 11-15 February 2013

EMMA (European quasi-Meridonal Magnetometer ARRAY), 1.5 < L < 6.5

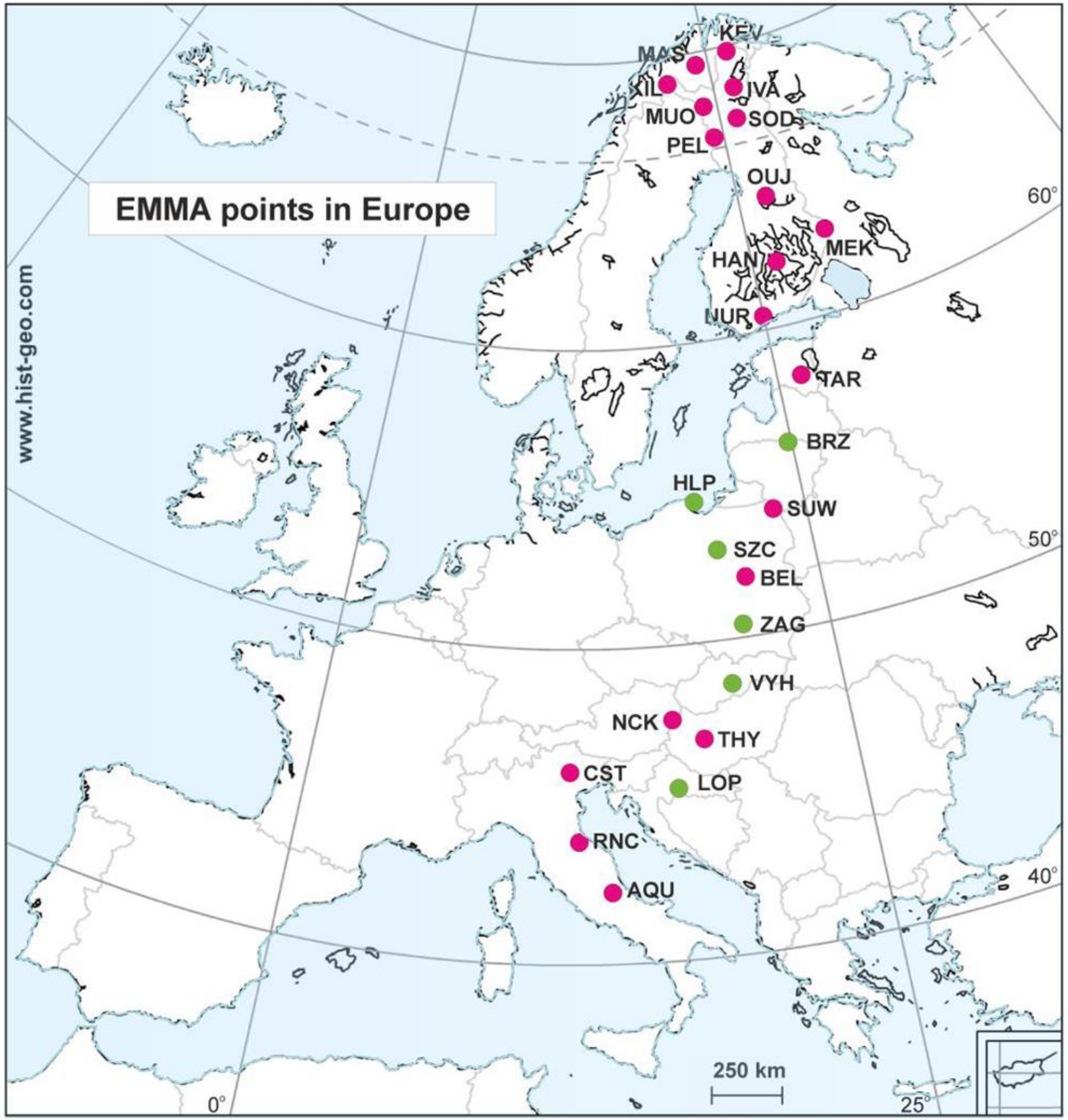

Established in the framework of a European project (PLASMON, *Lichtenberger et al*., 2013).

27 stations, all equipped with high sensitivity fluxgate magnetometers and GPS antenna for precise time recording.

All stations are remotely connected and transmit data to local servers every 1-15 min.

Data are collected at two main servers (one in Hungary and the other at University of L'Aquila) which continuously monitor the operational status of the whole network, and cyclically (every 15 min) run a procedure to detect FLR frequencies from several station pairs and deduce in near real time the equatorial plasma mass density in the *L*-range 1.6-6.1.

EMMA-Net Data Flow

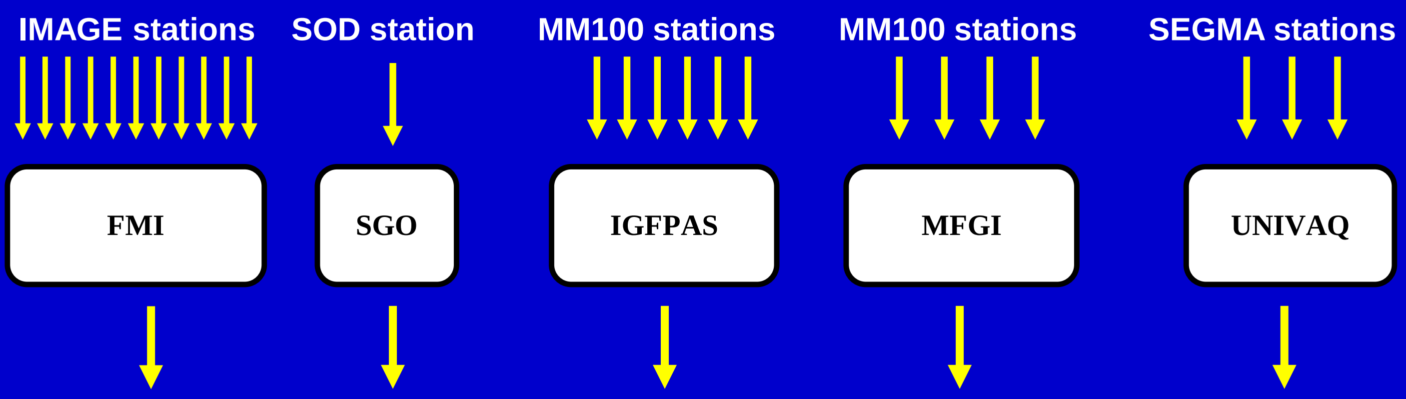

PLASMON EMMA Servers (L'Aquila; Tihany)

- **Conversion to EMMA Data Format (FMI stations)**
- **Transformation: XYZ → HDZ (if necessary)**
- **Removal of spikes, check of timing – correction**

Tihany Server

- **Implementation of FLRID**
- **Web-based monitor (http://geofizika.canet.hu/plasmon/):**

near real time magnetograms/power spectra/FLRID results

L'Aquila Server

- **Implementation of FLRID**
- **Implementation of FLRINV:**

results are stored in daily text files updated every 15 min and available for downloading

http://plasmonserver.aquila.infn.it/EMMA_FLR_DENSITY

FLR inversion (FLRINV)

The inversion algorithm converts FLR frequencies into estimates of the equatorial plasma mass density ρ_{eq} ($1.6 < L < 6.3$).

It solves numerically the MHD wave equation for the toroidale mode in an arbitrary field geometry (dipole, IGRF, **T02** models) and for a given density distribution along the field line: $\rho(s) = \rho_{eq} (r / r_{eq})^{-m}$, and infers ρ_{eq}.

T02 model (Tsyganenko, 2002). Input parameters:

- Universal Time: to determine the proper coefficients of the internal field (IGRF) and the tilt angle;
- Solar wind dynamic pressure;
- Dst index;
- IMF By and Bz components;
- G1, G2: take into account the prehistory state of the magnetosphere (determined by By, Bz, Vsw of the previous hour).

Near Real-time FLRINV process

Run every 15 min using:

- quasi real-time values of field line eigenfrequencies of all available station pairs (as computed by FLRID);
- solar wind and Dst parameters.

Real time solar wind data taken from the NOAA Space Weather Prediction Center which provides the latest 2 hours of magnetic and plasma data of the ACE satellite located at the L1 libration point: http://services.swpc.noaa.gov/text/ace-magnetometer.txt; http://services.swpc.noaa.gov/text/ace-swepam.txt

Data are time-shifted to take into account the propagation time of the solar wind from the satellite position to the Earth (typically about 1 hour).

Propagated data are resampled at fixed times and hourly running averages (time step 1 min) are produced.

Real-time Dst data are taken from the Dcx server of the University of Oulu, Finland:

http://dcx.oulu.fi/DstDcxDxtData/RealTime/Dxt/DxtRT.txt

Ground-based plasmasphere monitoring animation

Thanks to *Alfredo Del Corpo*

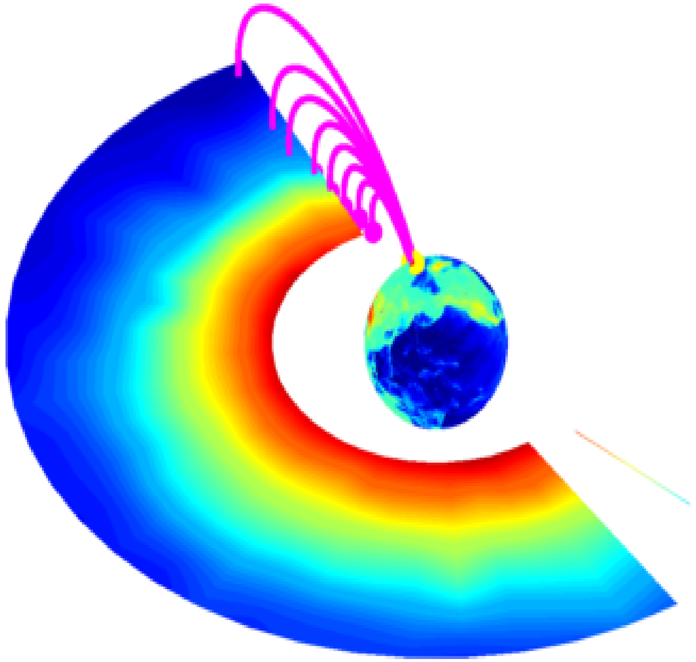

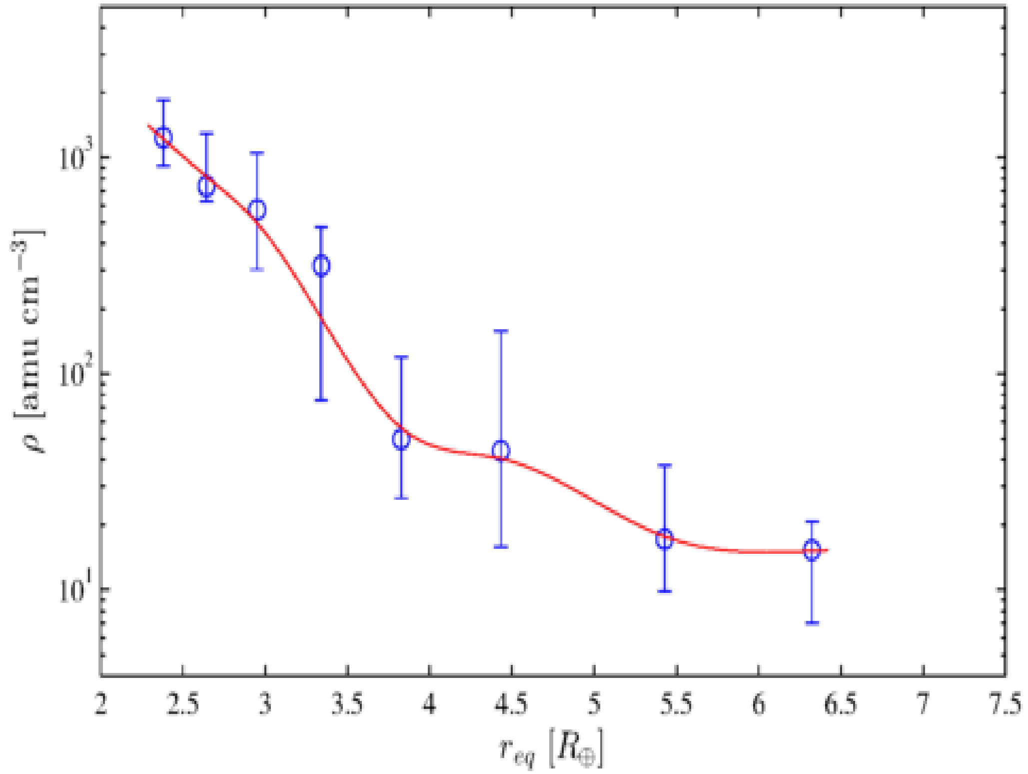

Statistical results (165 days in 2012-2017, 8 EMMA station pairs) *Del Corpo et al.*, 2019

Radial profiles – geomagnetic activity dependence

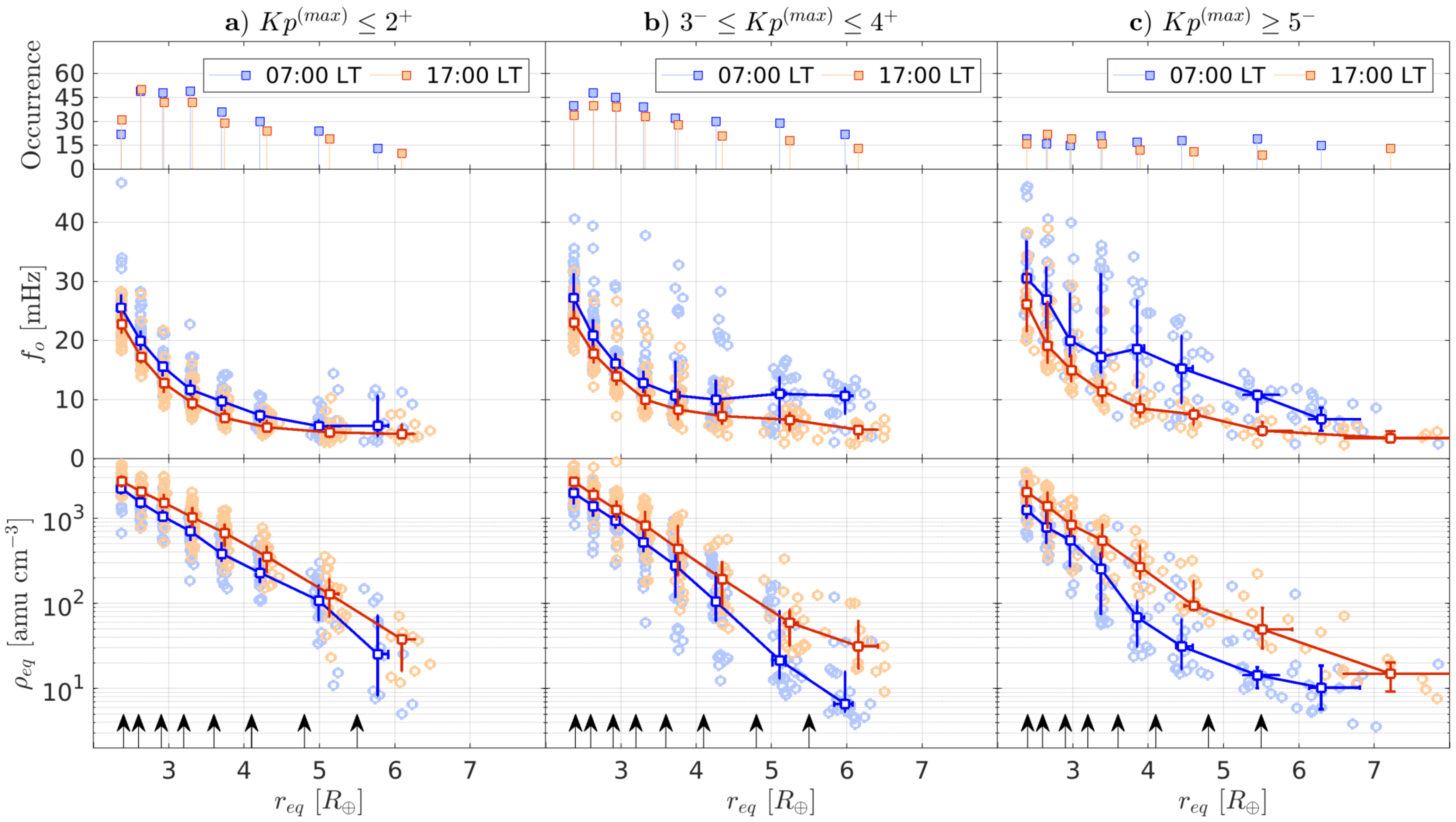

Densities obtained using TS05 and power law index *m* = 1.

Afternoon densities greater than in the morning --> refilling.

Plasmapause signature more evident for disturbed conditions and in the morning.

Plasmapause distance decreases with increasing disturbance level.

Map of the average plasma mass density distribution (*Del Corpo et al*., 2019, 2020)

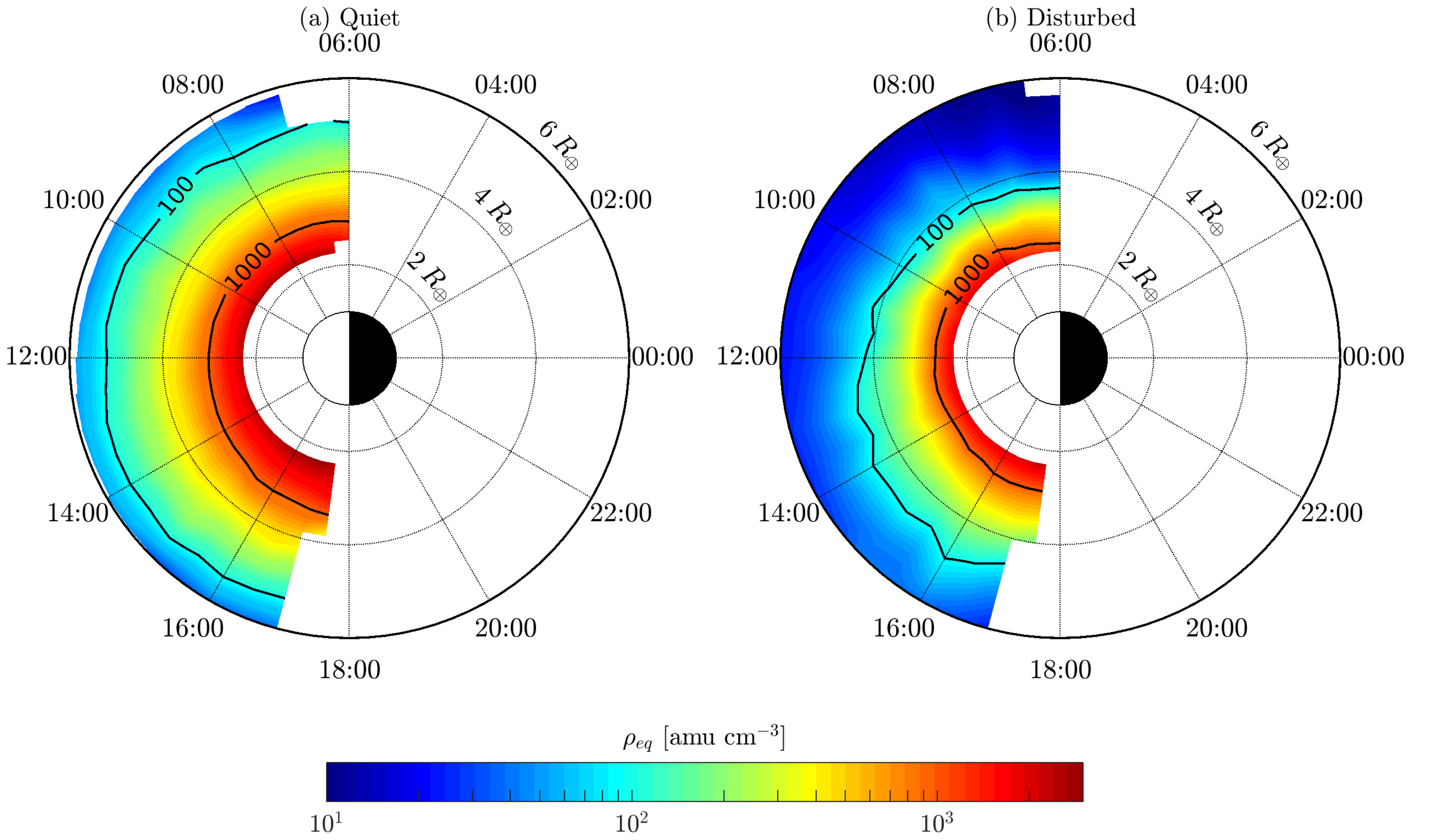

Plasmasphere density model (EMMA observations) $2.3\ R_E < r_{eq} < 4.5\ R_E$, $K_{p,max} <= 2^+$

$$\rho_{eq,ps} = \left\{477 + 171\cos\left[\frac{2\pi}{24}(LT - 20.24)\right]\right\}\left(\frac{r_{eq}}{4}\right)^{-3.34+0.56\cos\left[\frac{2\pi}{24}(LT-18.5)\right]}$$

Del Corpo et al., 2020

LT dependence

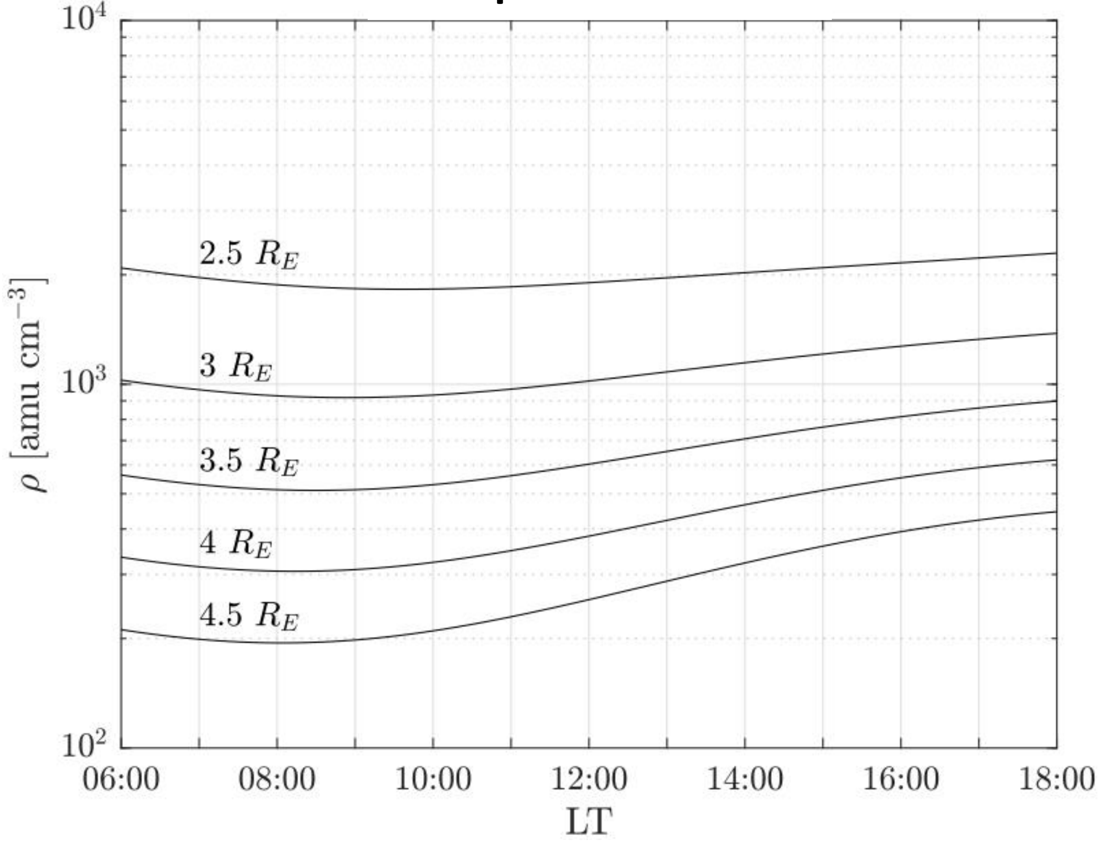

Radial dependence

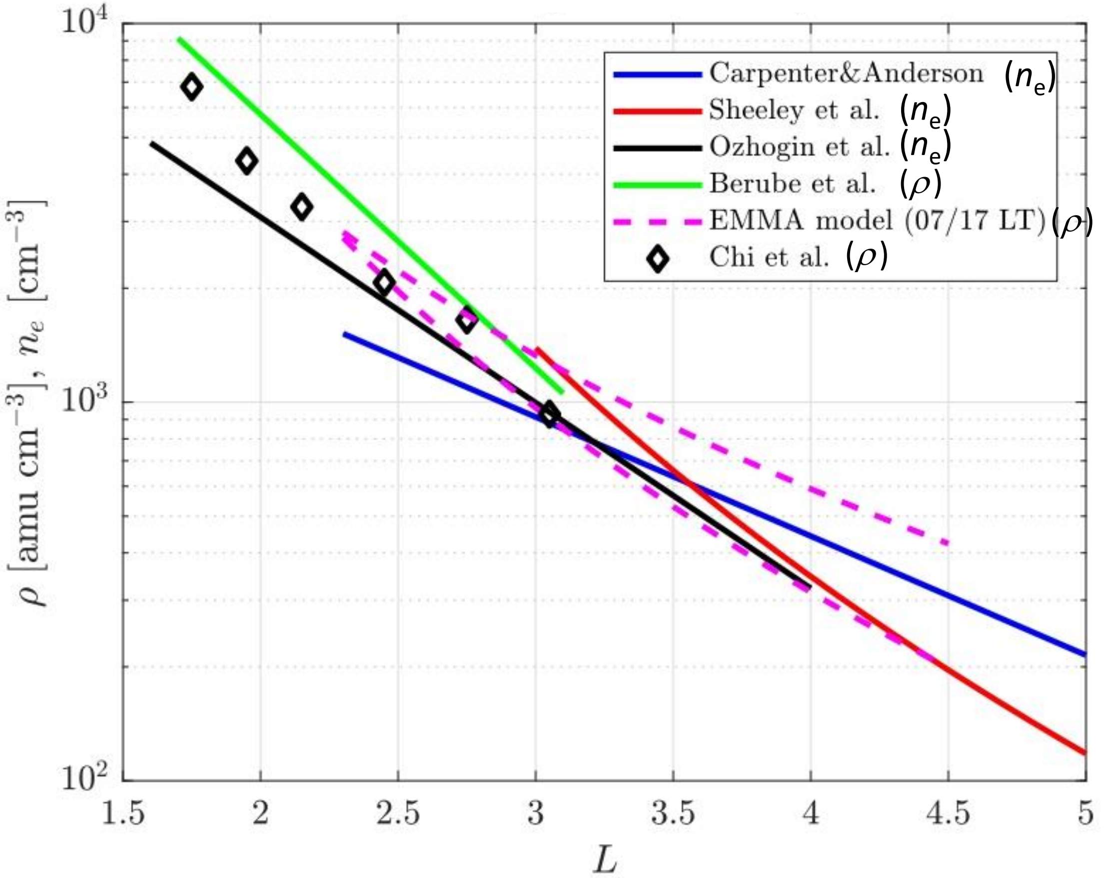

Unlike electron density models, the plasmasphere mass density model includes a LT dependence.

More pronounced LT variation at higher *L* probably reflects a more frequent replenishment condition at higher *L* flux tubes.

Plasmatrough density model (EMMA observations) $3.8\ R_E < r_{eq} < 8\ R_E$, $K_{p,max} >= 5^-$

Del Corpo et al., 2020

$$\rho_{eq,pt} = [30 + 17.4\,(LT-6)]\left(\frac{r_{eq}}{4}\right)^{-3.65\,-0.112\,(LT-6)}$$

LT dependence, r_{eq} = 4 R_E, 7 R_E

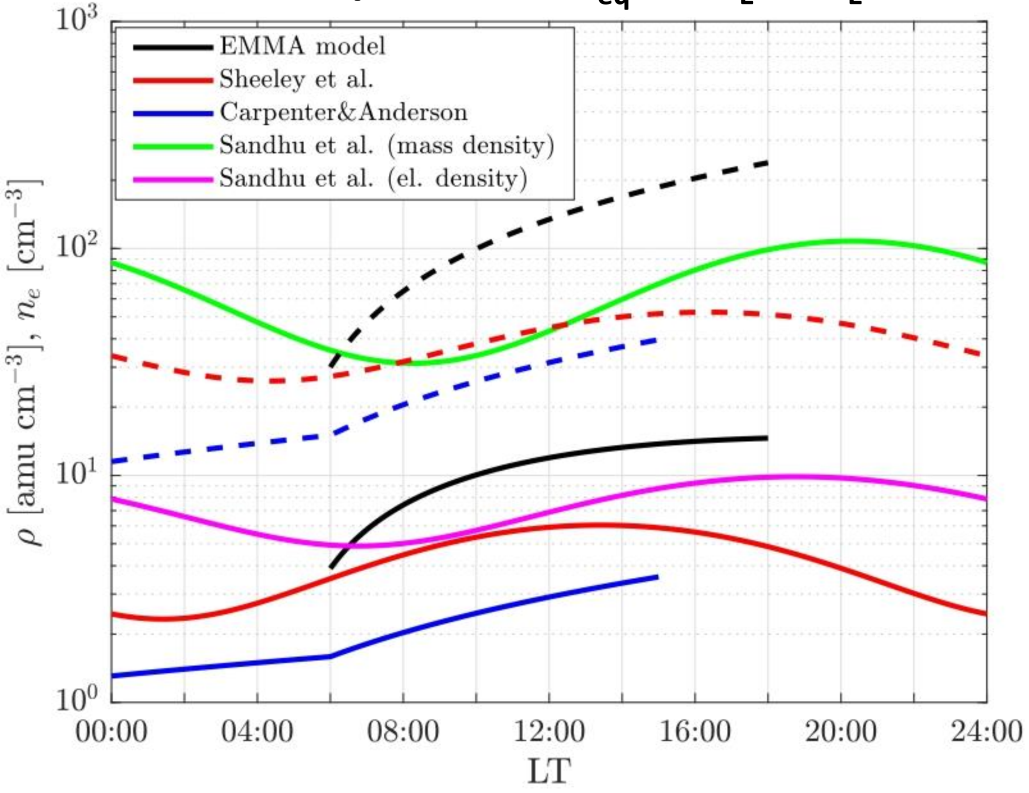

Radial dependence, LT = 12

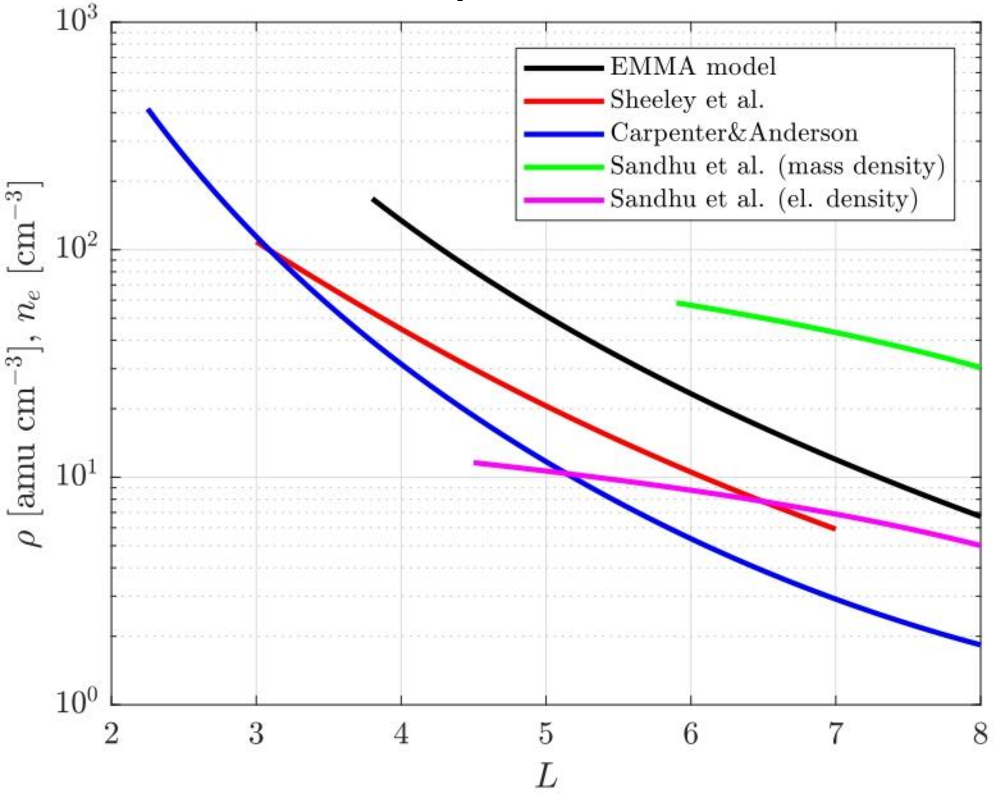

Plasmapause signatures on the ground - EMMA observations (*Heilig et al.*, 2014)

Equatorial profile

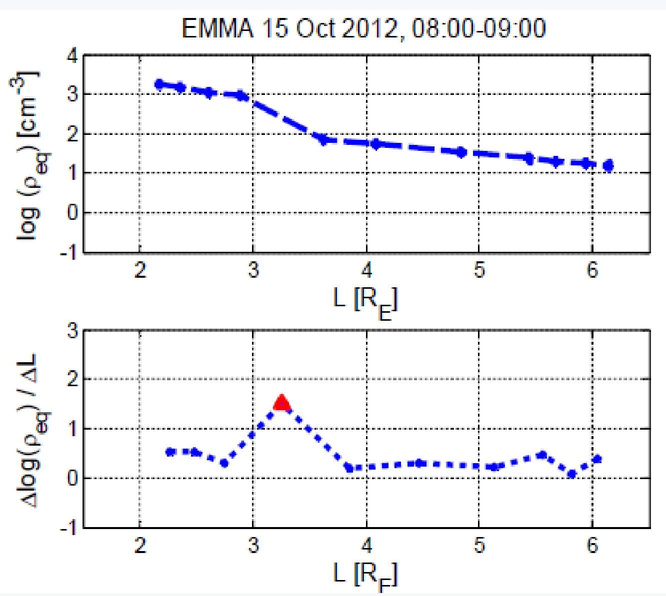

L-profile of equatorial plasma mass density inferred from EMMA observations. PP is depicted as a red triangle.

Abrupt density changes

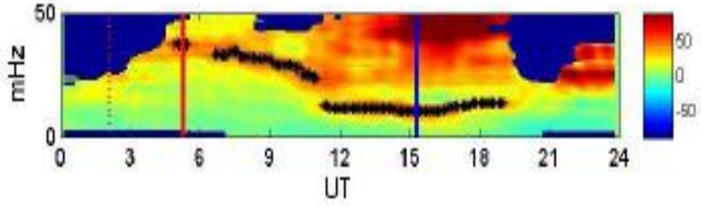

Abrupt changes in the observed FLR frequency (and as a consequence) in plasma mass density is also indicative of PP crossing. It means that the PP crossed the field lines that map to the stations on the ground.

Cross-phase drop-outs

Two stations straddling the plasmapause may have the same eigenfrequency, the cross-phase will be then near zero (*Milling et al.*, 2001; *Menk et al.*, 2004).

Cross phase reversals

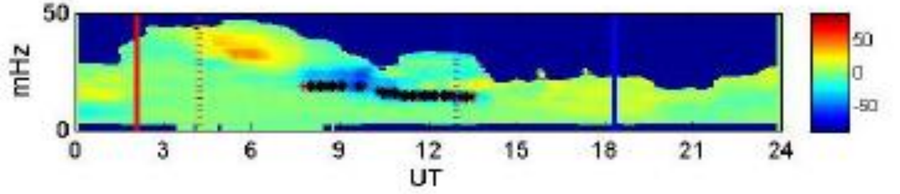

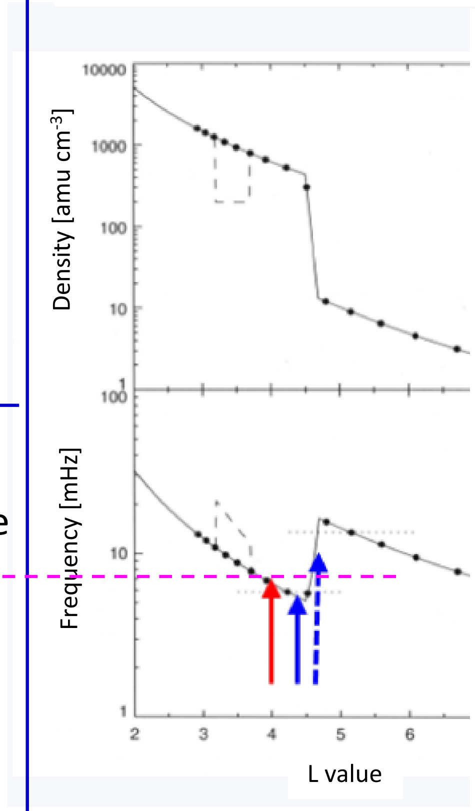

(*Menk et al.*, 2004)

Typically the FLR frequency at the poleward station is smaller than at the equatorward station (solid red and blue arrows). However, at a steep plasmapause (steeper than r^{-8}, *Kale et al.*, 2007) the opposite can occur (solid red and dashed blue arrows). In such a case both the cross phase and the amplitude spectra are reversed. The FLR frequency can be identified where the cross phase has a minimum.

Some examples of derived plasmapause profiles

IMAGE/SAMNET arrays

(Menk et al., 2004)

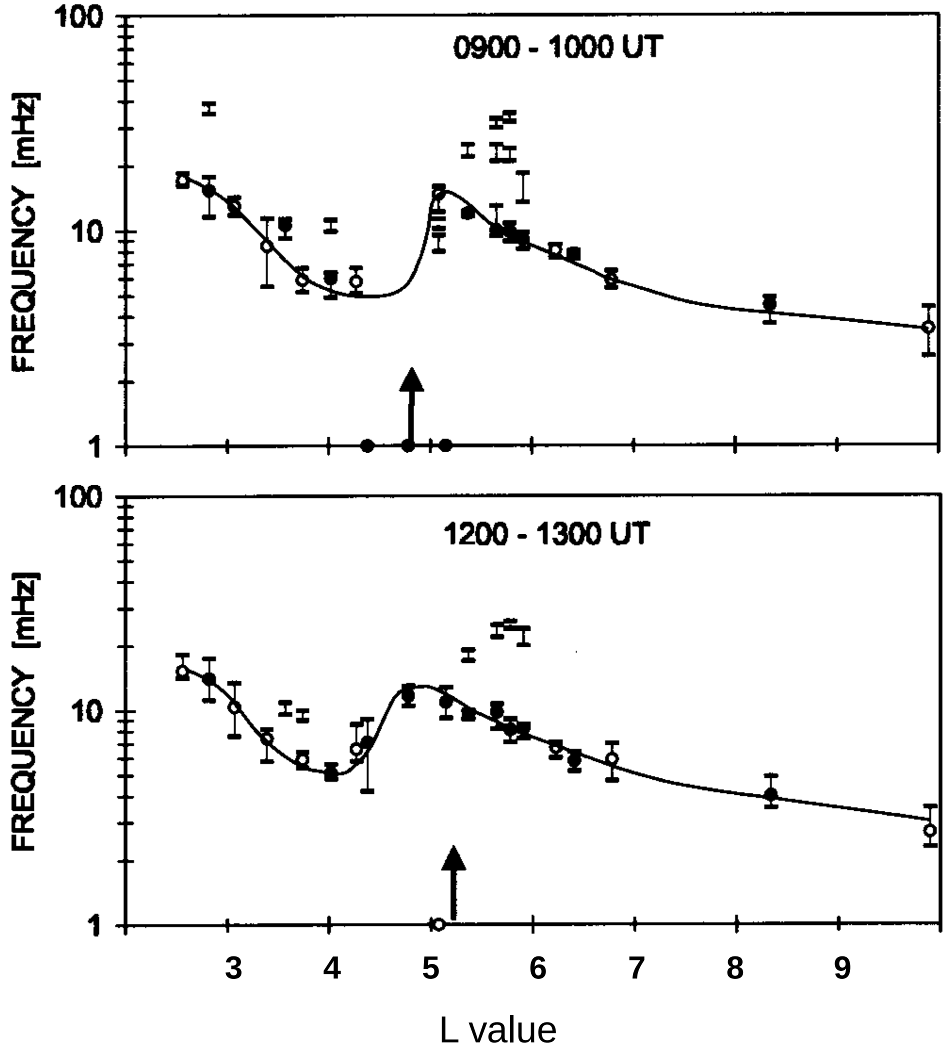

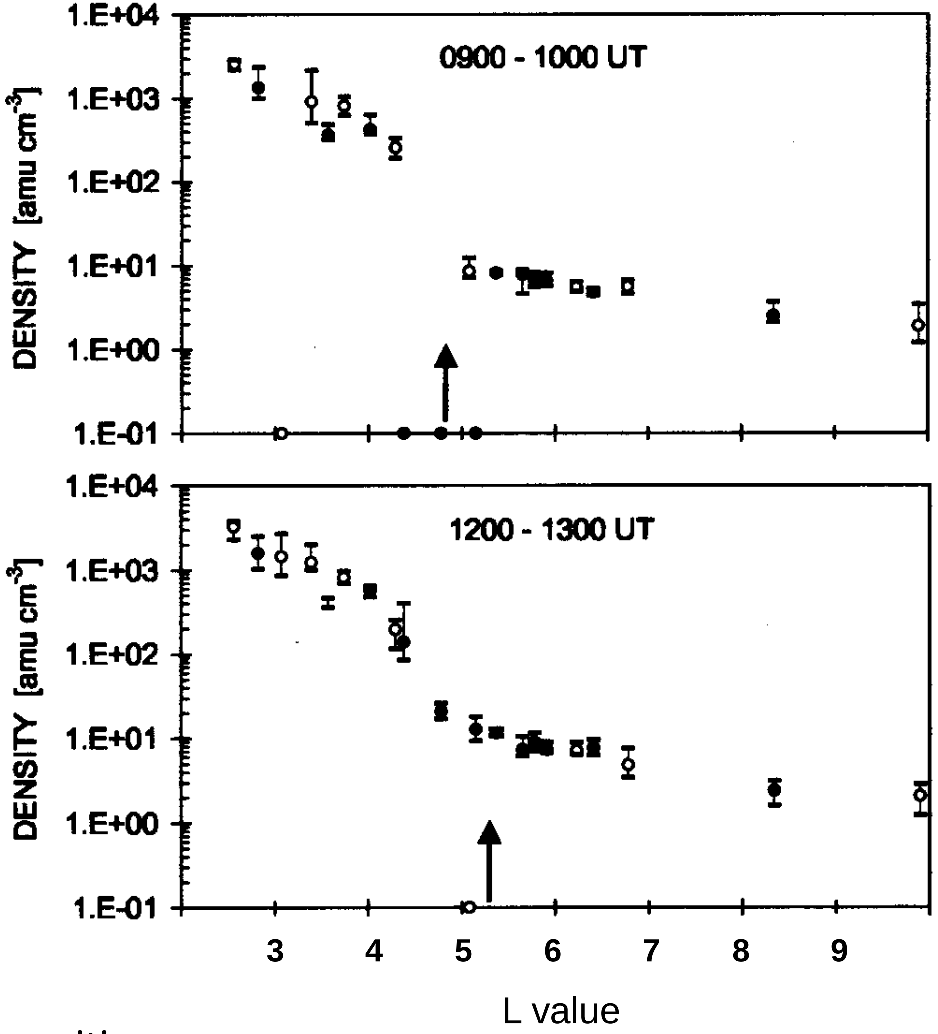

Predicted PP position

Caveats on density retrieval near the plasmapause

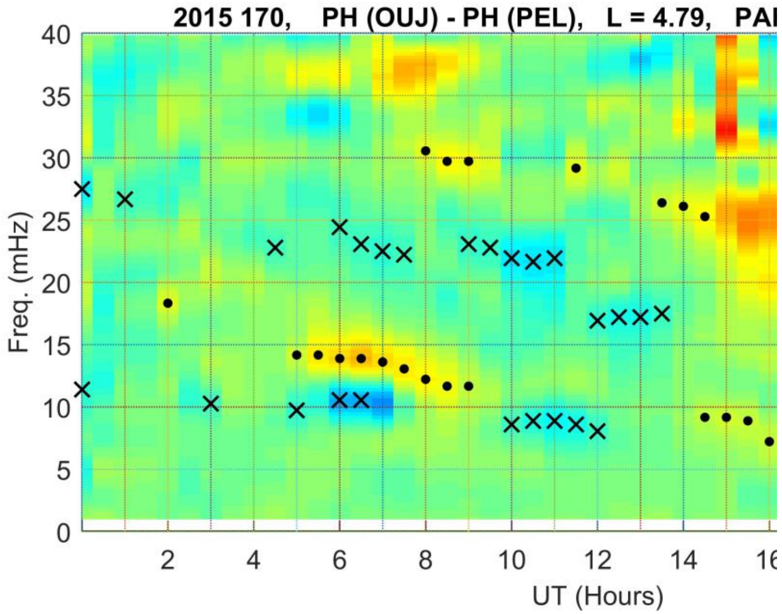

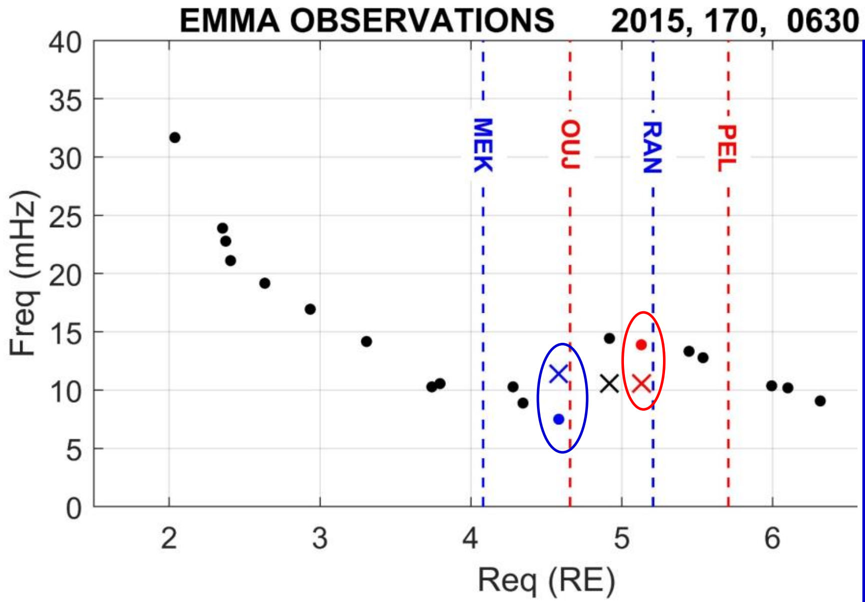

The simultaneous presence of peaks of opposite polarity is probably due to the <u>resonance width</u> being larger than the <u>plasmapause width</u>. So, when the station pair maps near the plasmapause, the stations sense the contribution from different regions (plasmasphere, plasmapause, trough) with weights depending on the station location, and frequency. As a result, a cross phase peak may not be related to the resonance frequency of the mid point.

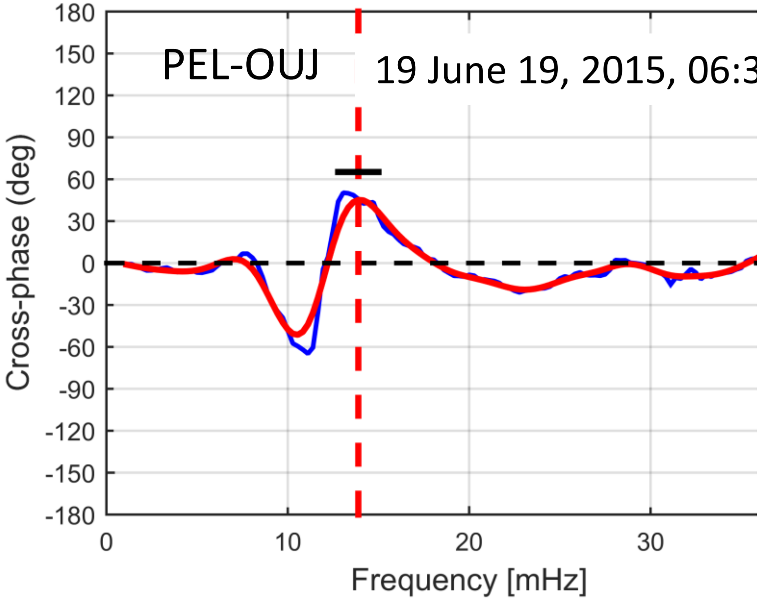

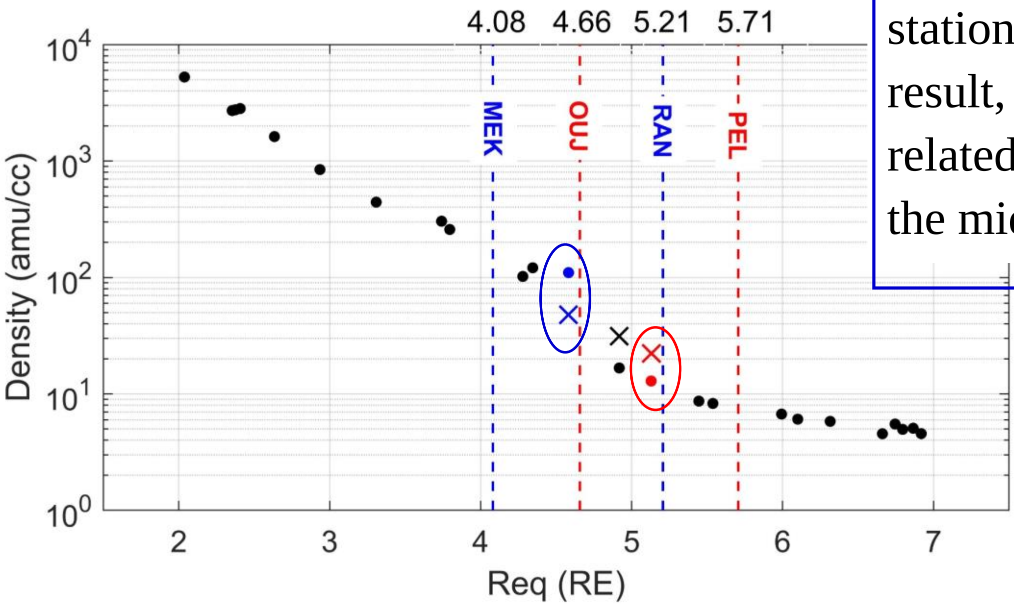

Plasmapause model (EMMA observations)

Del Corpo et al., 2020

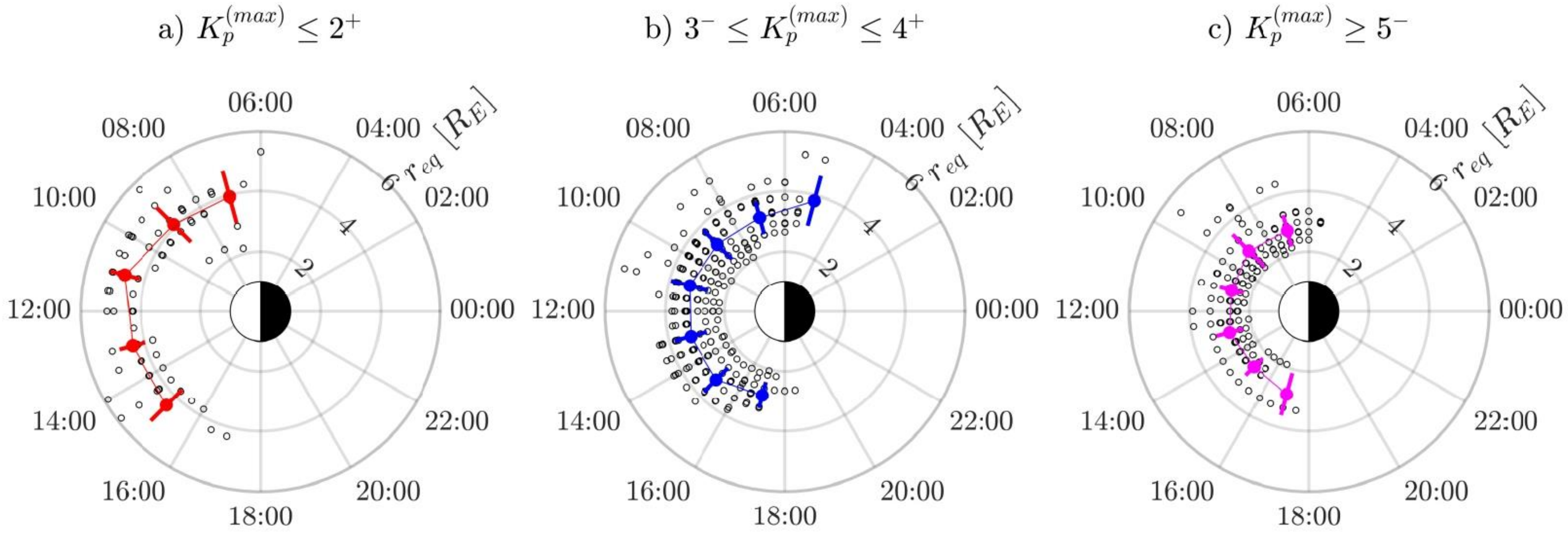

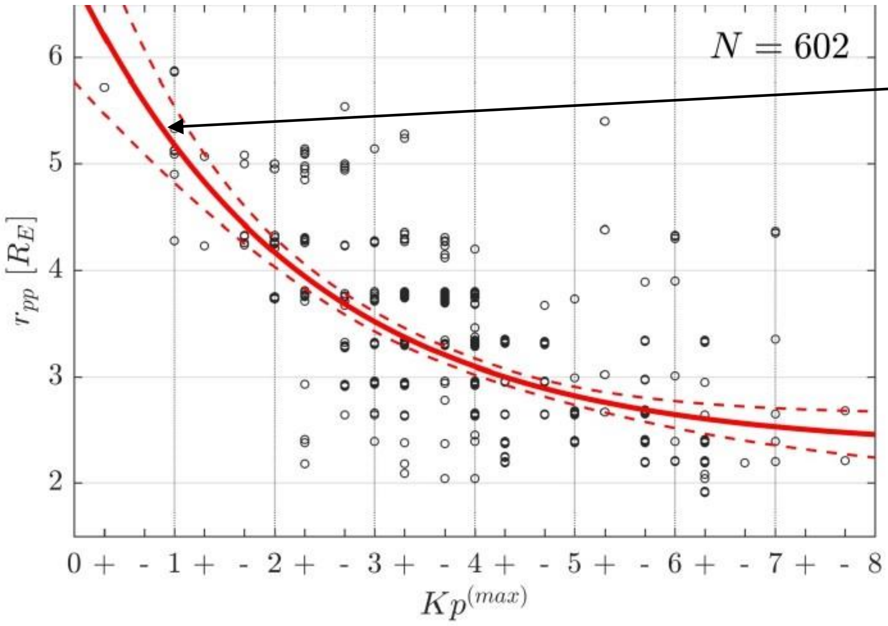

$$r_{pp} = 4.42\ e^{-0.44\ Kp^{(max)}} + 2.32$$

Generally, radial mass density profiles are characterized by a less steep plasmapause, confirming expectations (*Fraser et al.*, 2005). Plasmapause location shows a clear dependence on the geomagnetic activity level, while no evident local time dependence is observed.

Plume detection

An example from SAMNET/IMAGE arrays (*Grew et al.*, 2007)

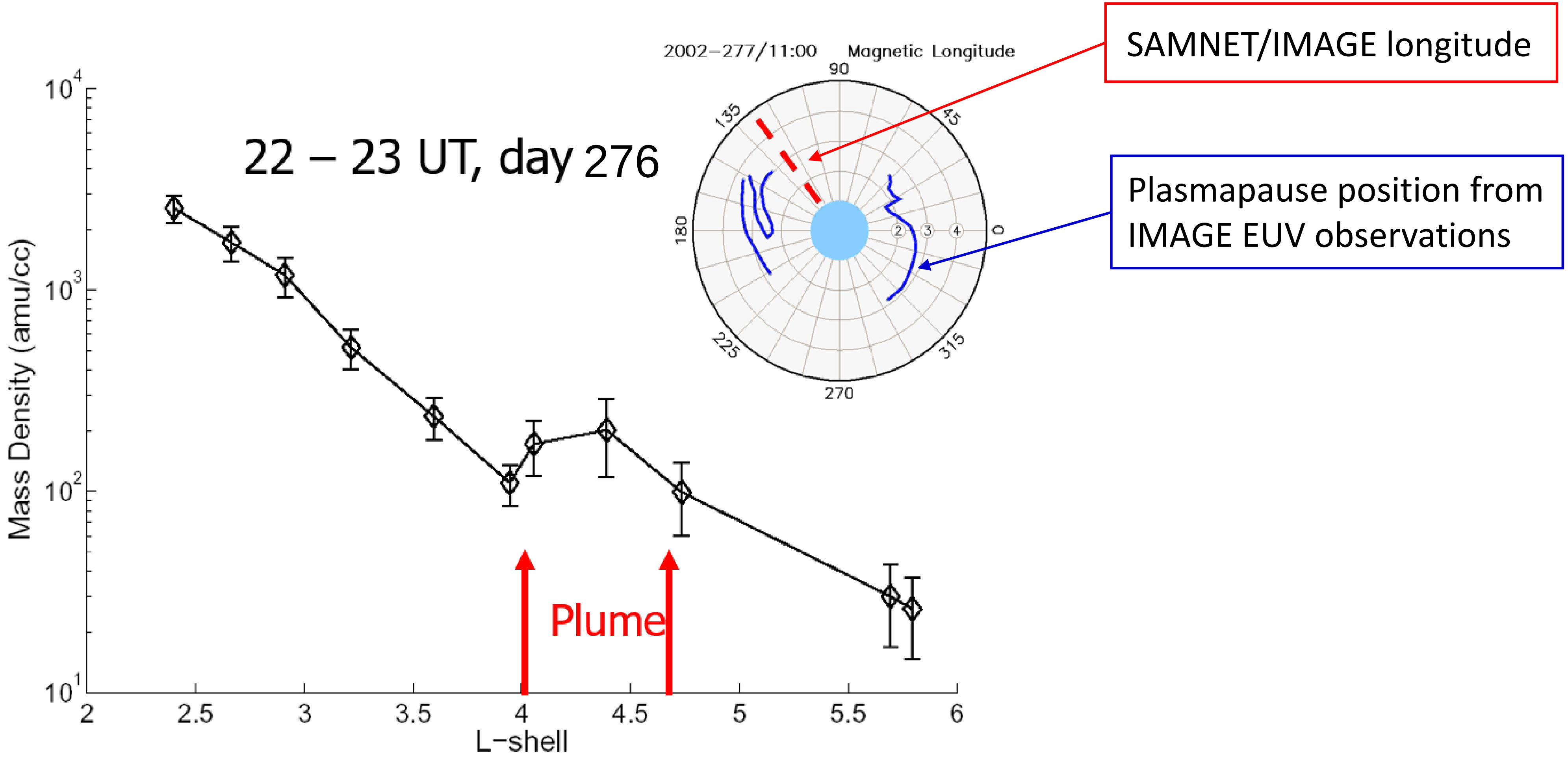

EMMA network

Del Corpo et al., 2015

Plasmasphere, erosion and refilling

SAMNET/IMAGE arrays

Obana et al., 2010

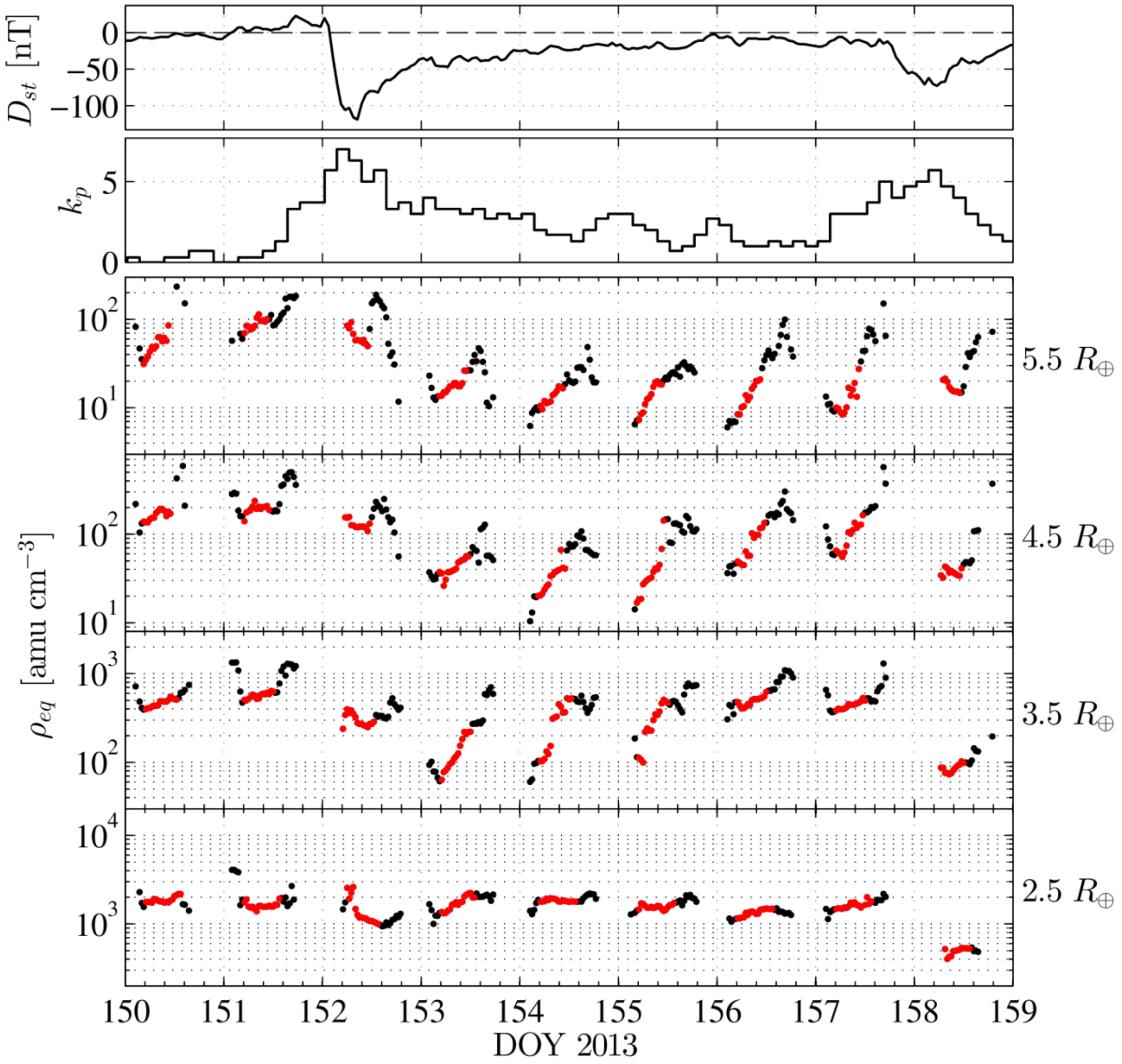

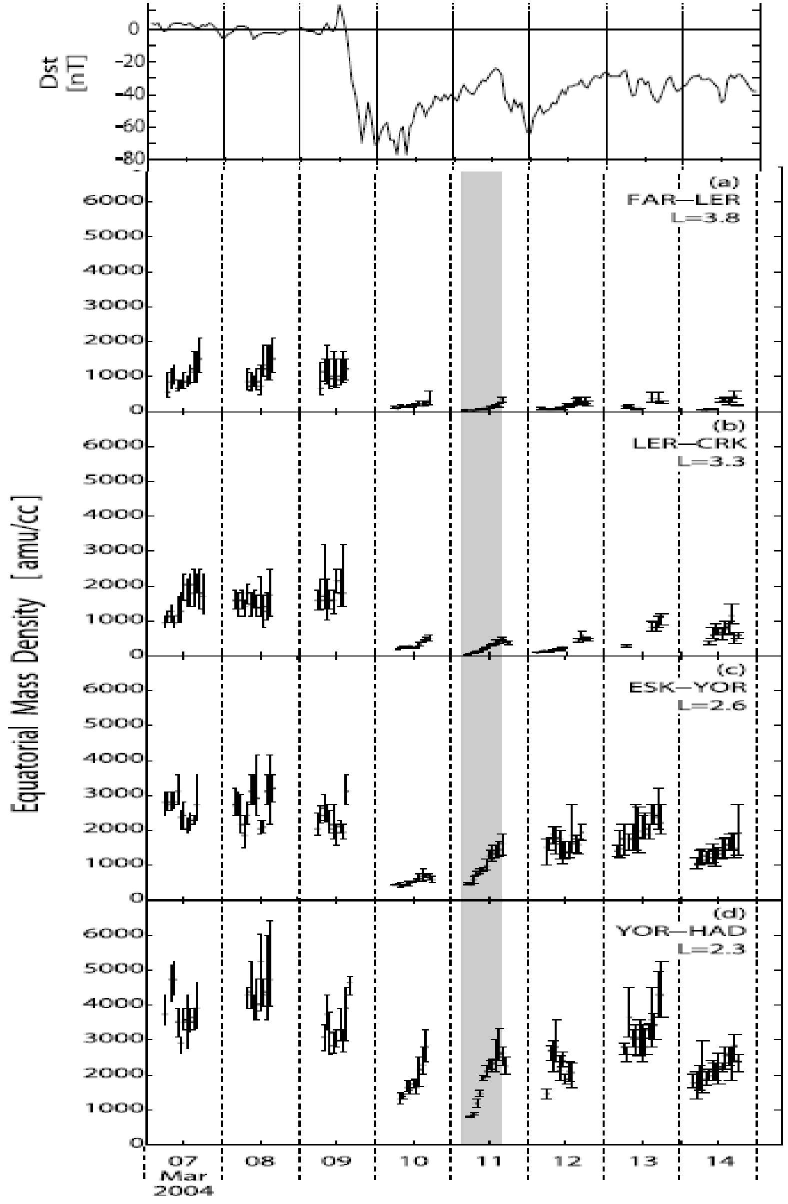

EMMA observations

Del Corpo et al., 2015

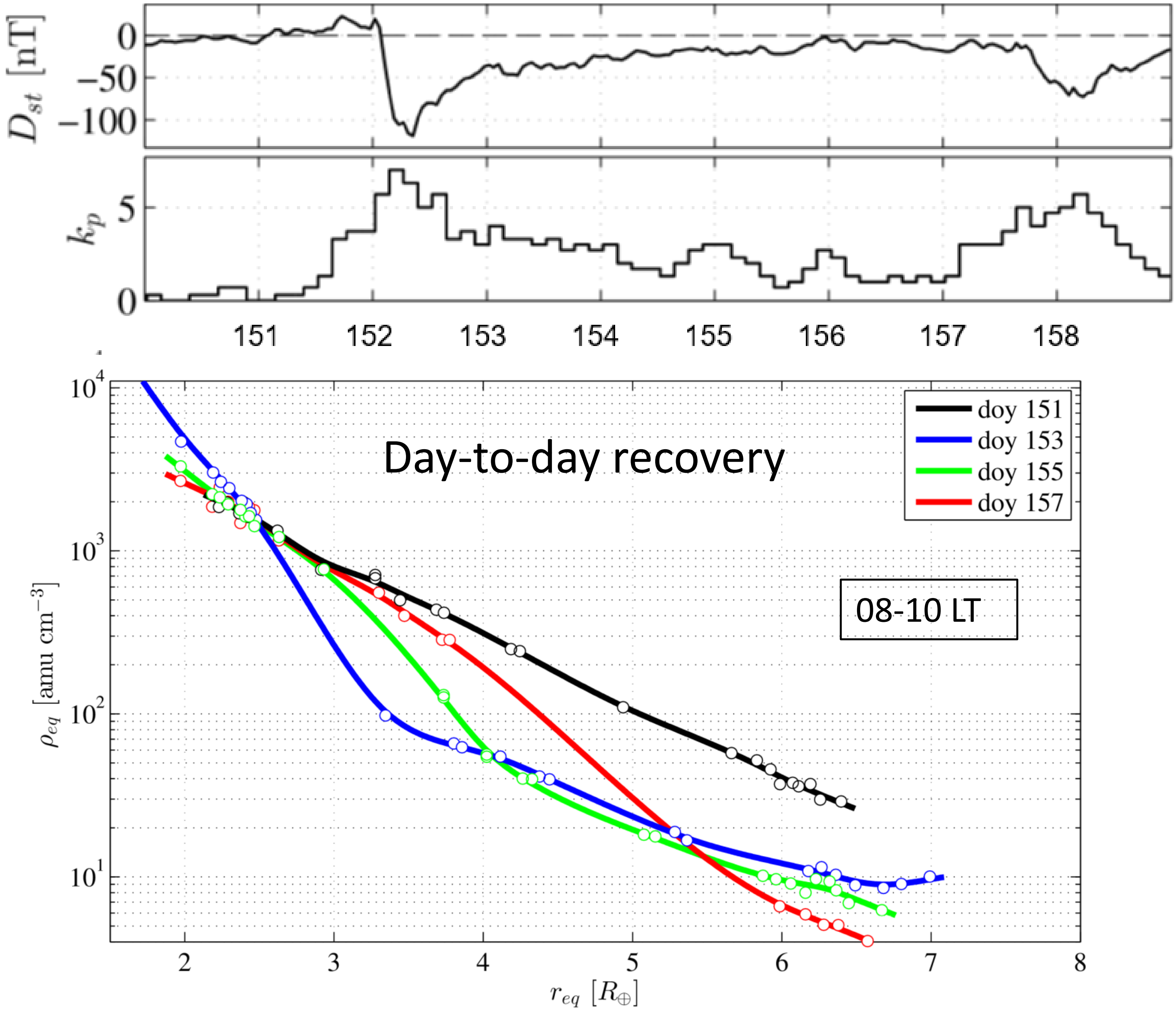

After 5 days from the Dst minimum, plasmasphere recovered to pre-storm conditions only for L < ~ 3.5.

Comparison of EMMA-FLR-derived plasma mass densities with in-situ (VAP) electron densities

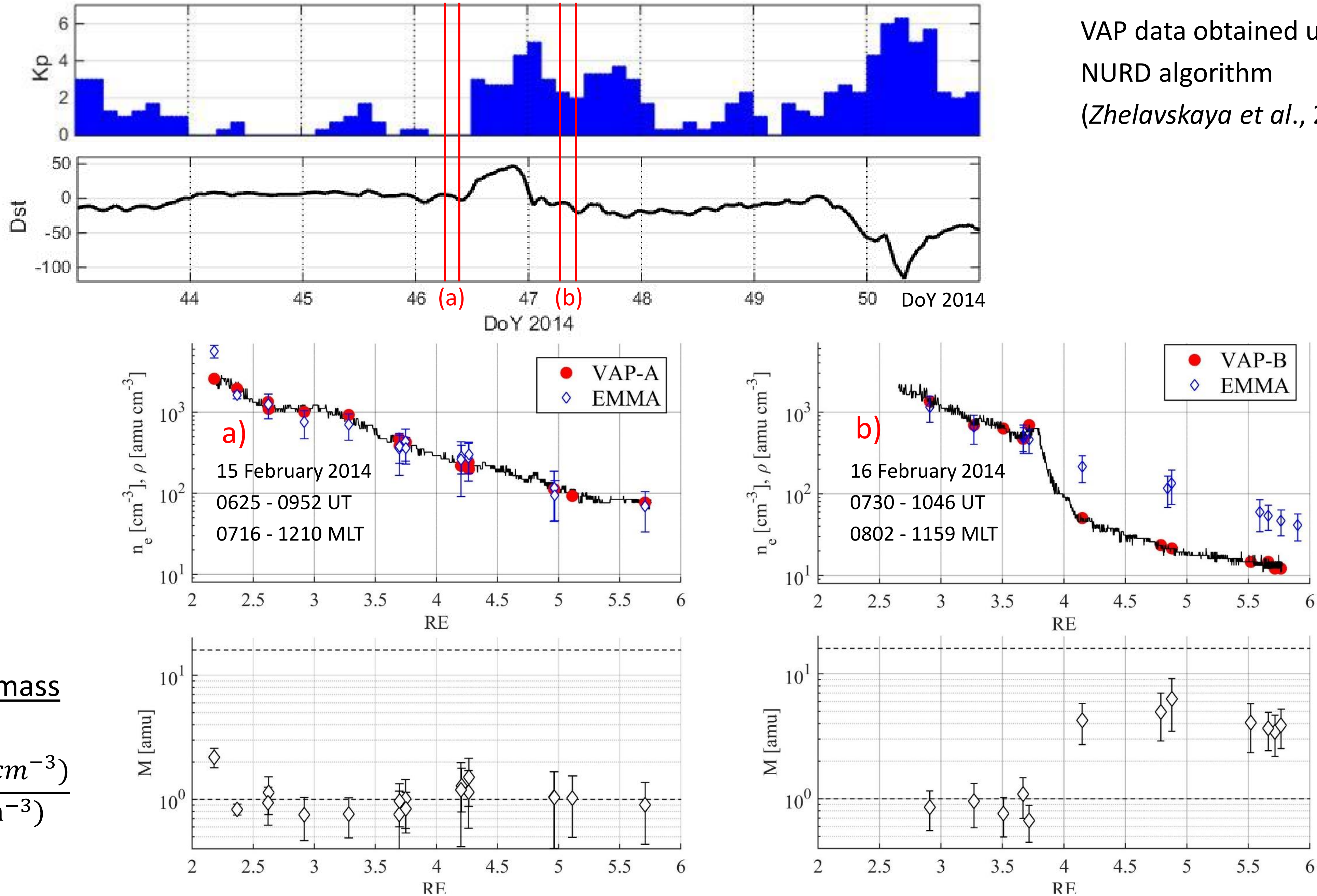

VAP data obtained using NURD algorithm (*Zhelavskaya et al.*, 2016).

<u>Average ion mass</u>

$$M = \frac{\rho\ (\text{amu}\ cm^{-3})}{n_e\ (\text{cm}^{-3})}$$

STATISTICAL ANALYSIS OF THE AVERAGE ION MASS FROM EMMA-VAP CONJUNCTIONS (2012/2017)

Del Corpo et al. (2022)

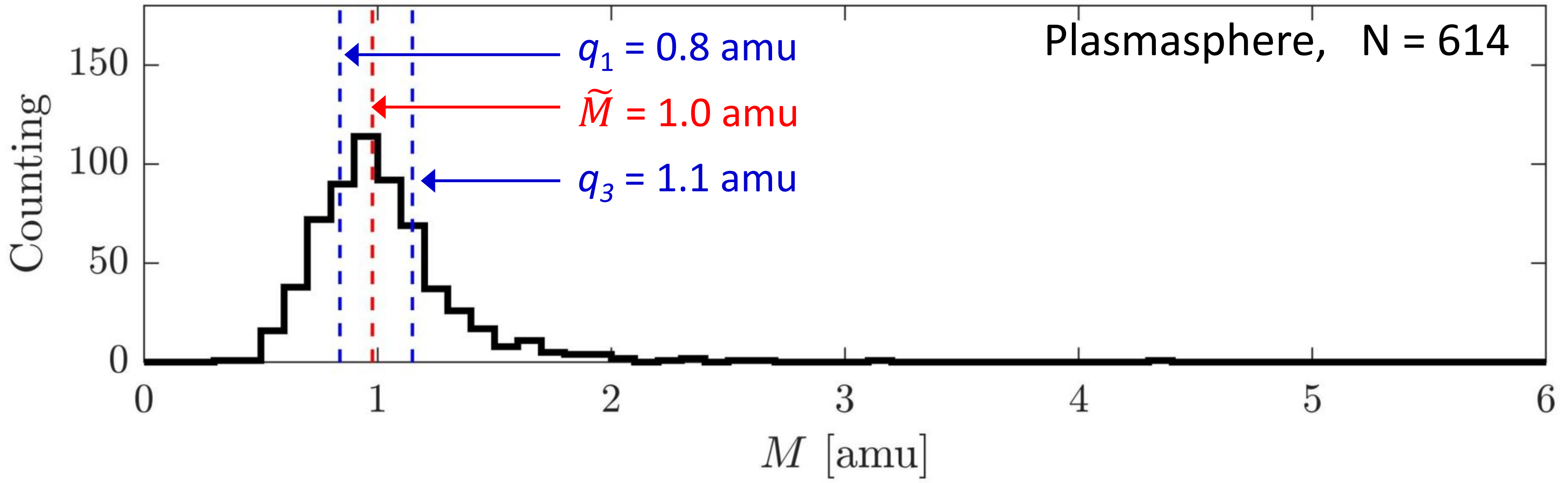

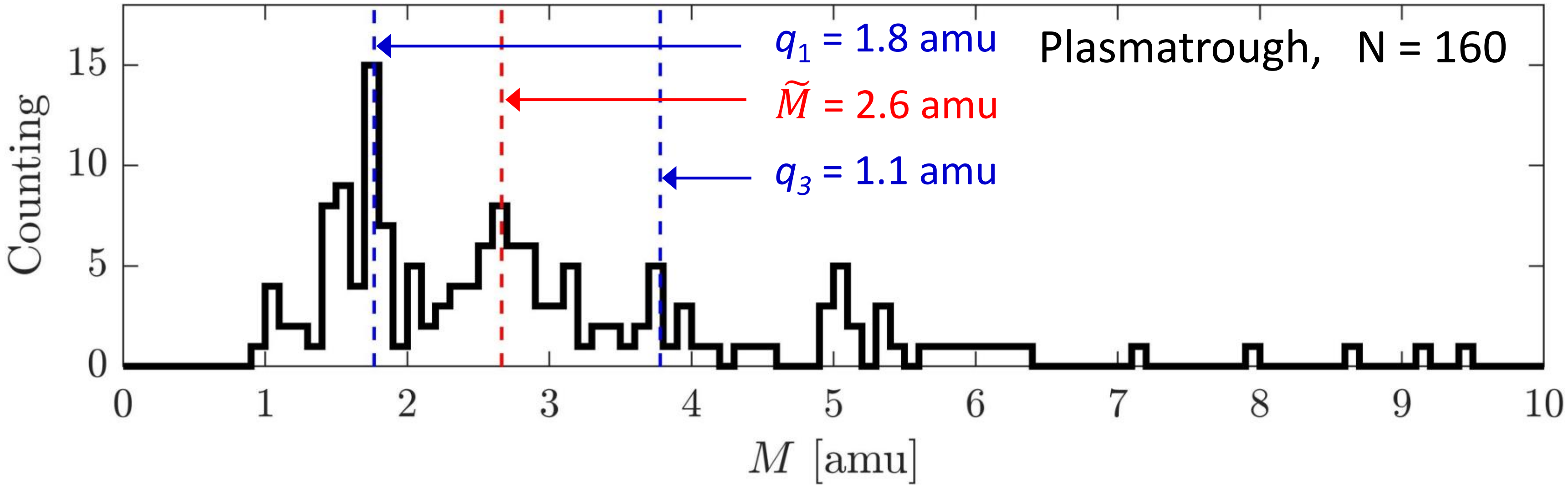

Radial, MLT, and Kp* dependences of the <u>Average Ion Mass</u> in PLASMASPHERE and PLASMATROUGH (*Del Corpo et al*. 2022)

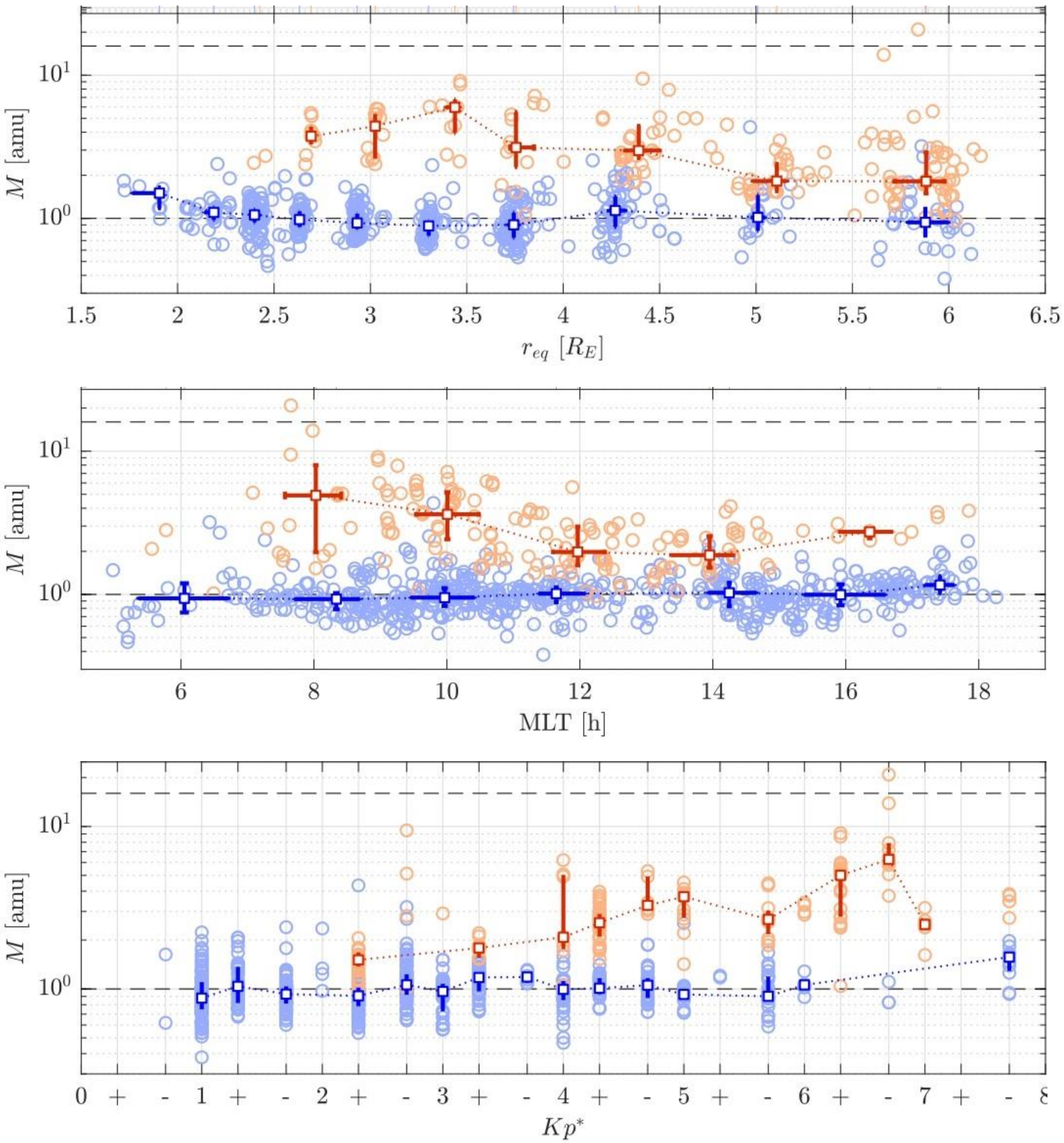

<u>RADIAL DEPENDENCE</u>

In plasmasphere, $M \cong 1$ amu at all distances.

Higher values at $L < 2$, possibly related to the He^+ and O^+ scale heights shorter than that of H^+.

In plasmatrough, maximum ~ 6 amu at r ~ 3.5 R_E.

<u>MLT DEPENDENCE</u>

No clear dependence in plasmasphere.

In plasmatrough: maximum in the 07-09 MLT sector.

<u>GEOMAGNETIC ACTIVITY DEPENDENCE</u>

No clear dependence in plasmasphere.

In plasmatrough: increasing with increasing level of disturbance.

PLASMASPHERE MONITORING USING TWO LONGITUDINALLY SEPARATED ARRAYS AND SPACE MEASUREMENTS (*Vellante et al.*, 2021)

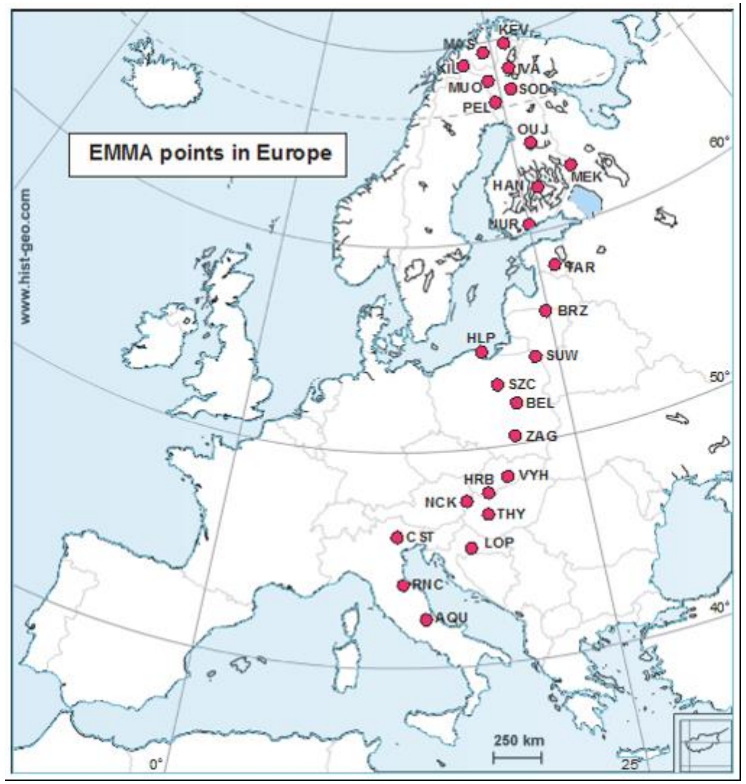

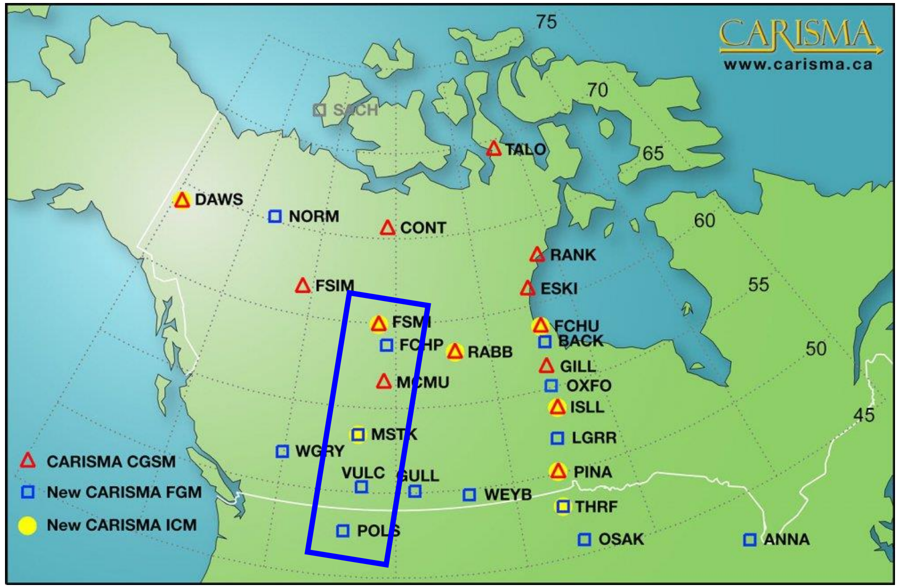

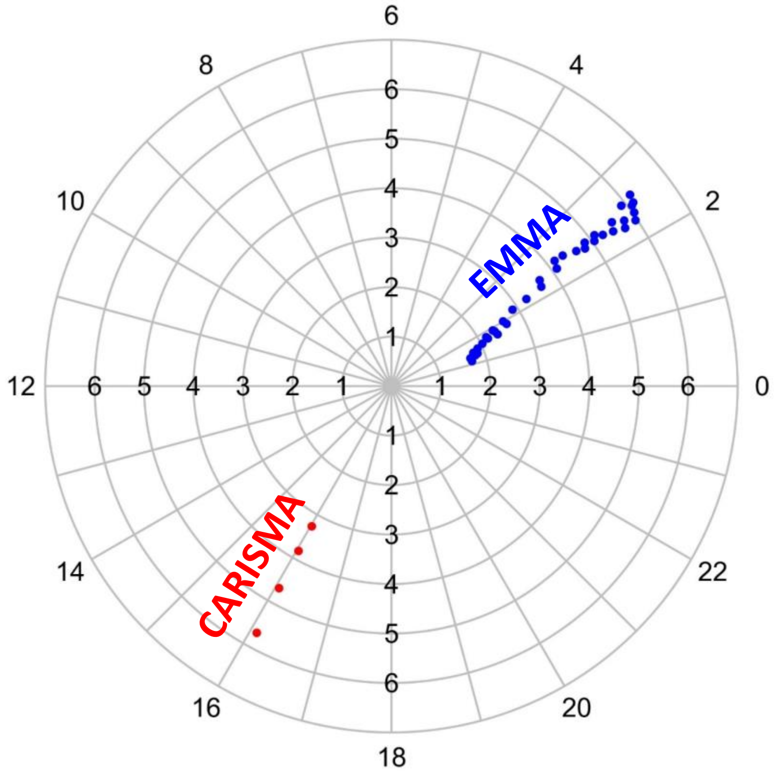

EQUATORIAL MAPPING OF THE MIDPOINT STATION PAIRS

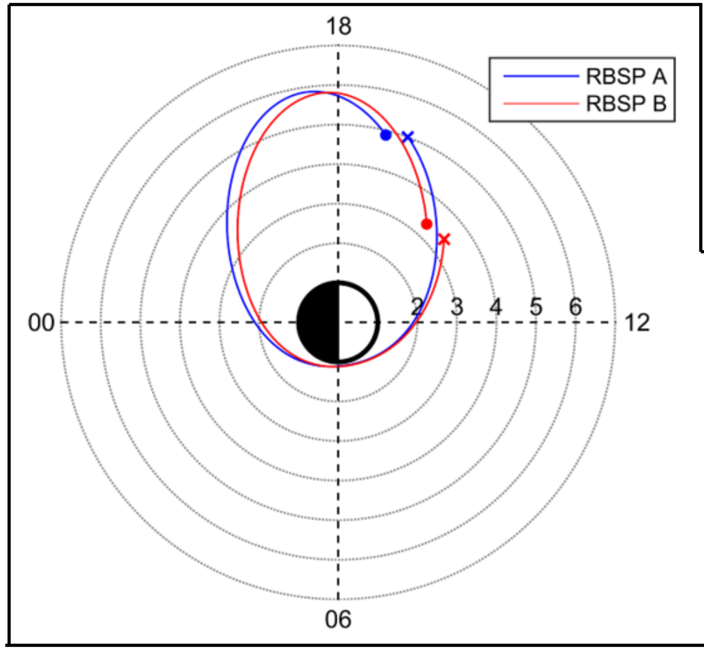

Van Allen Probes orbits (24 June 2015, 02-11 UT)

The afternoon outbound section is usable for comparison with the daytime ground observations

Time variation of plasma density at r_{eq} = 4 R_E, MLT = 16

(*Vellante et al.*, 2021)

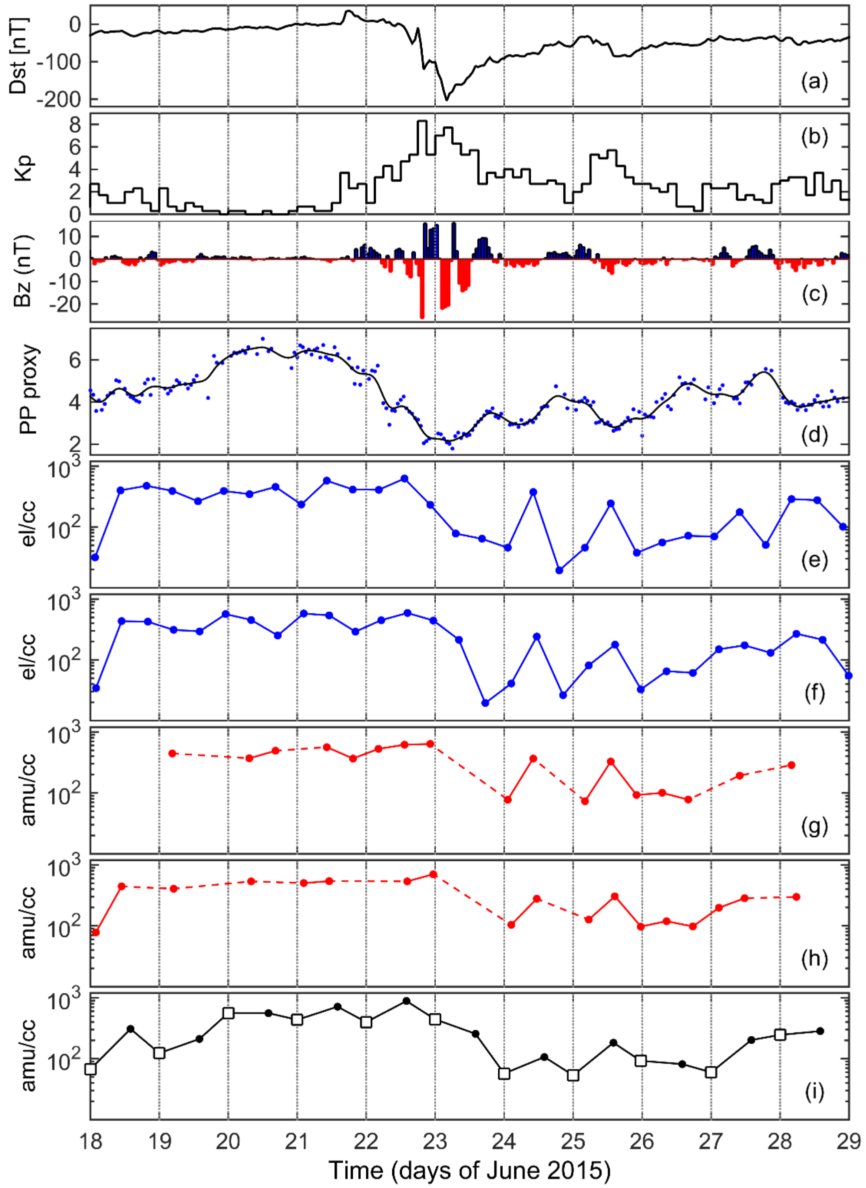

Dst

Kp

Bz

Midnight plasmapause location
(proxy from Swarm observations)

Ne RBSP A, MLT = 16.0 ± 0.3

Ne RBSP B, MLT = 15.7 ± 0.3

ρ RBSP A, MLT = 15.9 ± 0.3

ρ RBSP B, MLT = 15.6 ± 0.3

• ρ EMMA, MLT = 15.9 ± 0.1

□ ρ CARISMA, MLT = 16.0 ± 0.2

Plasmapause Test Particle simulation

Goldstein et al., 2014

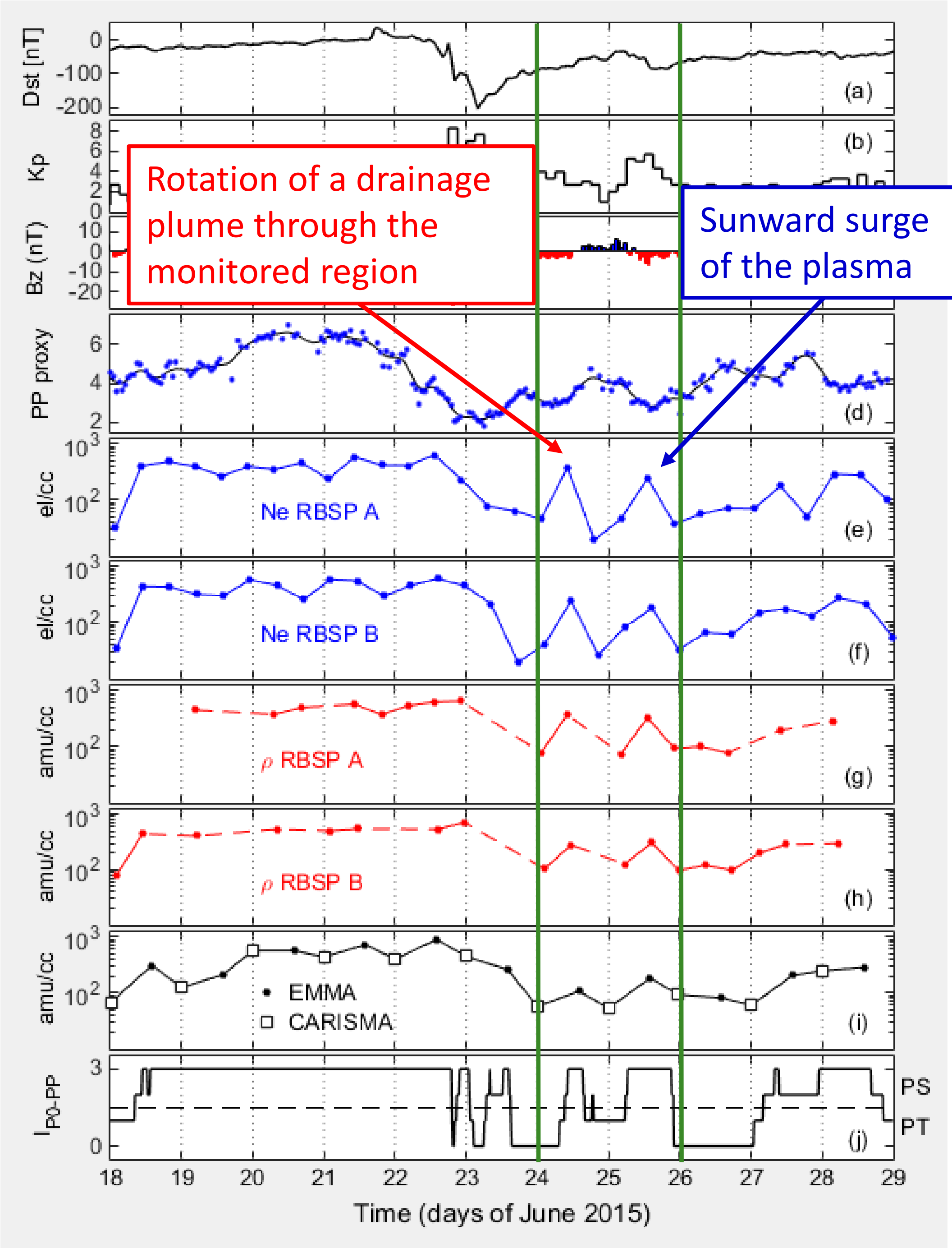

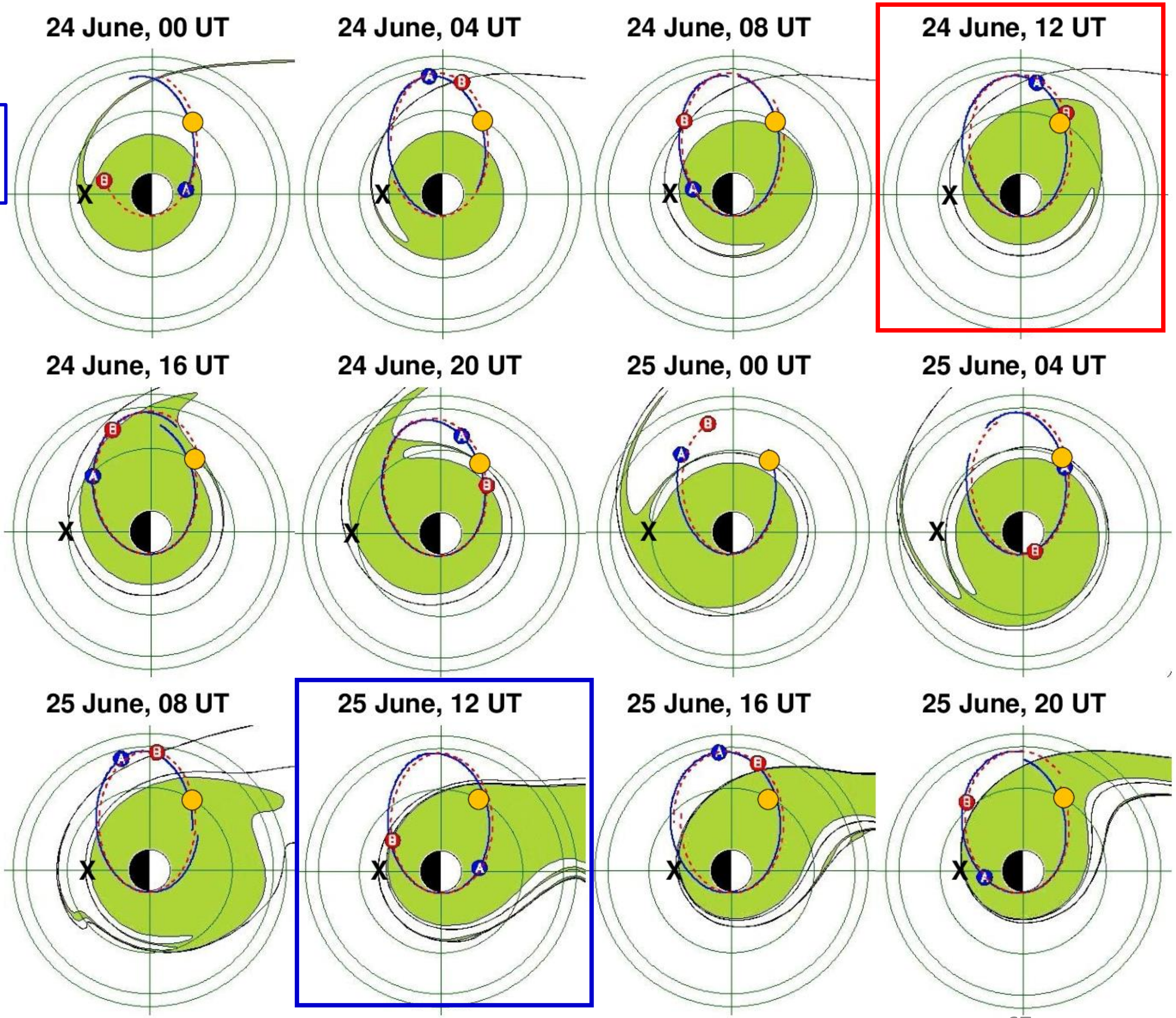

QUARTER-WAVE

Strong asymmetry of the ionospheric Pedersen conductance at the two ends of the field line

An example at L = 2.6 (*Obana et al.*, 2008)

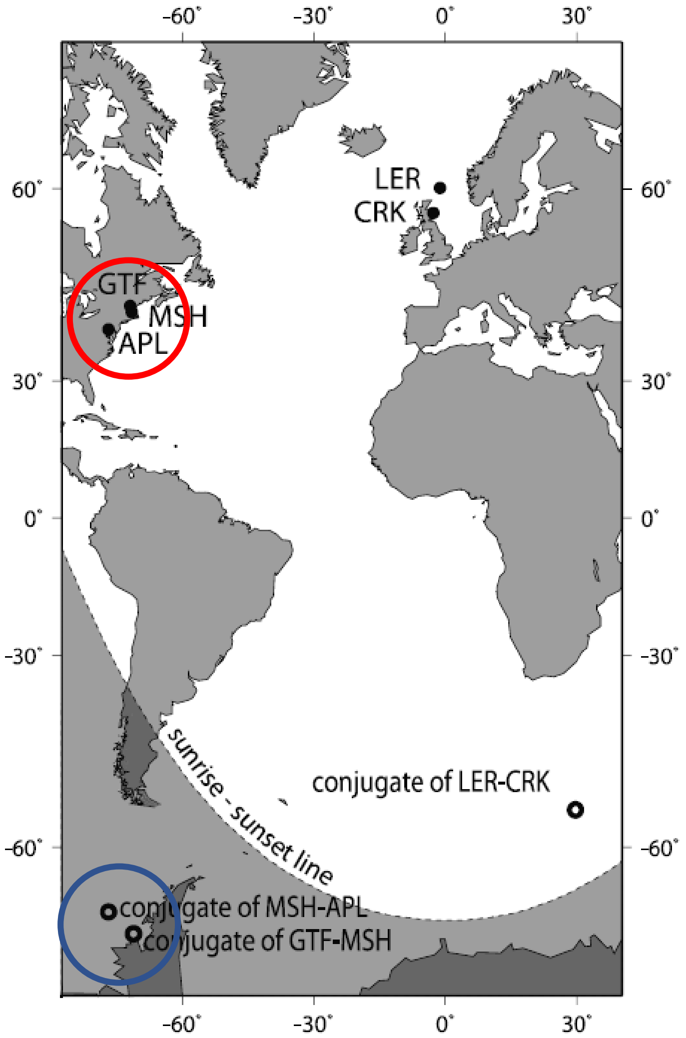

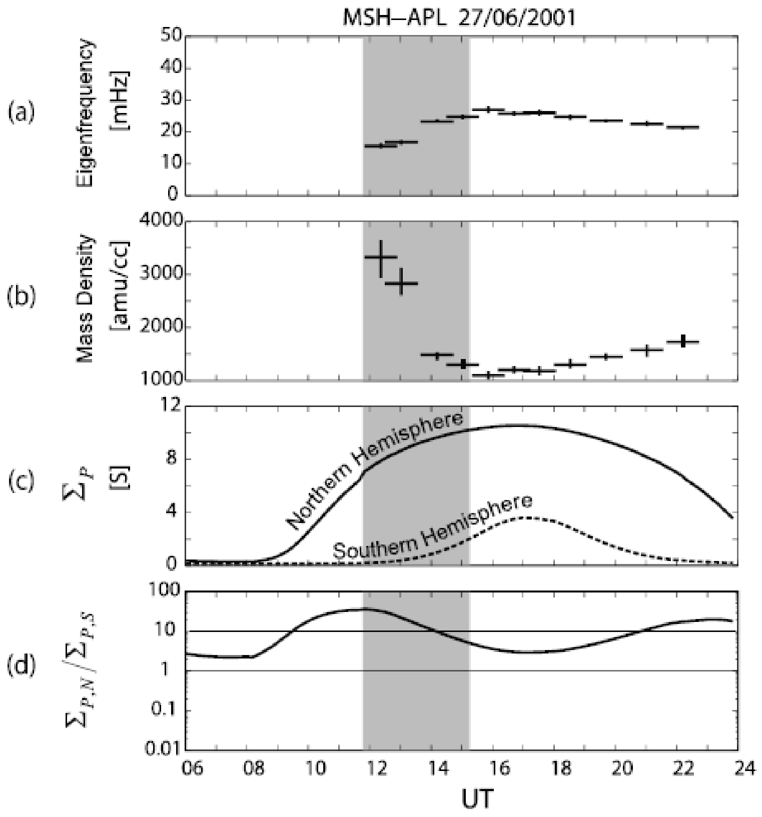

Figure 4. Time series of (a) eigenfrequency and (b) inferred mass density, from data shown in Figure 3. (c) Height-integrated Pedersen conductivities at northern (solid line) and southern (dashed line) ends of the field line. (d) Interhemispheric (north to south) ratio of Pedersen conductance.

Table 4. Inferred Mass Density Calculated Three Different Ways

Time (UT)	Frequency (mHz)	V_F 2006 Half-Wave	Solution of Wave Equation Half-Wave	Solution of Wave Equation Quarter-Wave
1230	15.5	3324	3325	1275
1300	16.8	2829	2831	1085
1600	27.0	1095	1103	420

If not correctly interpreted, inferred mass density significantly overestimated

Proper boundary condition to be used above the low-conductivity ionosphere:

$\mathbf{b} = \mu_o \Sigma_p \mathbf{e}$ (*Hughes & Southwood*, 1976)

Use of realistic ionospheric boundary conditions during night-time

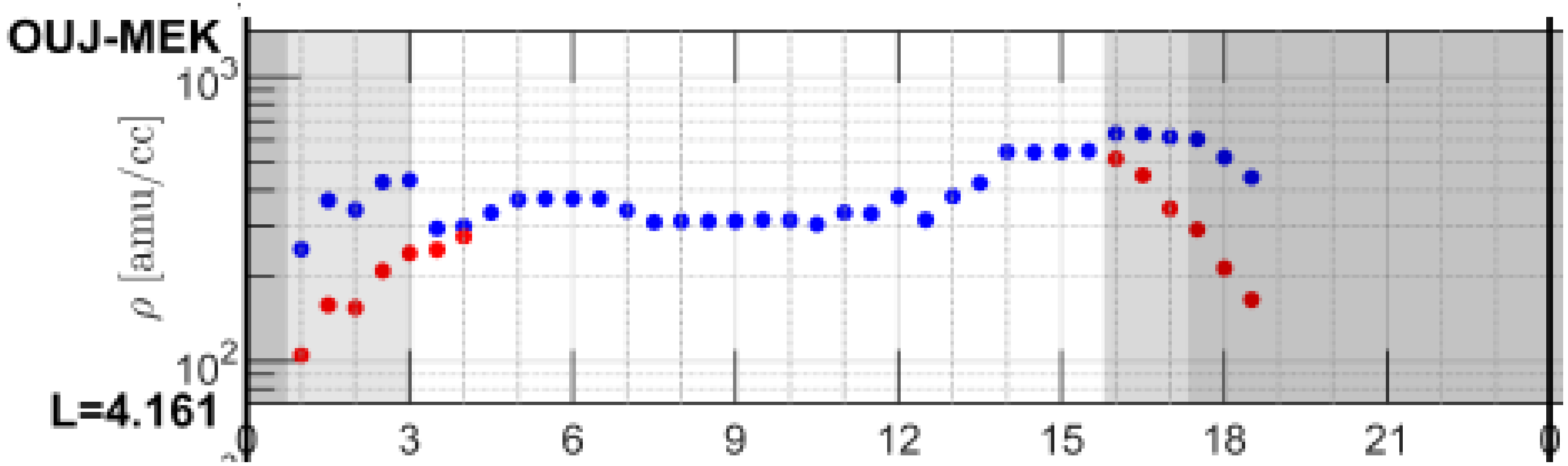

13 March 20015

Inferred equatorial mass density values assuming a fixed-end field line (blue dots) and finite ionospheric Pedersen conductance (red dots) from IRI model.

D. Sciarra (2022). MS thesis

Conclusions

Ground-based observations of FLRs is a powerful tool for remote sensing the plasma mass density in the inner magnetosphere.

Comparison with simultaneous measurements of the electron density allows to give important constraints on the relative abundances of heavy ions.

Meridional arrays can give important information, at least on a statistical basis, on spatial and temporal variations of the plasma density.

However, a single meridional array does not allow to get a global picture of the plasmaspheric dynamics occurring for example during geomagnetic storms. A larger, latitudinally extended, network is then necessary. This is also important to cover times when the array is in the night-time sector and FLRs are hardly detected.

Correct detection of FLRs can be quite time-consuming. Therefore the development of robust automated identification (including the use of machine learning methods, e.g. *Foldes et al.*, 2021) is very important. It would enormously increase the statistics, allowing to construct more sophisticated models of the spatial distribution of the plasma density. This is also important for using the technique in real-time monitoring.

At low latitudes ($L < 2$), because of the increased contribution of the near-ionosphere plasma, assuming the simple power law for the density distribution along the field line may lead to large errors in the inferred equatorial density. There is then need to search for more sophisticated dependences. A possible improvement might come from combining ULF wave observations with simultaneous ground-based ionospheric measurements which might provide important constraints.

Future experiments on board of satellites able to measure also the lowest energy ions ($< \sim 1$eV) would be very useful for a direct comparison of the FLR-derived mass density with the local one. This would represent a fundamental test for a complete validation of the FLR-technique.

References (cited in this lecture)

Baransky, L., et al. (1985). High resolution method of direct measurement of the magnetic field lines’ eigenfrequencies. *Planet. Space Sci*., 33 (12), 1369-1374. doi: 10.1016/0032-0633(85)90112-6

Berube, D., et al. (2003). An automated method for the detection of field line resonance frequencies using ground magnetometer techniques. *J. Geophys. Res.*, 108, 1348, doi: 10.1029/2002JA009737

Berube, D., et al. (2005). A plasmaspheric mass density model and constraints on its heavy ion concentration. *J. Geophys. Res.*, 110, A04212, doi: 10.1029/2004JA010684

Berube, D., et al. (2006). Computing magnetospheric mass density from field line resonances in a realistic magnetic field geometry. *J. Geophys. Res*, *111*, A08206, doi: 10.1029/2005JA011450

Carpenter, D.L., and R.R. Anderson (1992). An ISEE/whistler model of equatorial electron density in the magnetosphere. *J. Geophys. Res.*, *97*(A2), 1097–1108, doi: 10.1029/91JA01548

Chen, L., and A. Hasegawa (1974). A theory of long-period magnetic pulsations: 1. Steady state excitation of field line resonance. *J. Geophys. Res.*, 79, 1024-1032, doi: 10.1029/JA079i007p01024

Chi, P.J., et al. (2013). Sounding of the plasmasphere by Mid-continent MAgnetoseismic Chain (McMAC) magnetometers. *J. Geophys. Res.*, 118, 3077–3086, doi: 10.1002/jgra.50274

Clilverd, M.A., et al. (1991). The annual variation in quiet time plasmaspheric electron density determined from whistler mode group delays, *Planet. Space Sci*., 39, 1059–1067, doi: 10.1016/0032-0633(91)90113

Cummings, W.D., et al. (1969). Standing Alfvén Waves in the Magnetosphere. *J. Geophys. Res., 74, 778–793. doi:10.1029/JA074i003p00778*

Cz. Miletits, J., et al. (1988). East european pulsation array, autumn 1984. In *IX Winterschool on Magnetospheric Disturbances (KAPG), Sofia),* 128.

Del Corpo, A., et al. (2015). Temporal-spatial variations of cold plasma mass density in the inner magnetosphere from field line resonances detected at EMMA magnetometer network. *Paper presented at the 26th IUGG General Assembly, Prague*.

Del Corpo, A., et al. (2019). Observing the cold plasma in the Earth's magnetosphere with the EMMA network. *Annals of Geophysics*, *62*(4), GM447, doi: 10.4401/ag-7751

Del Corpo, A., et al. (2020). An empirical model for the dayside magnetospheric plasma mass density derived from EMMA magnetometer network observations. *J. Geophys. Res.*, *125*, doi: 10.1029/2019JA027381

Del Corpo, A., et al. (2022). Study of the Average Ion Mass of the Dayside Magnetospheric Plasma. *J. Geophys. Res.*, 127, e2022JA030605, doi: 10.1029/2022JA030605

Dungey, J.W. (1954). Electrodynamics of the outer atmosphere. *Penn. State Univ. Ionos. Res. Sci. Rept.*, 69

Foldes, R., et al. (2021). Assessing machine learning techniques for identifying field line resonance frequencies from cross-phase spectra. *J. Geophys. Res.*, 126, e2020JA029008, doi: 10.1029/2020JA029008

Fraser, B., et al. (2005). Heavy ion mass loading of the geomagnetic field near the plasmapause and ULF wave implications. *Geophys. Res. Lett.*, 32, L04102, doi: 10.1029/2004GL021315

Goldstein, J., et al. (2014). Simulation of Van Allen Probes plasmapause encounters. *J. Geophys. Res., 119*, 7464–7484, doi: 10.1002/2014JA020252

Green, C.A. (1978). Meridional characteristics of a Pc 4 micropulsation event in the plasmasphere. *Planet. Space Sci.*, 26, 955-967, doi: 10.1016/0032-0633(78)90078-8

Grew, R.S., et al. (2007). Mass and electron densities in the inner magnetosphere during a prolonged disturbed interval. *Geophys. Res. Lett., 34*, L02108, doi: 10.1029/2006GL028254

Gul'elmi, A.V. (1966). Plasma concentration at great heights according to data on toroidal fluctuations of the magnetosphere. *Geomagn. Aeron.*, 6, 98.

Heilig, B., et al. (2014). Ground based detection of the plasmapause and the density of the plasmasphere. *Paper presented at the EGU General Assembly, Vienna.*

Hughes, W.J. (1983). Hydromagnetic Waves in the Magnetosphere. In: *Carovillano, R.L., Forbes, J.M. (eds) Solar-Terrestrial Physics. Astrophysics and Space Science Library, vol 104. Springer, Dordrecht*, doi:10.1007/978-94-009-7194-3_18

Hughes, W.J. (1994). Magnetospheric ULF Waves: A Tutorial with a Historical Perspective. In *Solar Wind Sources of Magnetospheric Ultra-Low-Frequency Waves*, doi: 10.1029/GM081p0001

Hughes, W.J., and D.J. Southwood (1976). An illustration of modification of geomagnetic pulsation structure by the ionosphere. *J. Geophys. Res., 81*(19), 3241-3247, doi: 10.1029/JA081i019p03241

Jakowski, N., et al. (1991). Solar activity control of ionospheric and thermospheric processes, *J. Atmos. Terr. Phys.*, 53, 1125–1130, doi: 10.1016/0021-9169(91)90061-B

Jakowski, N., and M. Förster (1995). About the nature of the nighttime winter anomaly effect (NWA) in the F-region of the ionosphere. *Planet. Space Sci.*, 43, 603–612, doi: 10.1016/0032-0633(94)00115-8

Kale, Z.C., et al. (2007). Ground magnetometer observation of a cross-phase reversal at a steep plasmapause, *J. Geophys. Res*., 112, A10222, doi: 10.1029/2007JA012367

Lichtenberger, J., et al. (2013). The plasmasphere during a space weather event: First results from the PLASMON project. *J. Space Weather Space Clim*., *3*, A23, doi: 10.1051/swsc/2013045

McPherron, R.L. (2005). Magnetic Pulsations: Their Sources and Relation to Solar Wind and Geomagnetic Activity. *Surv Geophys*, 26, 545–592, doi: 10.1007/s10712-005-1758-7

Menk, F.W., et al. (2004). Monitoring the plasmapause using geomagnetic field line resonances. *J. Geophys. Res.*, 109, A04216, doi: 10.1029/2003JA010097

Menk, F.W., et al. (2012). The annual and longitudinal variations in plasmaspheric ion density. *J. Geophys. Res*., 117, A03215, doi:10.1029/2011JA017071

Milling, D.K., et al. (2001). Diagnosing the plasmapause with a network of closely spaced ground-based magnetometers. *Geophys. Res. Lett*., 28, 115–118, doi: 10.1029/2000GL011935

Obana, Y., et al. (2008). Quarter-wave Modes of Standing Alfvén Waves Detected by Cross-phase Analysis. *J. Geophys. Res*. 113, doi: 10.1029/2007ja012917

Obana, Y., et al. (2010). Plasma refilling rates for *L* = 2.3–3.8 flux tubes. *J. Geophys. Res.*, *115*, A03204, doi: 10.1029/2009JA014191

Ozhogin, P., et al. (2012). Field-aligned distribution of the plasmaspheric electron density: An empirical model derived from the IMAGE RPI measurements. *J. Geophys. Res.*, 117, A06225, doi: 10.1029/2011JA017330

Poulter, E.M., et al. (1988). ULF pulsation eigenperiods within the plasmasphere. *Planet. Space Sci*., 36 (2), 185-196. doi: 10.1016/0032-0633(88)90054-2

Samson, J.C., et al. (1971). Latitude-dependent characteristics of long-period geomagnetic micropulsations, *J. Geophys. Res.*, 76(16), 3675– 3683, doi: 10.1029/JA076i016p03675

Sandhu, J.K., et al. (2017). The dependence of magnetospheric plasma mass loading on geomagnetic activity using Cluster. *J. Geophys. Res.*, *122*, 9371–9395, doi: 10.1002/2017JA024171

Sciarra, D. (2022). Risonanze notturne delle linee del campo geomagnetico. *Tesi di laurea Magistrale, Università dell'Aquila, Italy*.

Sheeley, B., et al. (2001). An empirical plasmasphere and trough density model: CRRES observations. *J. Geophys. Res.*, 106(A11), 25,631–25,641. doi: 10.1029/2000JA000286

Singer, H.J., et al. (1981). Alfven Wave Resonances in a Realistic Magnetospheric Magnetic Field Geometry. *J. Geophys. Res.*, 86, 4589–4596, doi:10.1029/JA086iA06p04589

Southwood, D.J. (1974). Some features of field line resonances in the magnetosphere. *Planet. Space Sci.*, 22, 483-491, doi: 10.1016/0032-0633(74)90078-6

Tsyganenko, N.A., and M.I. Sitnov (2005). Modeling the dynamics of the inner magnetosphere during strong geomagnetic storms. *J. Geophys. Res.*, *110*, A03208, doi: 10.1029/2004JA010798

Vellante, M., et al. (1993). Simultaneous geomagnetic pulsation observations at two latitudes: resonant mode characteristics. *Ann. Geophys.*, 11(8), 734-741.

Vellante, M., et al. (1996). Solar cycle variation of the dominant frequencies of Pc3 geomagnetic pulsations at L=1.6. *Geophys. Res. Lett.*, 23, 1505-1508, doi: 10.1029/96GL01399

Vellante, M., and M. Förster (2006). Inference of the magnetospheric plasma mass density from field line resonances: A test using a plasmasphere model. *J. Geophys. Res.*, 111, A11204, doi:10.1029/2005JA011588

Vellante, M., et al. (2007). Solar activity dependence of geomagnetic field line resonance frequencies at low latitudes. *J. Geophys. Res.*, *112*, A02205, doi: 10.1029/2006JA011909

Vellante, M., et al. (2021). Multi-instrument characterization of magnetospheric cold plasma dynamics in the June 22, 2015 geomagnetic storm. *J. Geophys. Res.*, 126 (6), doi: 10.1029/2021JA029292

Waters, C.L., et al. (1991). The resonance structure of low latitude Pc3 geomagnetic pulsations. *Geophys. Res. Lett.*, 18 (12), 2293-2296, doi: 10.1029/91GL02550

Waters, C.L., et al. (1994). Low latitude geomagnetic field line resonance: Experiment and modeling, *J. Geophys. Res.*, *99*(A9), 17,547−17,558, doi: 10.1029/94JA00252

Yumoto, K. (1988). External and Internal Sources of Low-Frequency MHD Waves in the Magnetosphere-A Review. *J. Geomag. Geoelectr.*, 40, 293-311, doi: 10.5636/jgg.40.293

Zhelavskaya, I.S., et al. (2016). Automated determination of electron density from electric field measurements on the Van Allen Probes spacecraft. *J. Geophys. Res.*, 121, 4611–4625, doi: 10.1002/2015ja022132

Several arguments presented in this lecture can be found in:

Menk, F. W., & Waters, C. L. (2013). *Magnetoseismology: Ground-Based remote sensing of Earth's magnetosphere*. John Wiley & Sons, Inc., https://doi.org/10.1002/9783527652051

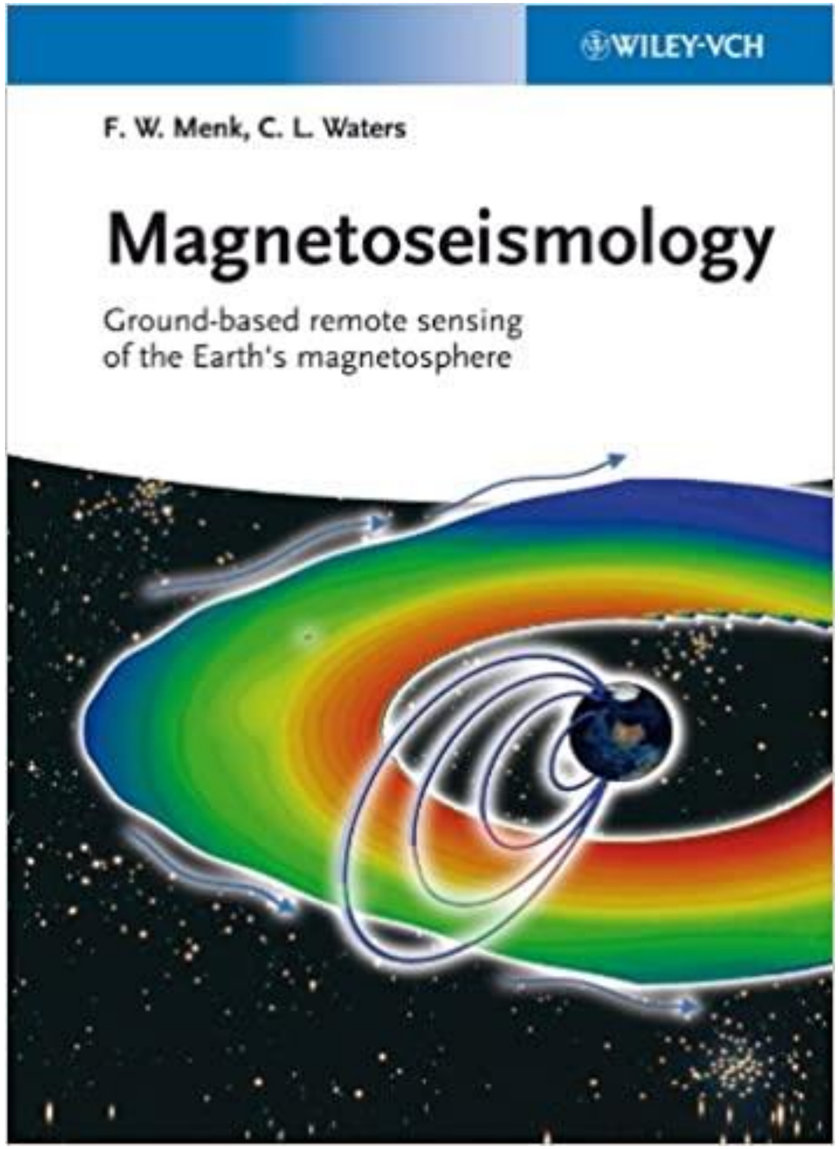

Thank you for your attention